A Reversible Metabolic Stress-Sensitive Regulation of Collapsin Response Mediator Protein 2A Orchestrates Cytoskeletal Remodeling and EMT, Increasing Metastatic Potential in Cancer

by

Aristeidis Boukouris

A thesis submitted in partial fulfillment of the requirements for the degree of

Doctor of Philosophy

Department of Medicine

University of Alberta

© Aristeidis Boukouris, 2021

Abstract

Cancer represents the second leading cause of death globally only after heart disease and is responsible for about 10 million deaths per year with a significant economic impact (WHO facts). Moreover, its prevalence is projected to increase over the following decades. Among all cancers, breast, lung and colorectal cancer represent the three most prevalent types of cancer. Intriguingly, it is estimated that 90% of all cancer morbidity and mortality is due to metastasis, i.e. the spread of cancer cells from the primary tissue of origin into surrounding structures and remote organs. Despite the several promising advances in cancer therapeutics, such as hormone therapy and immunotherapy, all available therapies are directed against the primary tumor, while no significant progress has been made regarding strategies to prevent metastasis. Therefore, a lot more work is needed in order to better understand the mechanisms and triggers of metastasis. The ability of cancer cells to metastasize is often preceded by a process called epithelial-to-mesenchymal transition (EMT), an extensive cellular rearrangement, which confers structural and molecular features to cells, enabling them to leave their original site and migrate to other tissues. It is thought that the signals to cancer cells for metastasis most often come from the surrounding stroma cells, mainly fibroblasts but also immune cells and vascular pericytes. Furthermore, the decision to metastasize, although beneficial for cancer cells in the long term, needs to be coupled with the metabolic state of cells and the fuel availability as EMT and metastasis are energy-intensive processes. Whether cancer cells also have “endogenous breaks” that need to be overcome for the process of metastasis to be fully activated and how these “breaks” relate to metabolic stress

remains unknown. Identifying such cell-autonomous mechanisms of metastasis has the potential to create new important perspectives on cancer therapeutics, by preventing metastasis-related deaths.

Here we show that Collapsin Response Mediator Protein 2A (CRMP2A), a microtubule-associated protein (MAP) with implications in neuron development and neurodegenerative diseases, is reversibly induced in lung cancer cells in response to metabolic stress and regulates the ability of cells to undergo EMT/metastasis. Loss of CRMP2A results in increased invasion and metastasis *in vitro* and *in vivo* but also acquisition of a cancer stem cells phenotype, characterized by chemoresistance, increased tumor-initiating capacity and metabolic rearrangement towards increased nucleotide synthesis from glutamine, now all recognized as features of partial EMT and aggressive/metastatic tumors. We found that the ability of CRMP2A to regulate these important cell fate decisions relies on the remodeling of the cytoskeleton, which in turn regulates several EMT-related processes, such as transcription factor trafficking and ciliogenesis.

This is one of the very few reports that a single MAP, like CRMP2A is able to orchestrate a complex cytoskeletal, metabolic and EMT/stemness program in cancer cells. Our discovery may have important implications for therapeutic strategies aiming at halting metastasis.

Preface

This thesis is an original work by Aristeidis Boukouris. Chapter 2 has been submitted for peer review and is under revision in Cell Reports.

To my beloved parents

Acknowledgements

First, I would like to express my deepest gratitude to my supervisor Dr. Evangelos Michelakis, whose mentorship and continuous guidance have inspired me in many ways and have shaped me into a better scientist and person. I must also acknowledge my committee members, Dr. Gopinath Sutendra and Dr. Gary Lopaschuk, for their leadership and valuable insight throughout my studies. Most importantly, I would like to thank my parents, Evangelos and Konstantina, for their love and constant support, without which completion of this dissertation would not have been possible. Finally, I would like to thank my colleagues Adam, Bruno, Yongneng, Mo, Vikram, Areli, Subhash, Alois, Yuan Yuan, Trevor and Yongsheng and especially my good friend Sotirios Zervopoulos for their friendship and hard work together, which made this journey a very pleasant one.

Table of Contents

List of Tables

List of Figures

List of Abbreviations

2D – 2-Dimensional

2-HG – 2-Hydroxyglutarate

AST – Aspartate Aminotransferase

ATP – Adenosine Trisphosphate

BMP2 – Bone Morphogenetic Protein 2

CDK5 – Cyclin-Dependent Kinase 5

ChIP – Chromatin Immunoprecipitation

c-Myc – V-Myc Avian Myelocytomatosis Viral Oncogene Homolog

CNS – Central Nervous System

CSC – Cancer Stem Cells

CRMP2A – Collapsin Response Mediator Protein 2A

CRMP2B – Collapsin Response Mediator Protein 2B

CRISPR – Clustered Regularly Interspaced Short Palindromic Repeats

ddPCR – droplet digital Polymerase Chain Reaction

DAPI – 4′,6-diamidino-2-phenylindole

DHPase – Dihydropyrimidinase

DMEM – Dulbecco's Modified Eagle Medium

DNA – Deoxyribonucleic acid

DPYSL2 – Dihydropyrimidinase-related Protein 2

DSS – Disuccinimidyl Suberate

EMT – Epithelial-to-Mesenchymal Transition

EtBr – Ethidium Bromide

ETC – Electron Transport Chain

FER – Feline Encephalitis Virus-Related Kinase

GAPDH – Glyceraldehyde-3-Phosphate Dehydrogenase

GDH – Glutamate Dehydrogenase

GLS1 – Glutaminase 1

GLS2 – Glutaminase 2

GO – Gene Ontology

GSK-3β – Glycogen Synthase Kinase 3β

HIF-1α – Hypoxia-Inducible Factor 1α

His – Histidine

IDH – Isocitrate Dehydrogenase

kDa – Kilodalton

mtDNA – mitochondrial DNA

MAP – Microtubule-Associated Protein

MAT2A – Methionine S-Adenosyltransferase 2A

MEF – Mouse Embryonic Fibroblast

MMP-2 – Matrix Metallopeptidase 2

mRNA – messenger RNA

MW – Molecular Weight

NF-κb – Nuclear Factor kappa-light-chain-enhancer of activated B cells

NFATc2 – Nuclear factor of activated T-cells, cytoplasmic 2

NSCLC – Non-Small Cell Lung Cancer

OCR – Oxygen Consumption Rate

PKC – Protein Kinase C

PDK1 – Pyruvate Dehydrogenase Kinase 1

PTEpiC – (Renal) Proximal Tubular Epithelial Cells

PTM – Post-Translational Modification

qRT-PCR – quantitative Real Time-Polymerase Chain Reaction

RNA – Ribonucleic Acid

rhTGF-β1 – recombinant human Transforming Growth Factor β1

SAEC – Small Airway Epithelial Cells

Scr – Scramble

siRNA – small interfering RNA (Ribonucleic Acid)

SIRT3 – Sirtuin-3

SMAD3/4 – (Small) Mothers Against Decapentaplegic homolog 3/4

Sox2 – Sex determining region Y-box 2

STAT3 – Signal Transducer and Activator of Transcription 3

SUMO – Small Ubiquitin-Related Modifier

TCA – Tricarboxylic Acid

TFAM – Transcription factor A, mitochondrial

TGF-β1 – Transforming Growth Factor β1

TF – Transcription Factor

Thr – Threonine

TSS – Transcription Start Site

TWIST1 – Twist-related Protein 1

Ser – Serine

UCK2 – Uridine-Cytidine Kinase 2

UMP – Uridine Monophosphate

vWF – von Willebrand Factor

ZEB1 – Zinc finger E-box-binding homeobox 1

α-KG – alpha-ketoglutarate

Chapter One: Background

1.1 Metabolic reprogramming and metabolic stress in cancer

One of the hallmarks of cancer cells that differentiates them from normal cells is their increased, uncontrolled proliferation[1]. Sustaining this trait requires cancer cells to produce increased amounts of building blocks: lipids (fatty acids), proteins (amino acids) and nucleic acids (nucleotides). In order to support the need for increased biomass production, cancer cells deploy a complex metabolic reprogramming, which is mainly characterized by increased glucose ("aerobic glycolysis"; Warburg effect[2]) and/or glutamine utilization. The Warburg effect describes the reliance of cancer cells on glycolysis for energy production bypassing the mitochondria even in the presence of ample oxygen. By contrast, normal cells process glucose first into pyruvate and then into carbon dioxide in the mitochondria under aerobic conditions (glucose oxidation) and only switch to lactate production in hypoxic conditions. Elevated glutaminolysis has also recently emerged as a metabolic feature of cancer cells[3]. In the absence of glucose oxidation, glutamine constitutes the major fuel of the TCA cycle contributing to ATP production, especially under hypoxia[4]. Aside from that, glutamine is used in cancer cells to boost lipid synthesis[5] and is also essential for the de novo nucleotide synthesis, both directly by donating nitrogen groups and indirectly through increased generation of aspartate in the TCA cycle[6].

Besides generation of macromolecules and uncontrolled growth, the metabolic rewiring in cancer cells has also been linked to the process of metastasis. For example, decreased glucose oxidation and increased lactate production contributes to generation of an acidic tumor microenvironment that favors metastatic dissemination, primarily by facilitating degradation of the extracellular matrix[7]. Similarly, several

studies have described the contribution of glutamine metabolism to cancer metastasis, although most effects appear to be mediated by glutaminase 1 (GLS1)[8]. Therefore, strategies to inhibit increased glycolysis and glutaminolysis have the potential to halt both tumor growth and tumor spread.

The metabolic rewiring of cancer cells has been largely attributed to activation of oncogenes, (e.g. RAS, HIF-1α, c-Myc and Snail), and tumor suppressor deactivation (e.g. p53), which results in upregulation of several metabolic enzymes and nutrient transporters[9]. Aside from that, malignantly transformed cells often harbor mutations in key metabolic enzymes, generating the so-called oncometabolites that act as agonists and/or antagonists for epigenetic modification enzymes (histone deacetylases, histone methyltransferases and DNA methyltransferases)[10]. Of these enzymes, the TCA cycle enzymes isocitrate dehydrogenases 1 and 2 (IDH1/2) deserve special mention. Mutated IDH1/2 produce large amounts of the oncometabolite 2-hydroxyglutarate (2-HG), which antagonizes the activity of α-ketoglutarate (α-KG), leading to aberrant DNA and histone methylation[11] as well as activation of epithelial-to-mesenchymal transition (EMT)[12,13].

Despite the upregulation and alteration of these metabolic pathways, cancer cells in tumors often experience conditions of metabolic stress due to limited fuel supply. This is especially true for the initial stages of tumor formation, where rapid cell proliferation frequently overrides the ability of the vascular network to provide enough fuel, such as glucose and oxygen. Relevant studies have been conducted in solid tumors, showing that cancer cells lying more than 100-150μm away from the capillaries experience significantly lower levels of oxygen (and glucose) compared to cells in the proximity of vessels[14-16].

Proper adaptation to metabolic stress is critical for the survival of cancer cells and it has to be coordinated with other critical cell fate decisions like proliferation, migration and epithelial-to-mesenchymal transition (EMT), which are energy-demanding processes[17]. HIF activation[18] and enhanced autophagy with recycling of intracellular organelles[1] are two of the mechanisms that have been implicated in the response to metabolic stress. However, the overall understanding of how cancer cells adapt to fluctuating fuel levels and how other processes are regulated is still poor.

1.2 The Collapsin Response Mediator Protein 2

Collapsin Response Mediator Protein 2 (CRMP2, also known as DPYSL2; Dihydropyrimidinase-related protein 2) and its two major isoforms A and B belong to the family of Collapsin Response Mediator Proteins (CRMPs), which consists of five different groups of proteins (CRMP1-5). All family members share a considerable (50-75%) sequence similarity with each other as well as to the enzyme Dihydropyrimidinase (DHPase) (60%)[19], which is why overlapping functions have been proposed for some of them. However, unlike DHPase, which converts dihydrouracil into 3-ureidopropanoate (pyrimidine metabolism), no enzymatic activity has ever been reported for the CRMP2 family of proteins, possibly due to a lack of critical histidine residues (His69, His248) at the amidohydrolase catalytic site[20].

CRMP2B is the shorter isoform of CRMP2 (MW: 64kDa) and the most well studied of the two, possibly due to its much higher expression/abundance compared to CRMP2B. The crystal structure of CRMP2B along with some of its structural

domains have been identified[21,22] (**Fig. 1-1A**). Cross-linking experiments have shown that CRMP2B can be present in monomers, dimers and (homo)tetramers, while an association with CRMP1 (heterotetramers) has also been proposed. The longer isoform CRMP2A (MW: 73kDa) shares an 85% sequence similarity with CRMP2B at the mRNA and protein level except for Exon 1 of the CRMP2A mRNA, which encodes an N-terminal stretch of 118 amino acids unique to the CRMP2A protein (**Fig. 1-1B**). Unlike CRMP2B, CRMP2A remains yet to be crystallized, therefore little is known about how its domains compare to those of CRMP2B. The extra N-terminal piece does not seem to bear significant similarity to proteins outside the CRMP family. However, our own in silico analysis using the protein structure prediction software iTASSER revealed the presence of helix and strand components within this piece (**Fig. 1-1C**). Despite the lack of available data regarding its structure, CRMP2A has been proposed to be able to form hetero-multimeric complexes together with CRMP1A and CRMP-Bs[23]. Regarding the mechanism behind production of the two different isoforms, although alternative splicing has also been proposed[24], other reports suggest the presence of different promoters as the most likely mechanism for the generation of CRMP2A and CRMP2B[25]; the last theory is also supported by our *in silico* analysis based on publicly available databases (Ensembl, UCSC).

The highest expression of the CRMP2 isoforms has been described in neurons, where they have also most extensively been studied[20,24,26]. They are most highly expressed during the neurogenic (intense axon outgrowth) period of brain development[26]. In mature neurons, CRMP2B is distributed along axons and dendrites, whereas CRMP2A is the dominant isoform in distal axons (in the vicinity

of growth cones)[23,27]. Both proteins were initially described as intracellular mediators of Collapsin (also known as Semaphorin-3A), a protein that induces collapse of growing nerve cones[28] during development of the nervous system and CNS injury[29]. It was later shown that CRMP2B promotes axon growth and branching by promoting microtubule formation. Specifically, CRMP2B is able to bind on free cytoplasmic tubulin (heterodimers) and promote tubulin polymerization and microtubule assembly, which is critical for axon elongation[30]. This microtubule-directed activity is the most important function described to date for CRMP2B and depends heavily on its phosphorylation status (C-terminus of the protein), which is regulated by several different kinases (Ser522 by CDK5, the priming phosphorylation event[31]; Thr514 by GSK-3β[31], PKC-βII[32] and PKC-γ[33]; Thr555 by ROCK II[34] and CaMKII[35] kinases). Phosphorylation of CRMP2B results in decreased association of CRMP2B with tubulin, which in turn reduces microtubule formation and axon growth (growth cone collapse)[31,36]. This has direct implications in neurodegenerative diseases, such as Alzheimer's disease (contributing to the formation of the so-called neurofibrillary tangles[31,37,38]) and schizophrenia[39]. A similar effect of phosphorylation on tubulin binding and microtubule formation has been described for CRMP2A in Alzheimer's disease[40] and bipolar disorder[41], resulting in abnormal neurite outgrowth. In contrast to tubulin polymerization, an opposite effect has been described for CRMP2A and CRMP2B on tubulin branching[23], a process relevant to processes, such as ciliogenesis[42] and EMT[43].

Besides tubulin, CRMP2B (but not CRMP2A) has been shown to also interact with other cytoskeleton-associated proteins (kinesin[44,45], dynein[46]) as well as ion (calcium and sodium) channels; the latter interaction is dependent on the CRMP2B

SUMOylation status[47,48].

Much less is known about the role of CRMP2A and CRMP2B in non-neuronal cells. Tahimic et al. first reported that phosphorylated CRMP2B can be found in mouse fibroblasts and that a drop in CRMP2B phosphorylation coincides with contact inhibition[49]. They also detected high levels of phosphorylated CRMP2B in a mouse tumor cell line. This first evidence on the potential role of CRMP2B in cancer was later followed by other reports showing that phosphorylated CRMP2B and/or CRMP2A can be detected in the nuclei of tumor cells and tumor biopsies[50,51] and its levels may be associated with poor overall survival in patients with non-small-cell lung cancer (NSCLC)[51]. Although the exact function of the CRMP2 proteins in cancer is overall very poorly understood, a recent study suggests that CRMP2B phosphorylation affects microtubule stability and bundling in ovarian cancer cells, similar to neurons. In this paper, the authors showed that CRMP2B can be phosphorylated at two novel residues (Y479 and Y499) by the FER kinase, thereby disrupting the microtubule-stabilizing activity of CRMP2B[52]. They then showed that this CRMP2B-tubulin interaction can be exploited therapeutically by combining FER kinase inhibitors with the microtubule-destabilizing and anti-cancer drug paclitaxel in order to enhance its cytotoxicity.

1.3 Epithelial-to-Mesenchymal Transition (EMT)

Epithelial-to-mesenchymal transition or EMT is a term describing the process of phenotypic transformation of cells from an epithelial into a mesenchymal state. During the process of EMT, epithelial cells end up losing their cell polarity and cell-

cell adhesion features, switching into a fibroblast-like elongated shape and acquiring migratory and invasive properties. As a result of this, EMT has been extensively studied in the context of cancer metastasis, where EMT is generally thought to precede the migration of cancer cells into distant sites[53]. Besides its role in metastasis, recent studies have linked EMT to stemness, proposing that partial (and not necessarily complete) EMT can be part of a stem cell-like signature[54], regardless of the ability of cells to metastasize[55]. Acquisition of partial EMT (where cells display mixed epithelial and mesenchymal features) and stemness is thought to give rise to aggressive clones of cancer stem cells (CSCs), which are highly resistant to metabolic stress[56], chemotherapy[57] and the immune system attack[58]. This allows them to evade death and eventually drive tumor initiation and regeneration post-chemotherapy. Apart from its significance in cancer biology, EMT has been shown to be an integral part of the following fundamental processes: a) organogenesis in the developing embryo (e.g. gastrulation, neural crest formation), also termed developmental EMT[59] and b) wound healing/organ fibrosis (e.g. heart regeneration post-injury), also termed pathological EMT[60,61].

Several different signaling pathways have been described to be involved in EMT, such as the PI3K/Akt, Ras/MAPK, Wnt/β-catenin and TGFβ/SMAD pathways[62] **(Fig. 1-2)**. These pathways can be activated in response to a variety of external stimuli, such as ligands (e.g. TGFβ, BMPs, cytokines) produced by cancer stroma cells (fibroblasts, macrophages etc.), hypoxia and mechanical stress[63]. Regardless of the nature/source of stimulation, these pathways seem to converge on certain transcription factors (TFs), whose activation is critical for the induction of the EMT program. The most important of these are Snail1 (Snail), Snail2 (Slug), TWIST1 and

ZEB1[64]. These TFs orchestrate the EMT process by positively or negatively regulating the expression of a wide number of downstream target genes that primarily affect cell adhesion and polarity but also other functions, such as metabolism[56,65] and apoptosis[66].

Unlike other cellular processes that involve major rearrangements and are terminal (e.g. senescence), EMT is dynamic and reversible. Mesenchymal cells can revert back to an epithelial state through an opposite process known as mesenchymal-to-epithelial transition (MET)[67]. This allows mesenchymal, metastatic cells that reach their target organ to 'settle' and grow in the new environment. The reversibility of EMT reflects the reversible nature of the underlying molecular mechanisms that drive EMT: epigenetic changes (acetylation and methylation affecting expression of master EMT TFs[68,69]) and fluctuating levels of the aforementioned ligands.

A

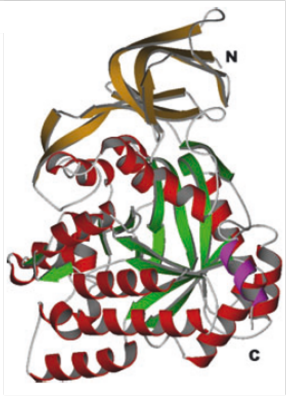

Main CRMP2B Domains

1. TIM barrel (core and largest fraction)
2. β-sheet (small domain)

B

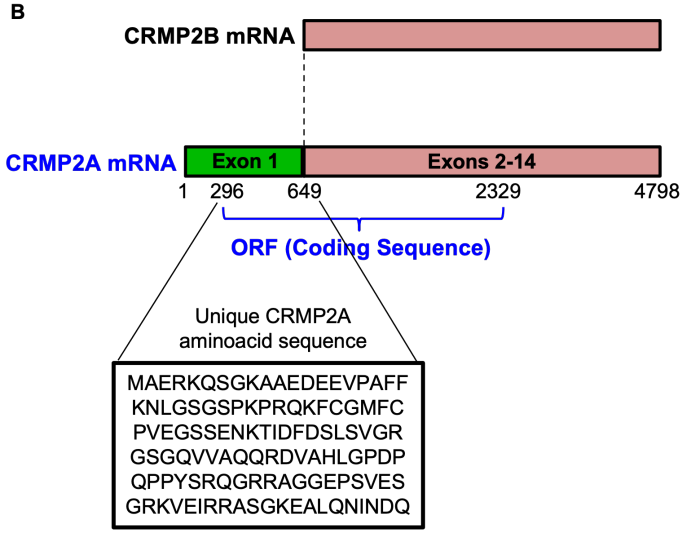

C **CRMP2A protein**
(predicted structural conformations)

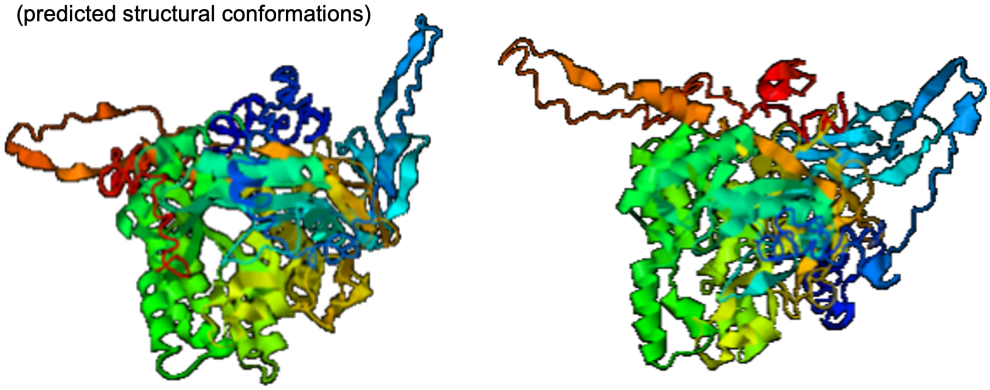

```
                    20        40        60        80        100       120
                    |         |         |         |         |         |
Sequence    MAERKQSGKAAEDEEVPAFFKNLGSGSPKPRQKFCGMFCPVEGSSENKTIDFDSLSVGRGSGQVVAQQRDVAHLGPDPQPPYSRQGRRAGGEPSVESGRKVEIRRASGKEALQNINDQSD
Prediction  CCCCCCCCCCCCCCCCHHHCCCCCCCCCHHHCCCCSSCCCCCCCCCCCCCCCCCCCCCCCCCCCCCCCCCCCCCCCCCCCCCCCCCCCCCCCCCCCCCCCCCCCCCCCCCCCCCCCCCCC
Conf.Score  950003666676566747651689999985010486321354643244445312146788888887778877777888887656677888765566776533457875444556667878
            H:Helix; S:Strand; C:Coil
```

Figure 1-1: Structural properties of the CRMP2A and CRMP2B proteins.

(A) Folding of the crystallized CRMP2B monomer and its main domains (Reprinted by permission from Wiley Publishing Company: Journal of Neurochemistry, The structure of human collapsin response mediator protein 2, a regulator of axonal growth, Pål Stenmark et al., Copyright 2006.) **(B)** Comparison of the mRNA sequences for CRMP2A and CRMP2B. The CRMP2A mRNA contains a unique nucleotide sequence (Exon 1; green rectangle) that is missing from the CRMP2B mRNA. The unique N-terminal amino acid sequence (118 amino acids) encoded by Exon 1 of the CRMP2A mRNA is shown in the box below. **(C)** Predicted three-dimensional protein structure of CRMP2A based on the iTASSER software. The two models with the highest probability scores are shown. The unique CRMP2A sequence includes amino acids that could participate in the formation of helices and strands.

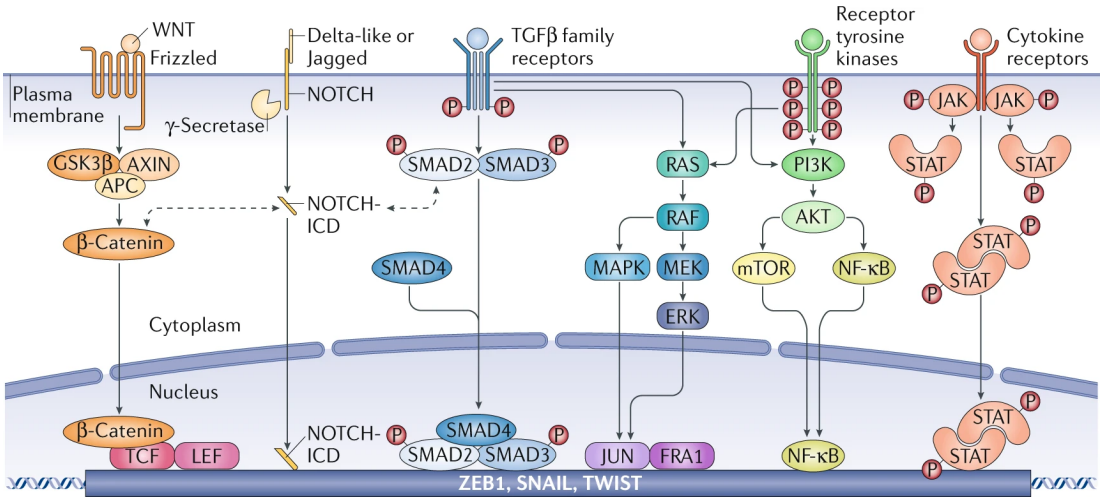

Figure 1-2: Signaling pathways that activate EMT. (Reprinted by permission from Springer Nature: Nature Reviews Molecular Cell Biology, New insights into the mechanisms of epithelial–mesenchymal transition and implications for cancer, Anushka Dongre & Robert Weinberg, Copyright 2018.)

References

1 Hanahan, D. & Weinberg, R. A. Hallmarks of cancer: the next generation. *Cell* **144**, 646-674, doi:10.1016/j.cell.2011.02.013 (2011).

2 Liberti, M. V. & Locasale, J. W. The Warburg Effect: How Does it Benefit Cancer Cells? *Trends Biochem Sci* **41**, 211-218, doi:10.1016/j.tibs.2015.12.001 (2016).

3 Yang, L., Venneti, S. & Nagrath, D. Glutaminolysis: A Hallmark of Cancer Metabolism. Annu Rev Biomed Eng 19, 163-194, doi:10.1146/annurev-bioeng-071516-044546 (2017).

4 Fan, J. et al. Glutamine-driven oxidative phosphorylation is a major ATP source in transformed mammalian cells in both normoxia and hypoxia. Mol Syst Biol 9, 712, doi:10.1038/msb.2013.65 (2013).

5 Metallo, C. M. et al. Reductive glutamine metabolism by IDH1 mediates lipogenesis under hypoxia. Nature 481, 380-384, doi:10.1038/nature10602 (2011).

6 Hosios, A. M. et al. Amino Acids Rather than Glucose Account for the Majority of Cell Mass in Proliferating Mammalian Cells. Dev Cell 36, 540-549, doi:10.1016/j.devcel.2016.02.012 (2016).

7 Kato, Y. et al. Acidic extracellular microenvironment and cancer. Cancer Cell Int 13, 89, doi:10.1186/1475-2867-13-89 (2013).

8 Wang, Z. et al. Targeting Glutaminolysis: New Perspectives to Understand Cancer Development and Novel Strategies for Potential Target Therapies. Front Oncol 10, 589508, doi:10.3389/fonc.2020.589508 (2020).

9 Faubert, B., Solmonson, A. & DeBerardinis, R. J. Metabolic reprogramming and cancer progression. *Science* **368**, doi:10.1126/science.aaw5473 (2020).

10 Liu, Y. & Yang, C. Oncometabolites in Cancer: Current Understanding and Challenges. Cancer Res 81, 2820-2823, doi:10.1158/0008-5472.CAN-20-3730 (2021).

11 Xu, W. et al. Oncometabolite 2-hydroxyglutarate is a competitive inhibitor of alpha-ketoglutarate-dependent dioxygenases. Cancer Cell 19, 17-30, doi:10.1016/j.ccr.2010.12.014 (2011).

12 Grassian, A. R. et al. Isocitrate dehydrogenase (IDH) mutations promote a reversible ZEB1/microRNA (miR)-200-dependent epithelial-mesenchymal transition (EMT). J Biol Chem 287, 42180-42194, doi:10.1074/jbc.M112.417832 (2012).

13 Colvin, H. et al. Oncometabolite D-2-Hydroxyglurate Directly Induces Epithelial-Mesenchymal Transition and is Associated with Distant Metastasis in Colorectal Cancer. Sci Rep 6, 36289, doi:10.1038/srep36289 (2016).

14 Dewhirst, M. W., Secomb, T. W., Ong, E. T., Hsu, R. & Gross, J. F. Determination of local oxygen consumption rates in tumors. *Cancer Res* **54**, 3333-3336 (1994).

15 Gatenby, R. A. & Gillies, R. J. Why do cancers have high aerobic glycolysis? *Nat Rev Cancer* **4**, 891-899, doi:10.1038/nrc1478 (2004).

16 Helmlinger, G., Yuan, F., Dellian, M. & Jain, R. K. Interstitial pH and pO2 gradients in solid tumors in vivo: high-resolution measurements reveal a lack of correlation. *Nat Med* **3**, 177-182, doi:10.1038/nm0297-177 (1997).

17 Sciacovelli, M. & Frezza, C. Metabolic reprogramming and epithelial-to-mesenchymal transition in cancer. *FEBS J* **284**, 3132-3144, doi:10.1111/febs.14090 (2017).

18 Majmundar, A. J., Wong, W. J. & Simon, M. C. Hypoxia-inducible factors and the response to hypoxic stress. *Mol Cell* **40**, 294-309, doi:10.1016/j.molcel.2010.09.022 (2010).

19 Hamajima, N. *et al.* A novel gene family defined by human dihydropyrimidinase and three related proteins with differential tissue distribution. *Gene* **180**, 157-163, doi:10.1016/s0378-1119(96)00445-3 (1996).

20 Goshima, Y., Nakamura, F., Strittmatter, P. & Strittmatter, S. M. Collapsin-induced growth cone collapse mediated by an intracellular protein related to UNC-33. *Nature* **376**, 509-514, doi:10.1038/376509a0 (1995).

21 Stenmark, P. *et al.* The structure of human collapsin response mediator protein 2, a regulator of axonal growth. *J Neurochem* **101**, 906-917, doi:10.1111/j.1471-4159.2006.04401.x (2007).

22 Myllykoski, M., Baumann, A., Hensley, K. & Kursula, P. Collapsin response mediator protein 2: high-resolution crystal structure sheds light on small-molecule binding, post-translational modifications, and conformational flexibility. *Amino Acids* **49**, 747-759, doi:10.1007/s00726-016-2376-z (2017).

23 Yuasa-Kawada, J. *et al.* Axonal morphogenesis controlled by antagonistic roles of two CRMP subtypes in microtubule organization. *Eur J Neurosci* **17**, 2329-2343, doi:10.1046/j.1460-9568.2003.02664.x (2003).

24 Bretin, S. *et al.* Differential expression of CRMP1, CRMP2A, CRMP2B, and CRMP5 in axons or dendrites of distinct neurons in the mouse brain. *J Comp Neurol* **486**, 1-17, doi:10.1002/cne.20465 (2005).

25 Liu, Y. *et al.* Functional variants in DPYSL2 sequence increase risk of schizophrenia and suggest a link to mTOR signaling. *G3 (Bethesda)* **5**, 61-72, doi:10.1534/g3.114.015636 (2014).

26 Wang, L. H. & Strittmatter, S. M. A family of rat CRMP genes is differentially expressed in the nervous system. *J Neurosci* **16**, 6197-6207 (1996).

27 Balastik, M. *et al.* Prolyl Isomerase Pin1 Regulates Axon Guidance by Stabilizing CRMP2A Selectively in Distal Axons. *Cell Rep* **13**, 812-828, doi:10.1016/j.celrep.2015.09.026 (2015).

28 Luo, Y., Raible, D. & Raper, J. A. Collapsin: a protein in brain that induces the collapse and paralysis of neuronal growth cones. *Cell* **75**, 217-227, doi:10.1016/0092-8674(93)80064-l (1993).

29 Mecollari, V., Nieuwenhuis, B. & Verhaagen, J. A perspective on the role of class III semaphorin signaling in central nervous system trauma. *Front Cell Neurosci* **8**, 328, doi:10.3389/fncel.2014.00328 (2014).

30 Fukata, Y. *et al.* CRMP-2 binds to tubulin heterodimers to promote microtubule assembly. *Nat Cell Biol* **4**, 583-591, doi:10.1038/ncb825 (2002).

31 Uchida, Y. *et al.* Semaphorin3A signalling is mediated via sequential Cdk5 and GSK3beta phosphorylation of CRMP2: implication of common phosphorylating mechanism underlying axon guidance and Alzheimer's

disease. *Genes Cells* **10**, 165-179, doi:10.1111/j.1365-2443.2005.00827.x (2005).

32 Yang, X. *et al.* Conventional protein kinase Cbeta-mediated phosphorylation inhibits collapsin response-mediated protein 2 proteolysis and alleviates ischemic injury in cultured cortical neurons and ischemic stroke-induced mice. *J Neurochem* **137**, 446-459, doi:10.1111/jnc.13538 (2016).

33 Winkler, S. C., Shimobayashi, E. & Kapfhammer, J. P. PKCgamma-Mediated Phosphorylation of CRMP2 Regulates Dendritic Outgrowth in Cerebellar Purkinje Cells. *Mol Neurobiol* **57**, 5150-5166, doi:10.1007/s12035-020-02038-6 (2020).

34 Arimura, N. *et al.* Phosphorylation of collapsin response mediator protein-2 by Rho-kinase. Evidence for two separate signaling pathways for growth cone collapse. *J Biol Chem* **275**, 23973-23980, doi:10.1074/jbc.M001032200 (2000).

35 Hou, S. T. *et al.* CaMKII phosphorylates collapsin response mediator protein 2 and modulates axonal damage during glutamate excitotoxicity. *J Neurochem* **111**, 870-881, doi:10.1111/j.1471-4159.2009.06375.x (2009).

36 Yoshimura, T. *et al.* GSK-3beta regulates phosphorylation of CRMP-2 and neuronal polarity. *Cell* **120**, 137-149, doi:10.1016/j.cell.2004.11.012 (2005).

37 Gu, Y., Hamajima, N. & Ihara, Y. Neurofibrillary tangle-associated collapsin response mediator protein-2 (CRMP-2) is highly phosphorylated on Thr-509, Ser-518, and Ser-522. *Biochemistry* **39**, 4267-4275, doi:10.1021/bi992323h (2000).

38 Yoshida, H., Watanabe, A. & Ihara, Y. Collapsin response mediator protein-2 is associated with neurofibrillary tangles in Alzheimer's disease. *J Biol Chem* **273**, 9761-9768, doi:10.1074/jbc.273.16.9761 (1998).

39 Pham, X. *et al.* The DPYSL2 gene connects mTOR and schizophrenia. *Transl Psychiatry* **6**, e933, doi:10.1038/tp.2016.204 (2016).

40 Petratos, S. *et al.* The beta-amyloid protein of Alzheimer's disease increases neuronal CRMP-2 phosphorylation by a Rho-GTP mechanism. *Brain* **131**, 90-108, doi:10.1093/brain/awm260 (2008).

41 Tobe, B. T. D. *et al.* Probing the lithium-response pathway in hiPSCs implicates the phosphoregulatory set-point for a cytoskeletal modulator in bipolar pathogenesis. *Proc Natl Acad Sci U S A* **114**, E4462-E4471, doi:10.1073/pnas.1700111114 (2017).

42 Ou, Y. *et al.* Targeting of CRMP-2 to the primary cilium is modulated by GSK-3beta. *PLoS One* **7**, e48773, doi:10.1371/journal.pone.0048773 (2012).

43 Guen, V. J. *et al.* EMT programs promote basal mammary stem cell and tumor-initiating cell stemness by inducing primary ciliogenesis and Hedgehog signaling. *Proc Natl Acad Sci U S A* **114**, E10532-E10539, doi:10.1073/pnas.1711534114 (2017).

44 Kawano, Y. *et al.* CRMP-2 is involved in kinesin-1-dependent transport of the Sra-1/WAVE1 complex and axon formation. *Mol Cell Biol* **25**, 9920-9935, doi:10.1128/MCB.25.22.9920-9935.2005 (2005).

45 Mokhtar, S. H. *et al.* Amyloid-beta-dependent phosphorylation of collapsin response mediator protein-2 dissociates kinesin in Alzheimer's disease. *Neural Regen Res* **13**, 1066-1080, doi:10.4103/1673-5374.233451 (2018).

46 Arimura, N. *et al.* CRMP-2 directly binds to cytoplasmic dynein and interferes with its activity. *J Neurochem* **111**, 380-390, doi:10.1111/j.1471-4159.2009.06317.x (2009).

47 Dustrude, E. T. *et al.* Hierarchical CRMP2 posttranslational modifications control NaV1.7 function. *Proc Natl Acad Sci U S A* **113**, E8443-E8452, doi:10.1073/pnas.1610531113 (2016).

48 Ju, W. *et al.* SUMOylation alters CRMP2 regulation of calcium influx in sensory neurons. *Channels (Austin)* **7**, 153-159, doi:10.4161/chan.24224 (2013).

49 Tahimic, C. G. *et al.* Evidence for a role of Collapsin response mediator protein-2 in signaling pathways that regulate the proliferation of non-neuronal cells. *Biochem Biophys Res Commun* **340**, 1244-1250, doi:10.1016/j.bbrc.2005.12.132 (2006).

50 Grant, N. J. *et al.* Phosphorylation of a splice variant of collapsin response mediator protein 2 in the nucleus of tumour cells links cyclin dependent kinase-5 to oncogenesis. *BMC Cancer* **15**, 885, doi:10.1186/s12885-015-1691-1 (2015).

51 Oliemuller, E. *et al.* Phosphorylated tubulin adaptor protein CRMP-2 as prognostic marker and candidate therapeutic target for NSCLC. *Int J Cancer* **132**, 1986-1995, doi:10.1002/ijc.27881 (2013).

52 Zheng, Y. *et al.* Tuning microtubule dynamics to enhance cancer therapy by modulating FER-mediated CRMP2 phosphorylation. *Nat Commun* **9**, 476, doi:10.1038/s41467-017-02811-7 (2018).

53 Pastushenko, I. & Blanpain, C. EMT Transition States during Tumor Progression and Metastasis. *Trends Cell Biol* **29**, 212-226, doi:10.1016/j.tcb.2018.12.001 (2019).

54 Wilson, M. M., Weinberg, R. A., Lees, J. A. & Guen, V. J. Emerging Mechanisms by which EMT Programs Control Stemness. *Trends Cancer* **6**, 775-780, doi:10.1016/j.trecan.2020.03.011 (2020).

55 Fischer, K. R. *et al.* Epithelial-to-mesenchymal transition is not required for lung metastasis but contributes to chemoresistance. *Nature* **527**, 472-476, doi:10.1038/nature15748 (2015).

56 Kim, N. H. *et al.* Snail reprograms glucose metabolism by repressing phosphofructokinase PFKP allowing cancer cell survival under metabolic stress. *Nat Commun* **8**, 14374, doi:10.1038/ncomms14374 (2017).

57 Li, X. *et al.* Intrinsic resistance of tumorigenic breast cancer cells to chemotherapy. *J Natl Cancer Inst* **100**, 672-679, doi:10.1093/jnci/djn123 (2008).

58 Kudo-Saito, C., Shirako, H., Takeuchi, T. & Kawakami, Y. Cancer metastasis is accelerated through immunosuppression during Snail-induced EMT of cancer cells. *Cancer Cell* **15**, 195-206, doi:10.1016/j.ccr.2009.01.023 (2009).

59 Lim, J. & Thiery, J. P. Epithelial-mesenchymal transitions: insights from development. *Development* **139**, 3471-3486, doi:10.1242/dev.071209 (2012).

60 Haensel, D. & Dai, X. Epithelial-to-mesenchymal transition in cutaneous wound healing: Where we are and where we are heading. *Dev Dyn* **247**, 473-480, doi:10.1002/dvdy.24561 (2018).

61 Stone, R. C. et al. Epithelial-mesenchymal transition in tissue repair and fibrosis. Cell Tissue Res 365, 495-506, doi:10.1007/s00441-016-2464-0 (2016).

62 Gonzalez, D. M. & Medici, D. Signaling mechanisms of the epithelial-mesenchymal transition. *Sci Signal* **7**, re8, doi:10.1126/scisignal.2005189 (2014).

63 Dongre, A. & Weinberg, R. A. New insights into the mechanisms of epithelial-mesenchymal transition and implications for cancer. *Nat Rev Mol Cell Biol* **20**, 69-84, doi:10.1038/s41580-018-0080-4 (2019).

64 Stemmler, M. P., Eccles, R. L., Brabletz, S. & Brabletz, T. Non-redundant functions of EMT transcription factors. *Nat Cell Biol* **21**, 102-112, doi:10.1038/s41556-018-0196-y (2019).

65 Yu, J. *et al.* Snail Enhances Glycolysis in the Epithelial-Mesenchymal Transition Process by Targeting FBP1 in Gastric Cancer. *Cell Physiol Biochem* **43**, 31-38, doi:10.1159/000480314 (2017).

66 Vega, S. *et al.* Snail blocks the cell cycle and confers resistance to cell death. *Genes Dev* **18**, 1131-1143, doi:10.1101/gad.294104 (2004).

67 Pei, D., Shu, X., Gassama-Diagne, A. & Thiery, J. P. Mesenchymal-epithelial transition in development and reprogramming. *Nat Cell Biol* **21**, 44-53, doi:10.1038/s41556-018-0195-z (2019).

68 Lin, Y., Dong, C. & Zhou, B. P. Epigenetic regulation of EMT: the Snail story. *Curr Pharm Des* **20**, 1698-1705, doi:10.2174/13816128113199990512 (2014).

69 Sun, L. & Fang, J. Epigenetic regulation of epithelial-mesenchymal transition. *Cell Mol Life Sci* **73**, 4493-4515, doi:10.1007/s00018-016-2303-1 (2016).

Chapter Two: A reversible metabolic stress-sensitive regulation of Collapsin Response Mediator Protein 2A orchestrates cytoskeletal remodeling and EMT, increasing metastatic potential in cancer

This chapter is under revision in the journal Cell Reports.

Abstract

Critical cell fate decisions like proliferation, migration, EMT or stemness need to be coordinated and responsive to environmental inputs, like metabolic stresses. A complex metabolic and molecular rewiring allows cancer cells to both survive their (often) limited fuel supply and support the need for increased biomass production[1,2]. A partial EMT phenotype with features of cancer stem cells ~~(CSC)~~ is now recognised as a critical feature of aggressive/metastatic tumors, but the mechanism(s) that promote it and its relation to metabolic stress remain unknown[3]. Here we show an unexpected cytoplasmic, reversible induction of Collapsin Response Mediator Protein 2A (CRMP2A) in cancer cells, in response to diverse metabolic stresses, including low glucose and hypoxia. CRMP2A, a microtubule-associated protein (MAP), has been implicated in the mechanism of neuronal axonal growth and in different neurodegenerative diseases[4-6]. Luciferase and ChIP assays showed that CRMP2A transcription is regulated by HIF-1α (positively) and c-Myc (negatively). Loss of CRMP2A (siRNA or CRISPR) increased both microtubule polymerization and branching and caused an extensive cytoskeletal remodeling, an EMT phenotype, expression of CSC markers, increased migration, chemoresistance and increased glutamine utilization toward energy production and pyrimidine synthesis under low-glucose conditions; and in the absence of any exogenous triggers for EMT. Xenotransplanted CRMP2A-deficient cells showed increased tumor initiation capacity, tumor size and metastasis, compared to parental cells. Metastatic cell lines have less CRMP2A than non-metastatic primary cell lines. In a cohort of prostate cancer patients with biopsies from both primary tumors and distant metastases, there

was decreased CRMP2A expression in the metastatic versus primary tumors. We show for the first time that CRMP2A is reversibly induced under the metabolic stress frequently encountered in tumors and represses the energy-intensive EMT[7]; while its loss (for example in the vicinity of blood vessels where there is less metabolic stress) increases EMT/stemness and metastatic potential. This is the first evidence that the loss of a single MAP, like CRMP2A in cancer cells, is sufficient to orchestrate a complex cytoskeletal, metabolic and EMT/stemness program, promoting growth and metastasis, which may have significant clinical implications. CRMP2A is an endogenous molecular brake on cancer EMT/stemness, and its loss increases the aggressiveness and metastatic potential of tumors.

Introduction

We speculated that there may be a central, metabolic stress-responsive mechanism that may ignite and coordinate an adaptive cell fate (EMT) response in cancer cells, while keeping it suppressed in normal cells. While EMT offers several survival advantages for tumor cells in growing tumors as it allows them to migrate and escape the metabolic stress (including limited supply of glucose and oxygen) that they frequently encounter, it is by itself energetically demanding[7,8]. Furthermore, under metabolic stress, EMT may be catastrophic for normal adult epithelial cells, since they will lose their essential features like polarity, cell-cell adhesions and cell-basal membrane adhesions, which are critical for tissue integrity. This raises the intriguing possibility that there may exist an endogenous inhibitor of EMT, particularly under metabolic stress. Since many transcription factors have been shown to ignite diverse EMT programs in response to exogenous signals (typically microenvironment-derived)[3], it is possible that this inhibitor may not be an upstream regulator (i.e. transcription factor), but rather a downstream regulator at a converging stage of EMT programs, such as the cytoskeleton, which is known to regulate trafficking of multiple transcription factors toward the nucleus.

Here we report that various types of metabolic stress, particularly low glucose and hypoxia, increase the unphosphorylated form of the microtubule-associated protein Collapsin Response Mediator Protein 2A (CRMP2A) *in vitro* and in hypoperfused areas of tumors *in vivo*. While the drop in phosphorylated CRMP2A promotes microtubule formation (polymerization), the concomitant increase in total, unphosphorylated CRMP2A inhibits branching of microtubules and ciliogenesis,

which is part of the EMT program. By contrast, lack of all forms of CRMP2A in CRMP2A-deficient cells allows for an extensive cytoskeletal remodeling with increased microtubule polymerization and branching, particularly under metabolic stress. In turn, this increases the invasive and metastatic potential of cancer and normal cells. Besides EMT properties, CRMP2A-deficient cells have a cancer stem cell signature and an altered metabolic profile (increased glutamine utilization towards pyrimidine synthesis) that is compatible with both EMT and stemness.

Results

2.1 Collapsin Response Mediator Protein 2A is a novel metabolic stress-sensitive protein.

Since mitochondria are critical sensors and processors of several fuels (glucose, lipids, amino acids and oxygen)[9], we first used a model in which cancer cells were exposed to either severe mitochondrial stress with mitochondrial inhibitors, or to more physiologic stresses found in tumors (e.g. low glucose or mild-moderate hypoxia). We sought to discover the induction of proteins that may be induced under all the stresses and have the potential to regulate several critical and diverse pathways, from metabolic rewiring and proliferation/apoptosis, to (partial) EMT and stemness, now all recognized as important features of aggressive and metastatic tumors. We exposed A549 lung cancer cells (a widely studied cell line with a low metastatic potential) to either strong mitochondrial inhibitors (ethidium bromide, which completely inhibits mitochondrial function by impairing mitochondrial DNA synthesis[10]; partial inhibitors of mitochondrial function (SIRT3 siRNA[11] or Electron Transport Chain (ETC) inhibitors, such as the ATP synthase inhibitor Oligomycin); as well as fuel restriction by exposing the cells to low glucose or physiologic hypoxia (i.e. pO_2 ~ 30 mmHg with normal pH and pCO_2 using buffers), as opposed to anoxia. As an indicator of the cells' response, we first looked at c-Myc, because it is responsive to several metabolic inputs like nutrient availability (glucose and glutamine)[12] and it is a master transcription factor with over 500 documented target genes[13] involved in all of the aforementioned adaptive cellular processes. We found that c-Myc 2 (the main c-Myc isoform) decreased in response to most forms of

metabolic stress **(Fig. 2-1A)**. However, all the c-Myc immunoblots, revealed the induction of a higher molecular weight protein in response to metabolic stressors **(Fig. 2-1A)**, which was reversible upon their removal **(Fig. 2-1B)**. This protein did not match the known molecular weights of c-Myc 1 (58 kDa) and c-Myc 2 (55 kDa)[14] and 5 different c-Myc siRNAs, each targeting a different area (exon) of the c-Myc mRNA, did not affect its expression to the levels expected if this protein represented another c-Myc isoform **(Fig. 2-1C)**. Moreover, out of 3 commercially available antibodies that we tested, only one detected this protein **(Fig. 2-1D)**. However, its dynamic regulation and its inverse relationship with c-Myc suggested that it may actually represent a novel c-Myc-regulated gene product (inhibitory effect) with a potentially important role in the response to metabolic stress. Intrigued by this unexpected finding, we characterized this protein, using a 2D gel- and Mass Spectrometry-based proteomic approach **(Fig. 2-2A-C)**, which identified 4 candidate proteins **(Fig. 2-2D)**. Searching for the presence of sequence similarities between the predicted epitope of the cross-reactive c-Myc antibody (CST #5605) and the 4 proteins detected by Mass Spec, we identified this protein as the Collapsin Response Mediator Protein 2A (CRMP2A) **(Fig. 2-2E)**. CRMP2A is a microtubule-associated protein (MAP) that has been implicated in neuron development and axonal growth[4,5,15-17], but very little is known about its potential role in cancer[18].

2.2 Expression and transcriptional regulation of CRMP2A in normal and cancer cells.

Immunoblot analysis of total CRMP2A levels in A549 cells and small airway epithelial cells (SAEC, the non-cancerous counterparts of A549 cells) using both a previously validated monoclonal CRMP2A-specific antibody (a gift from Dr. Veronique Rogemond, INSERM, France)[15] as well as a commercially available CRMP2A/B antibody (that recognized both the A and B isoforms of CRMP2), showed increased levels of the CRMP2A (but not CRMP2B) protein in the A549 cells **(Fig. 2-3A)**. These data were also confirmed by another custom-made monoclonal anti-CRMP2A antibody (GenScript Biotech Corporation, Piscataway, NJ, USA) (data not shown). The CRMP2A increase in the A549 versus SAEC was also evident at the mRNA level, using CRMP2A-specific primers and droplet digital PCR **(Fig. 2-3B)**. Further comparison of the CRMP2A protein levels between normal cells (melanocytes, human skin and foreskin fibroblasts and human embryonic kidney cells) and various cancer cell lines (melanoma, glioblastoma, bone and breast cancer) also showed higher CRMP2A levels in most of the cancer cells **(Fig. 2-3C)**, although the embryonic cells had somewhat increased levels compared to normal epithelial cells, like SAEC and melanocytes.

In silico analysis of the putative CRMP2A promoter together with data mining from publicly available databases (Ensembl, UCSC) revealed the presence of putative binding motifs for c-Myc as well as for the transcription factors HIF-1α, STAT3, NFATc2, NF-κb and SMAD3/4 **(Fig. 2-3D)**. Of them, we focused on c-Myc and HIF-1α as they are both important metabolic stress-related (i.e. glucose and

oxygen, respectively) transcription factors and with wide target gene networks. Interestingly, we found that c-Myc and HIF-1α had opposing effects on CRMP2A expression. Inhibition of c-Myc with siRNA significantly induced CRMP2A mRNA and protein levels **(Fig. 2-3E)**, while inhibition of HIF-1α (siRNA) inhibited CRMP2A expression **(Fig. 2-3F)**. This is in keeping with the frequently antagonizing roles of c-Myc and HIF-1α on gene expression[19]. Importantly, both c-Myc and HIF-1α had a mild or no effect at all on CRMP2B expression **(Fig. 2-3E-F)**.

2.3 The unphosphorylated form of CRMP2A is transcriptionally induced in cancer and normal cells exposed to metabolic stress

We next repeated our earlier experiments with metabolic stressors in A549 cells, now utilizing CRMP2A-specific antibodies and primers. We found that total CRMP2A was induced both at the protein and at the mRNA level, after exposure to several mitochondrial/metabolic stresses: ethidium bromide **(Fig. 2-4A)**, SIRT3 siRNA **(Fig. 2-4B)**, hypoxia **(Fig. 2-4C)**, Ciprofloxacin (an inhibitor of the mitochondrial DNA topoisomerase)[20] **(Fig. 2-4D)** or siRNA-inhibition of TFAM (a master transcription factor of mtDNA-encoded genes)[21] **(Fig. 2-4E)**. In cells exposed to low glucose (we used 2.5 mM for 24-48 h based on the results of a combined dose-response and time-course experiment, **Fig. 2-5A**), we once again found that CRMP2A, but not CRMP2B was induced both at the mRNA and protein level **(Fig. 2-4F)**. An induction of CRMP2A in response to metabolic stress was also observed in two other cancer cell lines (HeLa: cervix, MDA-MB-231: breast) **(Fig. 2-5B)** as well as two non-cancerous (but proliferative) cell lines (skin fibroblasts, MEFs) **(Fig. 2-**

5C). Interestingly, while total CRMP2A levels increased by metabolic stress, phosphorylation of CRMP2A (which is important for inhibiting microtubule polymerization in neurons[5,6]) decreased at Thr619 ($p<0.05$) and Ser627 ($p=0.1$), i.e. sites known to be phosphorylated by GSK-3β[6] and CDK5[4], respectively; both kinases are involved in metabolic signaling[22].

2.4 Differential activity of c-Myc and HIF-1α as well as changes in gene methylation may be involved in the induction of CRMP2A under stress

Under the same metabolic stress conditions described above, whole cell **(Fig. 2-6A)** and nuclear (**Fig. 2-6B-C**) levels of c-Myc and phospho-c-Myc (Ser62) (the stable and transcriptionally active form of c-Myc[23]) decreased, while total **(Fig. 2-6D)** and nuclear **(Fig. 2-6E)** HIF-1α levels increased in A549 cells. At the same time increased CRMP2A was detected exclusively in the cytoplasm **(Fig. 2-6B)**. This combination of events was intriguing as we earlier showed opposing effects of c-Myc and HIF-1α silencing on CRMP2A expression. Probing the putative CRMP2A promoter with a chromatin immunoprecipitation assay (ChIP) at baseline and after exposure to stress (hypoxia) showed significantly increased HIF-1α and decreased c-Myc binding (c-Myc: three different sites, HIF-1α: two different sites) ($p=0.06$ for one of the HIF-1α binding sites) (**Fig. 2-6F**). Moreover, a custom luciferase assay of the putative CRMP2A promoter, using a construct containing most of the c-Myc and HIF-1α binding sites studied in ChIP, revealed an overall increased activity during hypoxia **(Fig. 2-6G** and **Fig. 2-7)**. Altogether, these data suggest that a decrease in c-

Myc along with an increase in HIF-1α could be responsible for the induction of CRMP2A during metabolic stress.

Lastly, treatment of A549 cells with two different agents that result in decreased DNA methylation, 5-aza-2′-deoxycytidine (5-aza-dC), a DNA methyltransferase inhibitor, and FIDAS-5, a methionine S-adenosyltransferase 2A (MAT2A) inhibitor, showed that CRMP2A (but not CRMP2B) increased at the protein level in a dose-dependent manner **(Fig. 2-8)**. 5-aza-dC (10 μM) also increased the CRMP2A mRNA by 2-fold in A549 cells and by 4-fold in SAEC. These data suggest that promoter methylation (an epigenetic regulatory mechanism that is known to respond to metabolic signals[2]) is operational in cancer, but perhaps even more in normal epithelial cells.

2.5 Levels of total and phosphorylated CRMP2A affect tubulin polymerization and microtubule branching.

We then examined whether the decrease in p-CRMP2A and increase in total CRMP2A under metabolic stress could potentially affect the microtubule/cytoskeletal organization. In neurons, p-CRMP2A inhibits microtubule polymerization[5,6], while total CRMP2A inhibits branching of microtubules[17]. We first used a microtubule/tubulin assay that quantifies the amount of polymerized tubulin (microtubules) vs. unpolymerized tubulin and found that control cells had lower polymerization at baseline compared to low glucose (a condition that decreases p-CRMP2A); while CRMP2A-deficient cells (first generated by siRNA and later on confirmed in cells deleting CRMP2A using CRISPR; see below) had higher

polymerization at baseline compared to control cells, a difference that persisted under low glucose, suggesting almost maximal polymerization at baseline **(Fig. 2-9A)**. Microtubule polymerization and stability is required for subsequent branching. To study microtubule branching, we used α-tubulin staining and high-resolution confocal image analysis[24,25] and found that control cells had less microtubule branching than CRMP2A-deficient cells both at baseline, and under low glucose conditions **(Fig. 2-9B-C)**.

Furthermore, since tetramerization of CRMP2 has also been implicated in tubulin stability[26], we performed cross-linking experiments with DSS, which did not show differences in the formation of CRMP2 tetramers between baseline and low glucose conditions **(Fig. 2-10)**. Therefore, we concluded that the observed effects on microtubule polymerization/stability are predominantly due to the decrease or loss of p-CRMP2A; whereas the effects on microtubule branching are due to the loss of total, unphosphorylated CRMP2A. Thus, loss of CRMP2A is sufficient to increase both microtubule polymerization and branching in cancer cells, promoting a more organized and complex cytoskeletal network, important for several different functions, including trafficking of transcription factors (e.g. c-Myc[27]) and EMT[28].

2.6 Loss of CRMP2A induces an EMT phenotype with cytoskeletal reorganization and increased invasive and metastatic properties.

In order to study the potential association between CRMP2A and EMT, we first exposed A549 cells to rhTGF-β1, a well-known chemical inducer of EMT[29], and found that it significantly decreased mRNA and protein levels of CRMP2A, while

inducing clear phenotypic (spindle shape) and molecular features of EMT, including Snail and Slug induction, N-/E-cadherin switch, decreased tubulin acetylation[30] and increased tubulin detyrosination[31] **(Fig. 2-11A)**. The decrease by rhTGF-β1 suggested that CRMP2A may play a role in the EMT signaling of cancer cells. We then utilized the CRISPR/Cas9 technology to permanently delete CRMP2A expression in A549 cells and created two different clones of CRMP2A-deficient cells **(Fig. 2-12)**. CRMP2A-deficient cells from both clones had clear morphological (switching from cobblestone to mesenchymal-like spindle-shaped cells) and molecular (Snail and Slug induction, N-/E-cadherin switch and alterations in tubulin post-translational modifications, PTMs) features of EMT, which were even more pronounced than the changes observed with rhTGF-β1 **(Fig. 2-11B)**. Interestingly, these cells were also less responsive to further Snail induction after rhTGF-β1 stimulation, suggesting that the EMT potential is maximized at baseline when CRMP2A is absent **(Fig. 2-11C)**. Another notable difference observed in the CRMP2A-deficient cells was the F-actin reorganization, switching from thin, cortical filaments (epithelial-like) into thick, parallel contractile bundles **(Fig. 2-11D)**.

To determine whether the cytoskeletal changes induced by the loss of (p-) CRMP2A are important and upstream of EMT induction, we treated CRMP2A-deficient cells with microtubule-destabilizing agents (colchicine and nocodazole). Both drugs inhibited Snail expression, suggesting that the cytoskeletal remodeling induced by the decrease in (p-)CRMP2A (by either metabolic stress or by gene deletion), is upstream of EMT induction **(Fig. 2-11E)**.

We confirmed the aforementioned changes in morphology and protein expression by performing an unbiased pathway and Gene Ontology (GO) enrichment

analysis of a GeneChip assay, in CRMP2A-deficient vs parental control cells. We found that EMT and metastasis-associated genes comprised the largest group of differentially regulated genes **(Fig. 2-13A)**. The genes that showed the biggest change in expression are shown in **Fig. 2-13B**. Compared to the chronic loss of CRMP2A (CRISPR), short-acute deficiency of CRMP2A achieved with siRNA, also resulted in similar EMT-related changes in A549 cells. Comparison of the GeneChip profiles between CRMP2A-deficient and siRNA CRMP2A-treated A549 cells revealed a shared signature of 10 important EMT-related changes in mRNAs (marked with an asterisk in **Fig. 2-13B**), including Snail upregulation. Note that a panel of putative cancer stem cell markers is also present in this comparison in addition to classic EMT markers (i.e. upregulation of CD44, Sox2). We confirmed the Snail induction in the siRNA CRMP2A-treated cells, along with an N-/E-cadherin switch and a decrease in acetyl-Tubulin (similar to CRMP2A-deficient cells), on immunoblots **(Fig. 2-11F)**. In keeping with the protein expression, brightfield microscopy revealed again a more spindle-like morphology of the siRNA- vs. scramble-treated cells **(Fig. 2-11G)**. A similar induction of Snail after acute loss of CRMP2A was seen in the SW480 colon cancer cells **(Fig. 2-11H)**. Furthermore, a strong negative correlation ($r \approx -0.94$) between Snail and CRMP2A protein levels was also observed in a panel of eight different human cancer cell lines (6 commercial cell lines and two primary, patient-derived glioblastoma cell lines from our previous work[32]) **(Fig. 2-11I)**. Intriguingly, besides A549 lung cancer cells, loss of CRMP2A allowed for Snail induction in renal proximal tubules (normal epithelial cells) as well, but this occurred only during concomitant exposure to low glucose, suggesting that CRMP2A may act as a brake to

EMT in both normal and cancer epithelial cells, particularly under metabolic stress **(Fig. 2-11J)**.

In order to examine whether the acquisition of EMT-compatible molecular features in CRMP2A-deficient cells could also predict an increased invasive and metastatic potential, we first performed *in vitro* assays, which showed that the supernatant from CRMP2A-deficient cells had increased activity of secreted MMP-2 (an enzyme that is able to degrade the extracellular matrix during metastasis)[33] **(Fig. 2-14A)** and invaded more through the basement membrane of a trans-well invasion assay compared to parental cells **(Fig. 2-14B)**. The increased invasive and metastatic potential of the CRMP2A-deficient cells was confirmed *in vivo* using a tail vein injection model of human A549 cells in immunodeficient mice[34]. We injected a group of 19 mice, 10 with parental and 9 with CRMP2A-deficient (CRISPR) cells via tail vein injection. We found that 30% of the parental A549 cells-injected mice had evidence of metastasis in the right lung (qRT-PCR detecting amplification of GAPDH specific to human, but not mouse cells) (mean: 0.159 copies/µl on ddPCR). By contrast, 67% of the CRMP2A-deficient A549 cells-injected mice had evidence of metastasis (mean: 143 copies/µl) **(Fig. 2-14C)**. In the lungs with the highest amount of human GAPDH mRNA we also provide immunoblot evidence of the presence of human-specific HLA-A protein. This 37% increase in the ability of CRMP2A-deficient cells to colonize the mice lungs is in keeping with our *in vitro* data.

In order to show causality between CRMP2A levels, Snail induction and metastatic potential, we first used two colon cancer cell lines derived from the *same* patient, from the primary tumor (SW480, *in situ*) and a lymph node metastasis (SW620, metastatic). CRMP2A protein levels were significantly decreased in the

metastatic cells and this was associated with increased Snail and decreased E-cadherin levels. When CRMP2A was inhibited in the primary tumor cells using siRNA, Snail expression increased to levels similar to those observed in the metastatic colon cancer cells **(Fig. 2-14D)**. Moreover, within different breast cancer cell lines, HTB-126 cells (established from a carcinoma *in situ*) had much higher CRMP2A levels and much lower Snail levels compared to a locally invasive (CRL-2321) and a metastatic cell line (MCF-7) **(Fig. 2-14E)**. Secondly, we studied primary tumor and metastatic biopsies from a group of 10 patients with prostate cancer before the initiation of any therapy (except for one patient that received androgen deprivation therapy). Patient demographic and clinical data are listed in **Fig. 2-16**. We used ddPCR to measure the CRMP2A mRNA levels in primary and metastatic tumor sites and found that CRMP2A expression was significantly reduced in the metastatic sites by an average of 400% **(Fig. 2-15A)**. Primary tumors also had significantly higher CRMP2A levels (average of 40%) than normal prostate tissues **(Fig. 2-15B)**. Lastly, we observed a moderate ($r \approx -0.43$) but significant negative correlation between Snail and CRMP2A mRNA levels in our total of 27 samples from normal prostate, primary tumors and metastatic tumor tissues **(Fig. 2-15C)**. These findings were further confirmed by immunofluorescence analysis of CRMP2A and Snail levels in tumor (primary and metastatic) and normal prostate biopsies from a representative patient **(Fig. 2-15D)**. The strength of our (admittedly small) cohort of prostate cancer patients is that it allowed a direct comparison of normal, prostate cancer and distal metastatic tissues from the *same* patient.

2.7 Loss of CRMP2A increases stemness in cancer cells.

A growing body of literature suggests that acquisition of a partial EMT phenotype in cancer cells leads to cells that also share features of cancer stem cells (CSCs), such as: chemoresistance, resistance to metabolic stress and increased tumor-initiating potential[3]. "Stemness" was also a signature that emerged from the unbiased gene chip analysis in CRMP2A-deficient compared to parental cells **(Fig. 2-13B)**. First, we looked at the expression level of commonly used putative CSC markers, i.e. CD44, CD133 and Sox2[3,35,36]. All three were significantly induced in our CRMP2A-deficient cells compared to parental cells **(Fig. 2-17A)**. Second, we found that exposure to genotoxic stress (Gemcitabine alone or the combination of Cisplatin and Gemcitabine chemotherapies, both relevant to non-small cell lung cancer, i.e. A549 cells) caused less apoptosis (measured by cleaved Caspase 3 levels) in the CRMP2A-deficient cells compared to parental cells **(Fig. 2-17B)**. Third, exposure to low (2.5 mM) glucose for 24 h showed a small proliferative advantage (albeit not significant, p=0.08) of CRMP2A-deficient compared to parental cells **(Fig. 2-17C)**. In order to study any differences in growth and tumor forming capacity *in vivo*, we used a xenotransplant model, which is associated with metabolic stress (low glucose and oxygen), due to the poor vascular supply, especially during the tumor initiation phase. We first injected a small amount (10^4) of CRMP2A-deficient cells in the right flank and an equal number of parental cells in the left flank of immunodeficient mice and we followed the growth of tumors over time. At 4 weeks, 100% of the CRMP2A-deficient cells and only 65% of the parental cells had *palpable* evidence of small tumors. By 7 weeks, the CRMP2A-deficient cells-injected sites had larger tumors

compared to the parental cells-injected sites (trend towards significance, p=0.16) **(Fig. 2-17D)**. An even bigger and significant difference in favor of the CRMP2A-deficient tumors was observed after s.c. injection of a larger number of cells ($3x10^6$) **(Fig. 2-17E)**. At the same time, CRMP2A-deficient xenografts retained increased expression of the EMT markers Snail, Slug and N-cadherin **(Fig. 2-18)**. The increased growth of the CRMP2A-deficient xenografts was confirmed with a ki67 staining (a marker of proliferation) **(Fig. 2-17F)**. Taken together, these data suggest that loss of CRMP2A not only induced a partial EMT phenotype but also initiated a (cancer) stem cell-like program in A549 cells.

In order to study the pattern of CRMP2A expression within the tumor, we co-stained parental tumors with antibodies against von Willebrand factor (to detect endothelial cells in capillaries), HIF-1a, DAPI (to mark nuclei) and CRMP2A. We randomly selected areas within 100 μm versus >100 μm away from capillaries, because it has been shown that in solid tumors the gradient of oxygen (and glucose) drops significantly beyond 100 μm from microvessels/capillaries[37-39]. We found that, as expected, in the former, HIF-1a was mostly absent (due to oxygen-induced degradation), while in the latter it was present with a clear nuclear localization. In the areas where HIF-1a was active, CRMP2A was much more expressed than in areas where HIF-1a was absent, with a very strong positive correlation ($r \approx +0.9$) between the two **(Fig. 2-17G)**.

2.8 CRMP2A-deficient cells have a metabolic rearrangement that promotes nucleotide synthesis under low glucose conditions.

We hypothesized that the survival advantage of the CRMP2A-deficient cells at low glucose conditions, which also supports their enhanced ability for tumor initiation, growth and metastasis, may be supported by a parallel metabolic remodeling. We speculated that this may include a shift towards increased glutamine utilization, which would be consistent with EMT[40]. Increased glutaminolysis could significantly support the energetic and biosynthetic requirements of proliferation during exposure to low nutrients (e.g. glucose) as it would allow cancer cells to both fuel the TCA cycle (ATP production) and provide metabolic intermediates for nucleotide (pyrimidine and purine) production for DNA/RNA synthesis, which is compromised under low glucose conditions due to decreased activity of the glucose-dependent pentose phosphate pathway. Measurement of the mitochondrial respiration showed that CRMP2A-deficient cells had a 49% higher oxygen consumption rate (OCR, measured by Seahorse) at baseline (25 mM glucose and 4 mM glutamine) compared to parental cells and this difference was retained (47%) under low glucose conditions (2.5 mM glucose and 4 mM glutamine, 24 h) **(Fig. 2-19A)**. In a different experiment, when glutamine was the only fuel (i.e. 0 mM glucose), the difference in OCR between parental and CRMP2A-deficient cells was completely lost (overlapping solid and dotted green lines on the graph). In addition, using a medium consisting of [^{13}C,^{15}N]-labeled glutamine (4mM) and unlabeled glucose (2.5mM or 25mM), we found that TCA cycle metabolites (α-KG and fumarate) were mostly derived from glutamine in either parental or CRMP2A-deficient cells **(Fig. 2-19B)**.

Together, these data suggested that glutamine was not preferentially used in CRMP2A-deficient vs. parental cells to support the TCA cycle and ATP production.

We thus turned our attention to the second arm of our hypothesis that glutamine may be diverted into non-TCA cycle-related pathways in CRMP2A-deficient cells to support nucleotide synthesis, especially under low glucose conditions. To explore this possibility, we first compared the levels of glutaminases 1 and 2 (GLS1/2) and glutamate dehydrogenase (GDH), which catalyze the first and second committed steps of glutamine metabolism respectively and found much higher GLS1/2 levels in the CRMP2A-deficient cells **(Fig. 2-19C)**. However, the opposite was observed with glutamate dehydrogenase (GDH), which converts glutamate to α-KG **(Fig. 2-19C)**. This would be in keeping with utilization of glutamate in other pathways such as aspartate production, which has been shown to be of critical importance for the pyrimidine and purine biosynthetic pathways in cancer[41,42]. Indeed, Mass Spec analysis of the metabolites in the de novo pyrimidine synthesis pathway at baseline and low glucose conditions revealed that CRMP2A-deficient cells were able to maintain a higher production of glutamate, aspartate, N-carbamoylaspartate, orotate and UMP at low glucose conditions compared to parental cells (**Fig. 2-19D** and **Fig. 2-20**). Using labeled [^{13}C,^{15}N]-glutamine we found that CRMP2A-deficient cells showed increased incorporation of labeled carbon and nitrogen into glutamate, aspartate and UMP as well as the UMP derivative thymidine in the DNA (**Fig. 2-19E** and **Fig. 2-21A**). Altogether, these findings suggest that CRMP2A-deficient cells have a metabolic profile, where glutamine is more efficiently utilized under low glucose conditions to support nucleotide synthesis and proliferation, as shown in the schematic **(Fig. 2-19F)**. Besides the de novo synthesis pathway, cancer cells can also

produce pyrimidines through the salvage pathway by converting free uridine (from RNA degradation) into UMP through the activity of uridine-cytidine kinase 2 (UCK2); this enzyme is overexpressed in several human cancers, including lung cancer[43]. When compared between parental and CRMP2A-deficient cells at baseline and low glucose conditions, we saw that UCK2 levels significantly decreased in parental cells exposed to low glucose, whereas CRMP2A-deficient cells retained their UCK2 levels. This difference in the regulation of UCK2 may also contribute to the ability of CRMP2A-deficient cells to maintain UMP synthesis during metabolic stress **(Fig. 2-21B)**.

Discussion

Overall, our work uncovers a novel cell fate-determining role for CRMP2A. To our knowledge, this is one of the very few descriptions of how a single MAP can orchestrate cell fate under metabolic stress in cancer. Loss of CRMP2A induced a combined EMT and stemness phenotype in cancer epithelial cells[44,45] and this was independent of any external factors[46]. EMT is rarely a cell autonomous process. Signals arising from the tumor stroma cells (adipocytes, fibroblasts, immune cells and vascular endothelial cells) secrete EMT-inducing factors like TGF-β1[3], but in our model EMT and stemness took place in the absence of these cells and factors.

Our findings suggest a mechanism where, in response to metabolic stress, CRMP2A prevents cells from entering the energetically demanding state of EMT. This (defense) mechanism may be relevant to all types of cells with EMT potential but may have direct implications for the function and integrity of epithelial cells,

whose physiologic role is to provide structure to tissues (and thus cannot afford to enter EMT under even mild metabolic stress).

Our work describes a dynamic and metabolic stress-sensitive mechanism for the suppression or induction of EMT. A very important aspect of CRMP2A's ability to suppress EMT is that it is reversible, whether the metabolic stress is due to mitochondrial inhibitors or more physiologic stresses like those encountered by most solid tumors. For example, in areas of the tumor that are under metabolic stress (i.e. low O_2 and glucose), a decrease in the metabolism-sensitive GSK3β- and CDK5-dependent phosphorylation of CRMP2A leads to an early increase in microtubule polymerization, an effect that could potentially prime cells for further cytoskeletal remodeling and EMT. But the activation of HIF-1α (responsive to low O_2) or a decrease in c-Myc (responsive to low glucose), result in a robust increase in total CRMP2A levels, which inhibits microtubule branching, preventing further cytoskeletal remodeling. We propose that this is a critical event that puts a reversible brake in EMT/stemness **(Fig. 2-19G)**. In contrast, once mature vessels are established in the tumor, relieving the metabolic stress, HIF-1α activity will decrease while c-Myc will increase, both causing a decrease of CRMP2A **(Fig. 2-17G)**, releasing the brake and promoting EMT/stemness **(Fig. 2-19G)**. This induction of EMT in the proximity of mature vessels, will facilitate the spread of these transitioned cells through the vasculature to distal organs.

Our work is also in keeping with the demonstration that in some breast cancer subtypes, inhibition of ciliogenesis is sufficient to repress EMT/stemness[47]. This is because CRMP2 is also known to be involved in the regulation of cilia formation[48], a process closely linked to microtubule dynamics. In other words, direct effects on cilia

or microtubules are sufficient to induce complex downstream effects toward EMT/stemness, as our data with Snail induction by microtubule destabilizers also suggested.

Although more studies may be needed to completely understand CRMP2A's role in EMT, our work is important because it describes a complex and comprehensive molecular and metabolic remodeling caused by the loss of a single MAP, increasing survival and metastatic potential of cancer cells, which could be exploited in cancer therapeutic and biomarker discovery strategies. We also believe that the discovery of this endogenous brake on EMT, its reversible nature and its responsiveness to metabolic signals, will significantly advance our understanding of the EMT/stemness phenotype of aggressive and metastatic cancer cells.

Materials and Methods

Cell culture

All cancer cells (ATCC) were grown in Dulbecco's Modified Eagle Medium (DMEM, Gibco) supplemented with 10% FBS and 1% P/S at 9% CO_2 according to ATCC recommendations. Human Small Airway Epithelial cells (SAEpiC) and Renal Proximal Tubular Epithelial cells (PTEpiC) were purchased from ScienCell (CA, USA) and grown in SAEpiCM and EpiCM media (ScienCell) respectively at 5% CO_2. For generation of ρ^- A549 cells (partial depletion of mtDNA), cells were treated with 50 ng ml^{-1} EtBr for 14 days. For glucose starvation experiments, cells were grown to 70-80% confluence, washed once with PBS and then cultured in glucose-free DMEM (Gibco, Cat: 11966-025), supplemented with 10% FBS, 1% P/S and 2.5 mM of D-(+)-glucose (Sigma-Aldrich, G7021). For detection of secreted BMP2 in

the supernatant, A549 cells were cultured in serum-free DMEM for 24 h before harvesting in order to decrease the albumin content in the supernatant.

Confocal microscopy

All images were obtained on a ZEISS LSM 710 confocal microscope (Carl ZEISS AG, Oberkochen, Germany), equipped with a GaAsp detector and the Airyscan module, allowing us to obtain super-resolution images with lateral resolution of ~140 nm. Images were acquired with a 40x Oil objective at optimal pixel size and interval (for z-stacks) based on the zoom factor and the fluorophores used in each experiment. After acquisition, the images were processed with the ImageJ software. **Brightfield Images**: Brightfield images were acquired on an EVOS™ XL Core Imaging System (Thermo Fisher Scientific).

Immunoblotting

Cultured cells were collected and lysed in ice-cold RIPA buffer for 30 min with vortexing every 10 min. Samples were then spun down at 10,000 rpm for 25 min in a tabletop centrifuge (Eppendorf AG, Hamburg, Germany). After centrifugation, the supernatant was collected. Protein concentration was quantified with a BCA kit (Thermo Fisher Scientific, Waltham, MA, USA) and measured on a SpectraMax iD3 plate reader (Molecular Devices, San Jose, CA, USA). Samples were then diluted to a final concentration of 0.5-2 mg ml^{-1} in RIPA buffer and 2x Laemmli Sample Buffer (Sigma-Aldrich). Finally, they were boiled at 95 ˚C for 5 min. Tumor xenografts (s.c. tumor model) and lung tissues (*in vivo* metastasis model) were lysed in ice-cold RIPA

buffer via sonication with 10 quick pulses using a handheld homogenizer (VWR, PA, USA). All subsequent steps were carried out as described above for cultured cell lysates. All samples were loaded on SDS-PAGE polyacrylamide gels. Proteins were then transferred onto 0.45 nm pore nitrocellulose membranes using a Trans-blot Turbo transfer system (Bio Rad, Hercules, CA, USA) according to the manufacturer's instructions. After transferring, membranes were incubated with Ponceau S (Thermo Fisher Scientific) to verify efficient transferring of the proteins. Membranes were then washed with TBST and blocked with 5% non-fat dry milk (or BSA) in TBST for 1 h at room temperature. Membranes were then incubated with the primary antibody in 1% non-fat dry milk (or BSA) in TBST overnight at 4 ˚C with gentle rotation. The following day, membranes were washed with TBST and incubated with the appropriate HRP-conjugated secondary antibodies (Cell Signaling Technology, Danvers, MA, USA). Proteins were detected after incubation of the membranes with ECL buffer (Thermo Fisher Scientific) and visualized on a ChemiDoc imaging system (Bio-Rad). If stripping was necessary, a commercially available stripping buffer was used (Thermo Fisher Scientific), followed by blocking with 5% milk (or BSA) for 45-60 min at room temperature and incubation with the primary and secondary antibodies as described above. **(Disuccinimidyl Suberate) DSS cross-linking**: Protein cross-linking in cells with DSS was performed as described previously[49]. Supernatants containing cross-linked proteins were quantified using a BCA kit. Samples were diluted to a final concentration of 0.75 mg ml^{-1} in RIPA buffer and 2x Laemmli Sample Buffer, and analyzed via immunoblotting as described above.

Customized monoclonal antibody production against Collapsin Response Mediator Protein 2A (CRMP2A) (GenScript)

The following peptide was chosen to be synthesized and used as the antigenic determinant (epitope) based on models projecting both maximum reactivity against the CRMP2A protein and low cross-reactivity with the CRMP2B protein: CVPAFFKNLGSGSPKPRQKF (phase I). After KLH conjugation and mouse immunization (phase II), 7 reactive clones were isolated and fused, and the respective antisera were screened/validated using immunoblots (phase III). Of the 7 screened clones, clone 6D9 showed the most promise as it produced no signal in a protein lysate from CRM2A-deficient cells and a strong signal in a lysate from CRMP2A-transfected cells. This clone was expanded (phase IV), followed by antibody purification from the respective cell supernatant (phase V). 2.51 mg of purified anti-CRMP2A antibody were delivered to us, concluding the project.

Trypan Blue Exclusion Assay

Adherent cells were washed with PBS, collected by trypsinization and added to the cell suspension of floating cells; the total pool of cells was then centrifuged at 1,500 rpm for 3 min. After removing the supernatant, cells were resuspended in PBS. 1 part of cell suspension was mixed with 1 part of 0.4% Trypan Blue solution (Sigma-Aldrich) and the mixture was incubated for 3 min at room temperature. Trypan Blue uptake was analyzed on a Countess II FL Automated Cell Counter (Thermo Fisher Scientific).

siRNA transfection

Premade siRNA constructs were purchased from Ambion (TX, USA); the custom anti-CRMP2A construct was manufactured by iDT (Coralville, Iowa, USA). Cells were grown in 35 mm dishes to 50-60% confluence and then transfected in antibiotic-free medium with 30 pmol siRNA diluted in Opti-MEM medium (Gibco, Waltham, MA, USA) and mixed with Lipofectamine^{TM} RNAiMAX reagent (Invitrogen). The mixture was incubated for 10 min at room temperature and then added to the cells, which were collected at 72 h post-transfection.

Immunofluorescence

Cultured cells were grown on coverslips and treated accordingly for each experiment. They were fixed with 2% PFA at 37 ˚C for 10 min, followed by permeabilization with Triton X-100 (0.25%) for 10 min. They were then treated with Image-iT FX Signal Enhancer (Thermo Fisher Scientific) for 30 min at room temperature and blocked for 1 h with 10% serum from the host of the secondary antibody. Cells were incubated with the primary antibodies overnight at 4 ˚C. The following day, incubation with the secondary antibodies was performed for 1h at room temperature in the dark. Finally, they were counterstained with 1 μM DAPI (Molecular Probes, Oregon, USA) at room temperature for 10 min, prior to mounting in ProLong Glass (Thermo Fisher Scientific). Tissue slices (5 μm thickness) from tumor xenografts or human prostate cancer biopsies were processed and stained similar to cultured cells. **F-actin staining**: The CytoPainter Phalloidin-iFluor 488 Reagent (Abcam, Cambridge, UK) was used according to the manufacturer's instructions. **Image**

analysis: All images were analyzed on ImageJ. In order to quantify microtubule branching, raw images were processed using the skewness function of the LPIXEL plugin of ImageJ.

GeneChip

200 ng of total RNA was labeled using the Affymetrix GeneChip 3' IVT PLUS Reagent kit (Thermo Fisher Scientific). Poly-A controls were added to each sample at the beginning of the labeling. 10 μg of fragmented, biotin-modified RNA was hybridized to the Affymetrix PrimeView Human microarray in the Affymetrix GeneChip Hybridization Oven 645 (Thermo Fisher Scientific) set at 45 ˚C with 60 rpm for 16 h. Hybridization controls were added to each sample before the arrays were hybridized. The arrays were washed and stained with Affymetrix GeneChip Wash and Stain Kit on the Affymetrix GeneChip Fluidics Station 450 (Thermo Fisher Scientific). Arrays were scanned on the Affymetrix GeneChip Scanner 3000 7G (Thermo Fisher Scientific) to generate the raw data files.

GO (Gene Ontology) enrichment analysis

We used the GeneAnalytics software (LifeMap Sciences, CA, USA) to identify enriched GO terms in the CRMP2A-deficient cells based on the fold change in gene expression (GeneChip assay) between CRMP2A-deficient and parental cells. The top 48 GO terms are plotted.

Chromatin Immunoprecipitation (ChIP) assay

ChIP was performed using the SimpleChIP Enzymatic Chromatin IP Kit (Thermo Fisher Scientific) according to the manufacturer's instructions. Briefly, approximately $4x10^6$ A549 parental cells (exposed to normoxia or hypoxia for 48 h) were used for each IP. Proteins were cross-linked to DNA by adding formaldehyde directly to culture medium to a final concentration of 1% and incubated for 10 min at room temperature. Following addition of glycine for 5 min (room temperature), medium was aspirated, and cells were washed and scraped in ice-cold PBS containing protease inhibitors. Cells were centrifuged for 6 min at 2,000*g* at 4 ˚C. Cell pellets were sequentially treated with 1 ml per IP of Buffer A and Buffer B in order to extract the nuclei, which were then resuspended in 1x ChIP Buffer and treated with micrococcal nuclease for 20 min at 37 ˚C. Nuclear lysates were sonicated at 4 ˚C to reduce DNA length to approximately 150-900 bp. Debris was removed by centrifugation for 10 min at 9,400 rpm at 4 ˚C in a microcentrifuge. ChIP-grade antibodies (c-Myc, HIF-1α or 1 μg Rabbit IgG) were then added to approximately 5 μg of DNA lysate per IP reaction and incubated overnight at 4 ˚C with rotation. The next day, antibodies were immobilized by adding 30 μl of Protein G magnetic beads (slurry) and incubating the mixture for 2 h at 4 ˚C. The beads were sequentially washed: 3x for 5 min using a Low Salt Wash Buffer and 1x with a High Salt Wash Buffer before eluting chromatin at 65 ˚C for 30 min with gentle vortexing (1,200 rpm). Following elution, ChIP products were treated with Proteinase K at 65 ˚C for 2 h and purified using DNA purification spin columns. Elution was performed with 50 μl nuclease-free water. Real-time PCR was performed with a SYBR™ Green PCR

Master Mix (Applied Biosystems) using 2 μl product as template for each reaction. Amplifications were carried out as follows: at 95 ˚C for 10 min, followed by 40 cycles at 95 ˚C (15 s), 60 ˚C (1 min). Results for each IP reaction were expressed as percent of the total input chromatin using the following formula: Percent Input = 2% x $2^{[Ct\ (2\%Input\ Sample) - Ct\ (IP\ Sample)]}$, Ct: Threshold cycle of PCR reaction.

Two Hypoxia Response Element (HRE) consensus binding sites (5'-ACGTG-3') for HIF-1α were identified at 1,400 bp (position #1) and 1,200 bp (position #2) upstream of the transcription site (TSS) of the CRMP2A gene. For c-Myc, we identified a consensus binding site (5'-CACGTG-3') for the Myc-Max heterodimer (E-box) at 1,200 bp (overlapping with the second predicted HIF-1α site) upstream of the TSS. Moreover, mining of publicly available RNA-seq databases (Genomatix) revealed the presence of two putative binding sites (variations of the consensus binding site 5'-CACGTG-3') at 490 bp (position #2) and 400 bp (position #3) upstream of the TSS. The custom-made ChIP primers used for each putative site are listed in the Table below (**Table 1**). Please note that the primers used for the c-Myc (Position #1) and HIF-1α (Position #1) are the same, since the putative binding sites for c-Myc and HIF-1α at this area overlap and the same primers can give information about the binding of both transcription factors.

Table 1. Custom-made primers used in the ChIP assay

ChIP reaction	Forward Primer	Reverse Primer
c-Myc (Position #1)	TTCTGCAGGATTTTGCCACT	ACCAGGGGGCAATTAGATTT
c-Myc (Position #2)	TTTCCCATCCATCAGCTCAC	CTCTCCTCCACCTGCCT
c-Myc (Position #3)	GTGCCCTGCCCGATACTTAC	ACCAGCTAATGGATGCGGAG

HIF-1α (Position #1)	TTCTGCAGGATTTTGCCACT	ACCAGGGGGCAATTAGATTT
HIF-1α (Position #2)	CTACCTCCTACTCCGCACCA	ACAAACTGAAACCCCCTTCC

2D gel electrophoresis (2-DE) and Mass Spectrometry-based identification of Collapsin Response Mediator Protein 2A (CRMP2A)

Vehicle- and EtBr-treated cells were collected on ice and fractionated using a commercially available kit (Thermo Fisher Scientific). Cytoplasmic extracts were processed with the ReadyPrep 2-D cleanup kit (Bio-Rad) in order to remove ionic contaminants (detergents, lipids, phenolic compounds) and precipitate the proteins. Following precipitation, the protein pellets were solubilized in IEF/2D-compatible rehydration buffer containing 7 M urea, 2 M thiourea, 1.2% CHAPS, 0.5% ampholytes and Destreak Reagent (GE Healthcare Life Sciences, ON, Canada). Each sample was run in duplicate. IEF was performed using Immobiline DryStrips (pH range 3-11 NL, 24 cm) according to the manufacturer's instructions on an Ettan IPGphor system (GE Healthcare). Prior to SDS-PAGE, strips were equilibrated sequentially in buffer containing 50 mM Tris (pH 6.8), 6 M urea, 30% glycerol, 2% SDS, 0.1% bromophenol blue and either 0.1% DTT or 0.25% iodoacetamide respectively. SDS-PAGE (10% polyacrylamide gels) was performed on an Ettan DALTsix Large Vertical System (GE Healthcare). Following electrophoresis, gels were either transferred on nitrocellulose membranes (immunoblotting; replicate 1) or stained with a Coomassie Brilliant Blue R-250 dye (Bio-Rad) (replicate 2).

Upon immunoblotting, we found that the EtBr sample ("high" in the unknown protein) produced a single and strong signal at approximately the same molecular

weight (70-75 kDa) as our original one-dimensional Western blot, using the same anti-c-Myc antibody (Cell Signaling Technology, #5605). This signal was not detectable in the Vehicle sample ("low" in the unknown protein) **(Fig. 2-2C)**. Based on this observation, we reasoned that this signal may represent the true signal for the unknown protein and turned our attention to the area of the Coomassie-stained gel (EtBr "high" sample) with the same coordinates. We were able to identify four distinct protein spots in this area, manually extract them and submit them for Mass Spec analysis **(Fig. 2-2D)**. Analysis of each spot returned a unique protein as our candidate unknown protein: Glycine-tRNA ligase (GARS), Lysine-tRNA ligase (KARS), CTP Synthase 1 (CTPS1) and Collapsin Response Mediator Protein 2A (CRMP2A). Peptide coverage was at least 25% for three out of four proteins, suggesting that their detection was not the result of a random, exogenous contamination.

We then decided to perform an *in silico* analysis in order to estimate the sequence similarity of each of the four candidate proteins with the epitope that the c-Myc antibody (CST #5605) could be recognizing. Since the immunoblot signal for our unknown protein was the result of antibody cross-reactivity, this type of analysis would give us important clues as to which Mass Spec hits we should first turn our attention to. Although the exact epitope sequence is proprietary (as is the case with the vast majority of commercially available antibodies), after personal communication with the production company (Cell Signaling Technology) we were informed that the epitope is linear (continuous), lies within the first 30 amino acids and around the amino acid (D; Aspartate) at position 15 of the human c-Myc 2

protein. Considering that linear antibody epitopes are usually 5-8 amino acids long, we blasted different epitopes of this length against the PubMed human proteome database (*BLASTp* suite), looking for epitopes that would be specific to c-Myc and therefore could have been used by the company to generate the antibody. The six amino acid long-epitope LDYDSV (pos. 14-19) returned BLAST results with the highest c-Myc specificity, prompting us to focus our attention on this as the most likely epitope for the c-Myc antibody. We then performed a protein-protein BLAST analysis of this epitope against the sequences of the four proteins identified by Mass Spec. We were surprised to discover that CRMP2A had an N-terminal amino acid run (IDFDSL, pos. 50-55) that could be reactive with the c-Myc antibody based on *in silico* prediction models as it bore similarity with the LDYDSV epitope. This is because the second (D; Aspartate), fourth (D; Aspartate) and fifth (S; Serine) amino acids were identical between the two sequences, whereas the amino acids in the other three positions had considerable structural similarities (e.g., L; Leucine on the c-Myc protein vs. I; Isoleucine on the CRMP2A protein at position 1) **(Fig. 2-2E)**. None of the other three proteins (GARS, KARS and CTPS1) showed such sequence similarity, prompting us to focus on CRMP2A as our most likely candidate for being the unknown protein.

CRISPR/Cas9 Genome Editing

Guide RNAs (gRNAs) designed to target the CRMP2A gene were prepared by mixing equimolar amounts of Alt-R CRISPR-Cas9 tracrRNA, ATTO-550 (iDT) and Alt-R CRISPR-Cas9 crRNA (iDT), then annealed as previously described[50]. Briefly,

gRNAs were incubated at 98 ˚C for 5 min, then cooled to 4 ˚C over the course of 60 min. Ribonucleoprotein (RNP) complexes were assembled prior to transfection by adding equimolar amounts of Cas9 (New England Biolabs) to the previously prepared gRNA. RNP complexes were transfected into A549 cells using Lipofectamine™ CRISPRMAX (Invitrogen) according to the manufacturer's instructions. 24 h following transfection, cells were singly sorted into a 96-well plate based on the presence of the ATTO-550 fluorescent marker using a BD FACS Aria III instrument (Flow Cytometry Core, University of Alberta). Following sufficient clonal expansion, gDNA was extracted using the QuickExtract™ DNA Extraction Solution (Lucigen, Middleton, WI, USA) according to manufacturer's instructions. Briefly, 500 µL of cells were pelleted at 300*g* for 5 min, then washed once with PBS (pH 7.4) and re-pelleted. Cell pellets were resuspended in 100 µL of QuickExtract™ solution (Lucigen) and moved to a thermocycler running the following program: 65 ˚C for 10 min, 68 ˚C for 10 min, and 98 ˚C for 3 min. Isolated gDNA was used directly as template for PCR amplification of the CRMP2A Cas9 target site. PCR amplification products were purified via the QIAquick PCR Purification Kit (Qiagen, Hilden, Germany) and analyzed via Sanger sequencing for Cas9-mediated gene disruption. Candidates that demonstrated the presence of indel(s) at the desired site were further validated for CRMP2A protein knockout by immunoblotting.

Custom CRMP2A Luciferase Assay

The Wild-type (WT) construct of the human CRMP2A promoter (range: -1,200 to +96 relative to the TSS) was cloned into a pGL4.20[luc2/Puro] expression vector

(Promega, Madison, WI, USA). The pGL4.73[hRluc/SV40] was used as reporter vector (Promega). Cells were grown to 70-80% confluence in 12-well plates and then co-transfected with the expression (900 ng) and reporter (100 ng) plasmids using Lipofectamine^{TM} 2000 reagent (Invitrogen). 48 h post-transfection, cells were transferred and maintained in normoxia or hypoxia for 48 h, before harvesting. Luciferase activity in the cells was analyzed using a dual luciferase reporter assay kit (Promega). The CRMP2A Firefly activity was normalized to the Renilla luminescence.

Gelatin Zymography

A549 cells were cultured in serum-free DMEM for 24 h before harvesting. Cell culture supernatants were collected on ice, concentrated 8-10x using 10 kDa MW cut-off columns (Abcam), mixed with 4x Laemmli buffer (without beta-mercaptoethanol to preserve the enzymatic activity of secreted proteins) and boiled at 95 ˚C for 6 min before loading on a 7.5% SDS-PAGE gel, containing gelatin. Following electrophoresis, gel was rinsed twice with ddH_2O and washed 2x for 30 min with washing buffer (2.5% Triton X-100, 50 mM Tris-HCl, pH 7.5, 5 mM $CaCl_2$ and 1 μM $ZnCl_2$ in water) to remove residual SDS. Gel was then rinsed with incubation buffer (1% Triton X-100, 50 mM Tris-HCl, pH 7.5, 5 mM $CaCl_2$ and 1 μM $ZnCl_2$ in water) for 5-10 min at 37 ˚C under agitation. After addition of fresh incubation buffer, the gel was incubated for 24 h at 37 ˚C. The next day, the gel was stained with a Coomassie Brilliant Blue R-250 dye and finally destained until band visualization.

In vitro Cell Invasion Assay

A549 (parental or CRMP2A-deficient) cells were serum starved for 24 h prior to plating them into the top chambers of a Boyden-like chamber in serum-free medium. The bottom chambers were filled with complete (10% FBS, 1% P/S) DMEM medium to stimulate migration through an 8 μm polycarbonate (PC) membrane (coated with basement membrane extract), separating the top and bottom chambers. After overnight incubation at 37 ˚C, invading cells in the bottom chamber were washed twice and incubated with Cell Dissociation Solution/Calcein AM for 1 h at 37 ˚C in order to dissociate cells from the PC membrane and label them with Calcein AM (internalized Calcein AM gets cleaved by intracellular esterases to generate free Calcein, which fluoresces brightly). Fluorescence was measured on a SpectraMax iD3 plate reader (Molecular Devices) at 485 nm excitation, 520 nm emission.

Seahorse Analyzer

Oxygen consumption (OCR) and extracellular acidification (ECAR) rates were assessed using a Seahorse XF24 Extracellular Flux Analyzer (Agilent, Santa Clara, CA, USA) according to the manufacturer's instructions. Briefly, A549 cells were seeded and cultured overnight in Seahorse XF-24 plates at a density of $2x10^4$ cells per well. The next day, plating medium was removed and replaced with bicarbonate-free Seahorse XF Base medium without phenol red (Agilent) supplemented with 4 mM glutamine and either 25 mM (baseline), 2.5 mM (low) or 0 mM glucose. Following incubation of the cells in the CO_2-free incubator for 1 h, cells were placed in the Seahorse Analyzer. OCR and ECAR were calculated using 3 min mix and 3 min

measure cycles. After the run, cells were washed with PBS and lysed in 100 µl per well of RIPA buffer (supplemented with protease inhibitors) for 30 min at 4 ˚C with constant agitation. Protein concentration was measured with a BCA assay and used to normalize the OCR and ECAR values. At least 4 replicate wells were used per group.

Metabolite Extraction and Mass Spectrometry

A549 cells were cultured in triplicates in 10 cm dishes until they reached 70-80% confluence. Cells were then switched to either complete medium (25 mM glucose, 4 mM glutamine) or "low glucose" medium (2.5 mM glucose, 4 mM glutamine) for 24 h. For stable isotope-labeling studies, DMEM medium without glucose and glutamine (Gibco) was supplemented with dialyzed FBS (Gibco), D-glucose (25 or 2.5 mM) and 4 mM [$^{13}C_5$,$^{15}N_2$]-L-Glutamine (Sigma-Aldrich). 24 h post-medium change, cells were washed 3x with 1 ml and scraped in 2 ml of cold 0.9% NaCl solution, followed by centrifugation at 550*g* for 5 min at 4 ˚C. Cell pellets were re-suspended in an ice-cold mixture of methanol and ddH_2O (80:20 v/v) containing a Succinic Acid-d_6 internal standard (C/D/N Isotopes, Quebec, Canada). Samples were periodically vortexed, then sonicated (10 pulses, 50% intensity) and centrifuged at 13,000 rpm for 10 min to pellet cell debris, lipids and proteins. Supernatants were collected and the extraction procedure was repeated one more time. The combined supernatants containing metabolites were transferred to a new set of tubes and concentrated using a SpeedVac vacuum concentrator (Thermo Fisher Scientific). The dried metabolites were resuspended in 100 µl of LC/MS-grade water/acetonitrile (60:40 v/v) (Fisher Scientific) before Mass Spec analysis. In order to measure [^{13}C,^{15}N]-thymidine,

gDNA was isolated from treated cells using the AllPrep DNA/RNA Mini Kit (Qiagen), denatured at 100 ˚C for 3 min and then sequentially digested using the following enzymes: a) nuclease P1 (Sigma-Aldrich) at 45 ˚C for 2 h, b) phosphodiesterase I (Sigma-Aldrich) at 37 ˚C for 2 h and c) alkaline phosphatase (Sigma-Aldrich) at 37 ˚C for 1 h. Samples were measured immediately after processing.

1 mg ml^{-1} stock solutions of orotic acid and ureidosuccinate standards were prepared in water containing 10 mM ammonium acetate at pH 9.4, adjusted with ammonium hydroxide. All other standard solutions were made in water, set to 1 mg ml^{-1} and stored at -20 ˚C prior to use. They were diluted in water/acetonitrile (60:40, v/v) at different working concentrations before HPLC/MS analysis.

Standard and sample solutions were analyzed using an Aria MX HPLC system (Thermo Fisher Scientific) coupled to Orbitrap Elite Mass spectrometer (Thermo Fisher Scientific). The Xcalibur software v. 2.2 (Thermo Fisher Scientific) was used for data acquisition and analysis. For determination of TCA cycle metabolites, an Xbridge BEH 150 mm x 2.1 mm Amide column, 2.5 µm particle size (Waters, Milford, MA) was employed for LC separations. The column temperature was controlled at 25 ˚C. The mobile phase A was acetonitrile; phase B was 10 mM ammonium acetate in 95:5 water/acetonitrile at pH 9.4, adjusted using ammonium hydroxide. The gradient was as follows: 0-2 min, 15% B; 2-11 min, linear gradient to 35% B; 11-20 min, linear gradient to 85% B; 20-21 min, back to 15% B and hold for 8 min. The flow rate of the mobile phase was 200 µl min^{-1} and the cycle time was 29

min/injection. The orbitrap mass spectrometer was operated under electrospray negative ion mode. Ionization voltage was set at -2.5 kV. Nitrogen was used as sheath gas, aux gas and sweep gas. They were set at sheath gas 25, aux gas 20 and sweep gas 3 (arbitrary units). The ion source temperature and capillary temperature were at 300 ˚C and 325 ˚C respectively. Acquisition was carried out in full scan mode with mass range from 70 to 1,000 amu with resolving power set to a nominal value of 120,000 at full width half-maximum at m/z 400. Mass calibration and tuning was done by infusing of LTQ Velos ESI Negative Ion Calibration Solution (Thermo Fisher Scientific) prior to performing HPLC/MS analysis. For determination of [^{13}C,^{15}N]-thymidine in DNA samples, a YMC Carotenoid C30 column 100 mm x 2.0 mm, 3 μm particle size (YMC America, Inc., Devens, MA) was employed for HPLC separation. The mobile phase A was 0.1% formic acid in water and B was 0.1% formic acid in methanol. The gradient was as follows: 0-1 min, 10% B; 1-6 min, linear gradient to 50% B; 6-7 min, back to 10%B and hold for 5 min. The mobile phase flow rate was 200 μl min^{-1} and cycle time 12 min/injection. The orbitrap mass spectrometer was operated under atmospheric pressure chemical ionization (APCI) positive ion mode. Ionization current was set at 5 μA. Mass calibration and tuning was done by infusing of LTQ Velos ESI positive Ion Calibration Solution (Thermo Fisher Scientific). The other parameters were the same as above.

For determination of TCA cycle metabolites, a ten-point calibration curve of target compounds with concentration range from 0.005 μg ml^{-1} to 25 μg ml^{-1} was constructed based on the peak area ratio of the target compounds/internal standard versus the target compounds concentration. The target compounds concentration was

extrapolated from this calibration curve. For analysis of [^{13}C,^{15}N]-thymidine, a six-point external calibration curve of thymidine with standard range from 0.1 μg ml^{-1} to 10 μg ml^{-1} was constructed based on the peak area of this compound versus their concentration and it was used to calculate the thymidine concentration in DNA samples.

LC-MS/MS for peptide identification

In-gel trypsin digestion was performed on samples. Briefly, excised gel bands were de-stained twice in 100 mM ammonium bicarbonate/acetonitrile (50:50). The samples were then reduced (10 mM BME in 100 mM bicarbonate) and alkylated (55 mM iodoacetamide in 100 mM bicarbonate). After dehydration, trypsin (6 ng μl^{-1}) was added to just cover the gel pieces and the digestion was allowed to proceed overnight (~16 h) at room temperature. Tryptic peptides were first extracted from the gel using 97% water/2% acetonitrile/1% formic acid followed by a second extraction using 50% of the first extraction buffer and 50% acetonitrile. Fractions containing tryptic peptides were resolved and ionized by using nanoflow HPLC (Easy-nLC II, Thermo Fisher Scientific) coupled to an LTQ XL-Orbitrap hybrid mass spectrometer (Thermo Fisher Scientific). Nanoflow chromatography and electrospray ionization were accomplished by using a PicoFrit fused silica capillary column (ProteoPepII, C18) with 100 μm inner diameter (300 Å, 5 μm, New Objective). Peptide mixtures were injected into the column at a flow rate of 3,000 nL min^{-1} and resolved at 500 nL min^{-1} using linear gradients from 0 to 45% v/v aqueous ACN in 0.2% v/v formic acid over 45 min. The mass spectrometer was operated in data-dependent acquisition mode,

recording high-accuracy and high-resolution survey Orbitrap spectra using external mass calibration, with a resolution of 30,000 and m/z range of 400–2,000. The fourteen most intense multiply charged ions were sequentially fragmented by using collision-induced dissociation, and spectra of their fragments were recorded in the linear ion trap; after two fragmentations all precursors selected for dissociation were dynamically excluded for 60 s. Data was processed using Proteome Discoverer 1.4 (Thermo Fisher Scientific) and a reviewed UniProt (uniprot.org) human database was searched using SEQUEST (Thermo Fisher Scientific). Search parameters included a precursor mass tolerance of 10 ppm and a fragment mass tolerance of 0.8 Da.

DNA/RNA Isolation and quantitative real-time PCR (RT-qPCR)

DNA and RNA were isolated using the AllPrep DNA/RNA Mini Kit (Qiagen, Hilden, Germany). The TaqMan RNA-to-Ct 1-step kit (Applied Biosystems, CA, USA) was used as per manufacturer's instructions for quantification of RNA, using RT-qPCR and gene-specific (CRMP2A, Snail) primers (TaqMan Gene Expression Assays, Life Technologies). Assays were run on a QuantStudio™ 7 Flex Real-Time PCR System. Human 18S rRNA was used as a housekeeping gene. The exact sequences of the custom CRMP2A TaqMan assay are listed below.

Forward Primer: TGTTCTGCCCGGTGGAA

Reverse Primer: CCGACAGCGAGTCGAAGTC

Probe: TCCTCGGAGAACAAG

Mouse Xenograft, Lung Metastasis and allo-qRT-PCR

For s.c. tumor growth experiments, 8-week-old male athymic mice (Charles River, Wilmington, MA, USA) were subcutaneously injected with ~3 x 10^6 parental or CRMP2A-deficient A549 cells suspended in a 1:1 ratio of Matrigel (Corning, NY, USA) and PBS in the right flank after institutional ethics committee approval. For the tumorigenicity assay, 1 x 10^4 A549 cells were injected in the left (parental cells) and right (CRMP2A-deficient cells) flank of athymic mice. All tumors were measured twice per week using electronic calipers and allowed to grow to a maximum volume of 2,000 mm^3 or until animals lost 20% of their initial weight before harvesting. For lung metastasis, 5 x 10^5 parental or CRMP2A-deficient cells (resuspended in 0.1 ml PBS) were injected into the lateral tail vein of 7-8-week-old male athymic mice under aseptic conditions. Mice were weighed and monitored for mobility, respiratory distress and signs of pain weekly until sacrificed. Lung colonization was monitored and quantified using human-specific GAPDH primers and RT-qPCR (allo-RT-qPCR) on a Droplet Digital PCR QX200 system (Bio-Rad) according to the manufacturer's recommendations. 200 ng of RNA were used per reaction. Mouse β2M was used as a housekeeping gene. Each sample was partitioned into 20,000 discrete droplets and after amplification, each droplet was analyzed individually using a fluorescent detection system (FAM dye). Amplifications were carried out as follows: at 48 ˚C for 1 h, 95 ˚C for 10 min, followed by 40 cycles at 95 ˚C (30 s), 60 ˚C (1 min, ramp rate: 2 ˚C per second); followed by incubation at 98 ˚C (10 min) and holding at 4 ˚C.

FFPE Human Prostate Tissues

FFPE tissue blocks were obtained from the Alberta Prostate Cancer Research Institute (APCARI). 4x 10 μm thick slices from each tissue were used for RNA isolation, using the RNeasy FFPE kit (Qiagen) according to the manufacturer's recommendations. The amount of CRMP2A, Snail, GAPDH (housekeeping gene #1) and β2M (housekeeping gene #2) mRNA was quantified on a Droplet Digital PCR QX200 system (Bio-Rad). 100 ng of RNA were used per reaction. Each sample was partitioned into 20,000 discrete droplets and after amplification, each droplet was analyzed individually using a fluorescent detection system (FAM dye). Amplifications were carried out as follows: at 48 ˚C for 1 h, 95 ˚C for 10 min, followed by 40 cycles at 95 ˚C (30 s), 60 ˚C (1 min, ramp rate: 2 ˚C per second); followed by incubation at 98 ˚C (10 min) and holding at 4 ˚C.

Statistical analysis

All statistical analyses were performed on GraphPad Prism (GraphPad software, CA, USA). Values are expressed as mean ± SEM. Comparisons between two groups were made using the Mann-Whitney U test. Kruskal-Wallis test was used to compare inter-group differences between three or more groups. The Wilcoxon signed-rank test was used to compare matched samples (prostate cancer patients). Spearman's correlation was performed to measure the association between two interval variables. Significance was considered at $p < 0.05$.

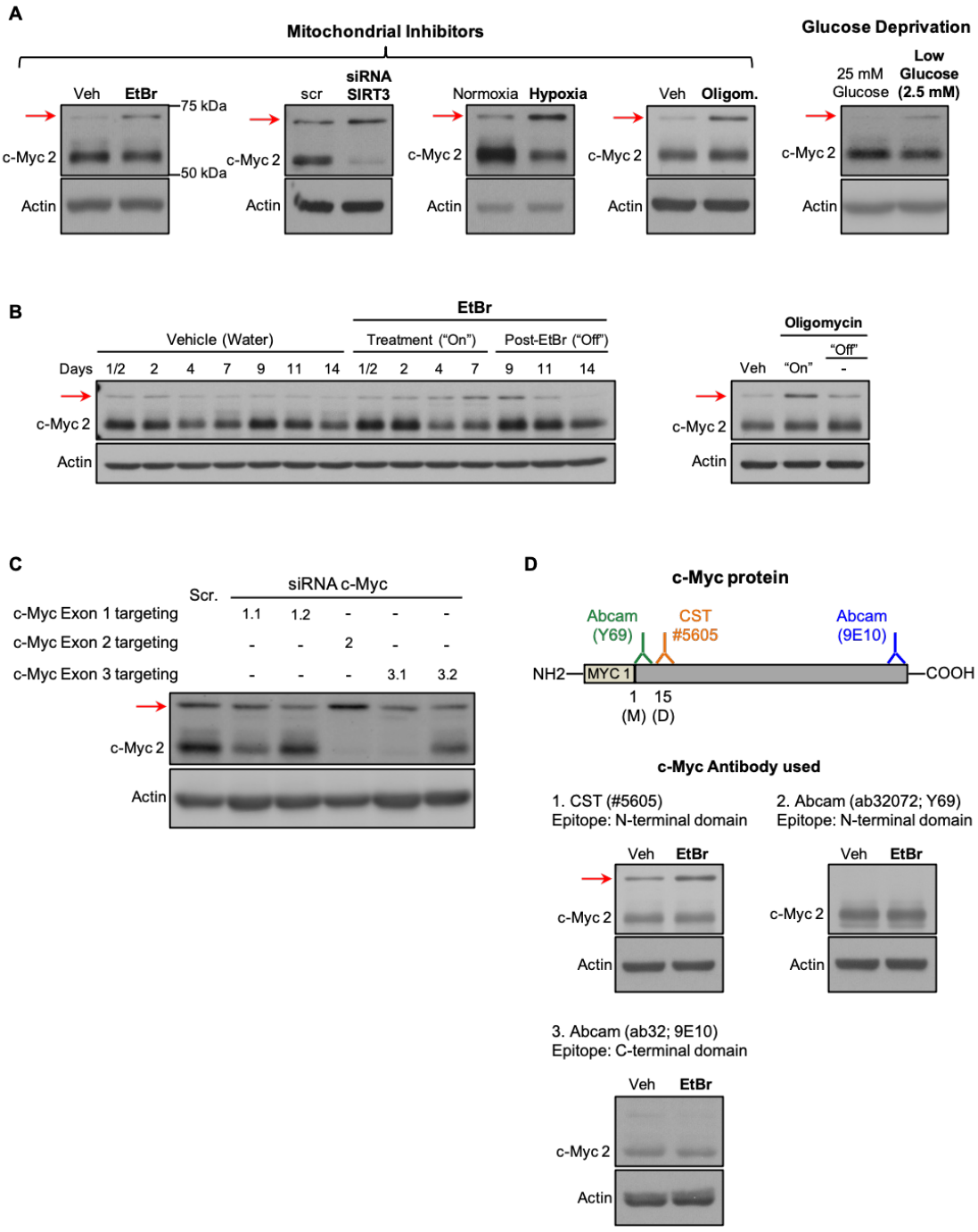
A
Mitochondrial Inhibitors
Glucose Deprivation
Veh
EtBr
75 kDa
50 kDa
c-Myc 2
Actin
scr
siRNA SIRT3
Normoxia
Hypoxia
Veh
Oligom.
25 mM Glucose
Low Glucose (2.5 mM)
B
EtBr
Vehicle (Water)
Treatment ("On")
Post-EtBr ("Off")
Days 1/2 2 4 7 9 11 14 1/2 2 4 7 9 11 14
Oligomycin
Veh
"On"
"Off"
C
Scr.
siRNA c-Myc
c-Myc Exon 1 targeting
c-Myc Exon 2 targeting
c-Myc Exon 3 targeting
1.1 1.2 - - -
- - 2 - -
- - - 3.1 3.2
D
c-Myc protein
Abcam (Y69)
CST #5605
Abcam (9E10)
NH2
MYC 1
COOH
1 15
(M) (D)
c-Myc Antibody used
1. CST (#5605)
Epitope: N-terminal domain
2. Abcam (ab32072; Y69)
Epitope: N-terminal domain
3. Abcam (ab32; 9E10)
Epitope: C-terminal domain

Figure 2-1: A c-Myc antibody-reactive band is reversibly induced in A549 cells following exposure to diverse metabolic stressors.

(A) A549 cells (NSCLC) exposed to diverse metabolic stresses show increased levels of a c-Myc antibody-reactive band at around 72 kDa (red arrows) by immunoblot. The anti-c-Myc #5605 antibody from Cell Signaling Technology (CST) was used for all blots. The positions of molecular weight markers (50 and 75 kDa) relative to this band are indicated on the right. Actin was used as a loading control. **(B)** Induction of the unknown protein (red arrows) is reversible upon removal of the mitochondrial stress (EtBr, Oligomycin). EtBr and Oligomycin were removed from the culture medium after 7 and 2 days of continuous treatment respectively. Actin was used as a loading control. **(C)** Transfection with 5 different c-Myc siRNAs, each targeting a different exon, does not affect the levels of the unknown protein (red arrows) to the levels expected if this protein represented a novel c-Myc isoform, as it does with c-Myc 2 expression. Actin was used as a loading control. Scr.: Scramble. **(D)** Two different commercially available c-Myc antibodies raised against the N- (Abcam, Y69) and C-terminus (Abcam, 9E10) of the human c-Myc protein fail to recognize the unknown protein, compared to the CST #5605 antibody (red arrow), in lysates from Vehicle (Veh)- and EtBr-treated A549 cells, while they effectively detect c-Myc 2. Schematic (top) shows the approximate binding site of these antibodies on the c-Myc protein. Amino acids at positions 1 (M; Methionine) and 15 (D; Aspartic acid) are also shown to signify the relative binding sites of these antibodies on the c-Myc protein. Actin was used as a loading control.

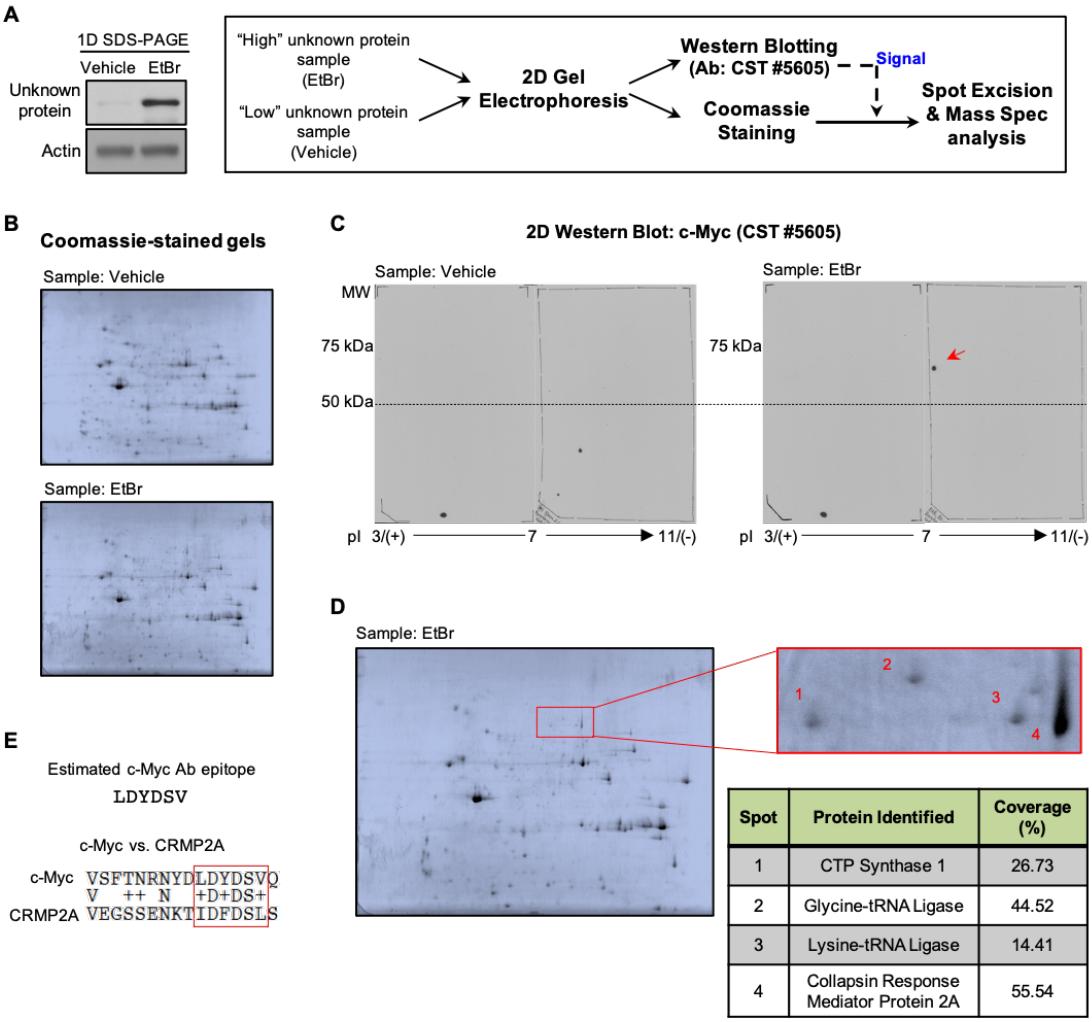

Spot	Protein Identified	Coverage (%)
1	CTP Synthase 1	26.73
2	Glycine-tRNA Ligase	44.52
3	Lysine-tRNA Ligase	14.41
4	Collapsin Response Mediator Protein 2A	55.54

Figure 2-2: An unbiased 2D gel- and Mass Spec-based proteomic approach identifies the metabolic stress-responsive unknown protein as the Collapsin Response Mediator Protein 2A (CRMP2A).

(A) Schematic depicting our strategy to identify the unknown protein from a "high" (EtBr) and a "low" (Vehicle) expression sample. Relative expression of the protein is shown in the 1D electrophoresis blot (left). Actin was used as a loading control. **(B)** Coomassie staining of proteins in gels post-2D electrophoresis. **(C)** The c-Myc CST #5605 antibody, which reacts with the unknown protein, produces a single Western blot signal (red arrow) in the "high" sample but not in the "low" sample. X-axis: Isoelectric Point (pI), Y-Axis: Molecular Weight (MW). **(D)** Selection of protein spots for Mass Spec analysis. The area of interest was defined by overlapping the Western blot signal to the Coomassie-stained gel of the "high" sample. Table shows the returned hits with their sequence coverage. **(E)** The predicted epitope of the reactive c-Myc antibody (CST #5605) bears similarity with an N-terminal stretch of 6 amino acids within the CRMP2A protein, suggesting cross-reactivity with CRMP2A is highly possible.

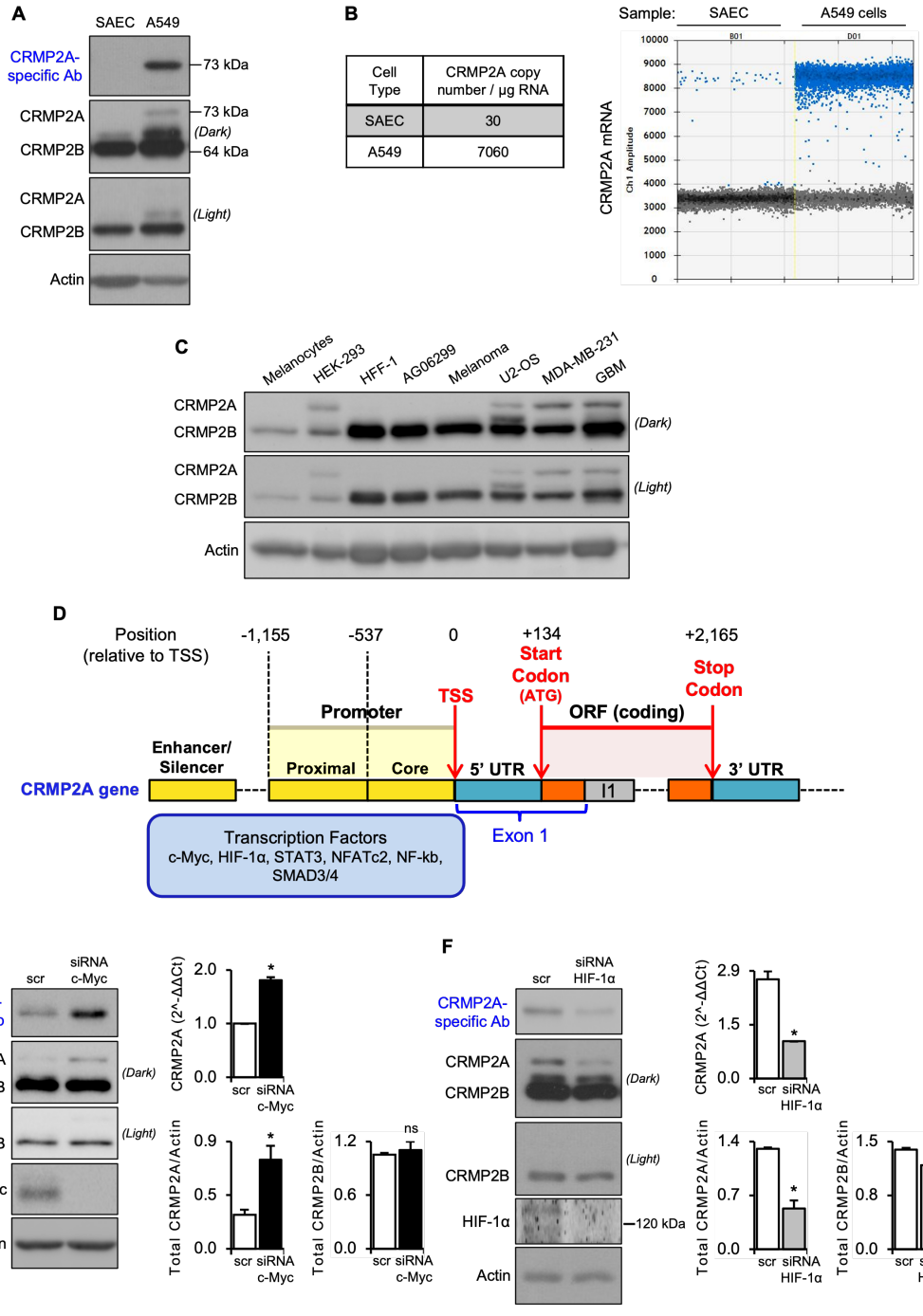
A
SAEC A549
CRMP2A-specific Ab
73 kDa
CRMP2A
CRMP2B
73 kDa
(Dark)
64 kDa
CRMP2A
CRMP2B
(Light)
Actin
B
Cell Type
CRMP2A copy number / µg RNA
SAEC
30
A549
7060
Sample: SAEC A549 cells
CRMP2A mRNA
Ch1 Amplitude
C
Melanocytes
HEK-293
HFF-1
AG06299
Melanoma
U2-OS
MDA-MB-231
GBM
CRMP2A
CRMP2B
(Dark)
CRMP2A
CRMP2B
(Light)
Actin
D
Position (relative to TSS)
-1,155
-537
0
+134
+2,165
Start Codon (ATG)
Stop Codon
TSS
Promoter
ORF (coding)
Enhancer/ Silencer
Proximal
Core
5' UTR
I1
3' UTR
CRMP2A gene
Exon 1
Transcription Factors
c-Myc, HIF-1α, STAT3, NFATc2, NF-kb, SMAD3/4
E
scr
siRNA c-Myc
CRMP2A-specific Ab
CRMP2A
CRMP2B
(Dark)
CRMP2B
(Light)
c-Myc
Actin
CRMP2A (2^-ΔΔCt)
Total CRMP2A/Actin
Total CRMP2B/Actin
ns
F
scr
siRNA HIF-1α
CRMP2A-specific Ab
CRMP2A
CRMP2B
(Dark)
CRMP2B
(Light)
HIF-1α
120 kDa
Actin
CRMP2A (2^-ΔΔCt)
Total CRMP2A/Actin
Total CRMP2B/Actin

Figure 2-3: CRMP2A is more highly expressed in cancer vs. normal cells and its transcription is antagonistically regulated by c-Myc and HIF-1α.

(A) Immunoblots of total CRMP2A and CRMP2B proteins in small airway epithelial cells (SAEC) vs. A549 cells show significantly higher CRMP2A levels in A549 cells. Both a CRMP2A-specific as well as a CRMP2A/B-reactive antibody were used. Dark and light exposures are shown to address confounding saturation effects in CRMP2A and CRMP2B. Actin was used as a loading control. Experiment was performed once. **(B)** A549 cells have much higher CRMP2A mRNA levels compared to SAEC, using a droplet digital PCR (ddPCR) system. Results are expressed as mRNA copies per μg of RNA. The graph on the right depicts the number of positive droplets (blue spots) above the baseline for both cell types. Experiment was performed once. **(C)** Immunoblots show higher expression of the CRMP2A (but not CRMP2B) protein in a panel of cancer vs. normal cell lines (HEK-293: Human Embryonic Kidney cells, HFF-1: Foreskin Fibroblasts, AG06299: Skin Fibroblasts, U2-OS: Osteosarcoma, GBM: Glioblastoma). GBM is a patient-derived primary cell line that was generated from a tumor obtained from a patient for one of our previous studies[32]. All other cell lines are commercially available. Dark and light exposures are shown to address confounding saturation effects in CRMP2A and CRMP2B. Actin was used as a loading control. Experiment was performed once. **(D)** Schematic showing the structure of the CRMP2A gene upstream (enhancer/silencer and promoter regions) and downstream (untranslated regions, open reading frame) of the consensus transcription start site (TSS; position 0). The most important putative transcription factors, based on *in silico* analysis of predicted binding sites (searched for on the enhancer/silencer and promoter regions), are also listed below. **(E)** Reduction in c-

Myc levels using siRNA increases the CRMP2A (but not CRMP2B) mRNA and protein levels, using qRT-PCR and immunoblots. Dark and light exposures are shown to address confounding saturation effects in CRMP2A and CRMP2B. 18S and actin were used as loading controls respectively (means and SEM are shown for the CRMP2A mRNA and the CRMP2A and CRMP2B protein levels, n = 3-4; *$p<0.05$ compared to scramble, two-tailed Mann-Whitney U test. Please note that if the SEM is too low, it may not show in lower magnifications of the figure). **(F)** Reduction in HIF-1α levels using siRNA decreases the CRMP2A (but not CRMP2B) mRNA and protein levels, using qRT-PCR and immunoblots. Dark and light exposures are shown to address confounding saturation effects in CRMP2A and CRMP2B. 18S and actin were used as loading controls respectively (means and SEM are shown for the CRMP2A mRNA and the CRMP2A and CRMP2B protein levels, n = 4; *$p<0.05$ compared to scramble, two-tailed Mann-Whitney U test. Please note that if the SEM is too low, it may not show in lower magnifications of the figure). HIF-1α knockdown was associated with a strong decrease in HIF-1α target genes (e.g. PDK1 mRNA) (data not shown).

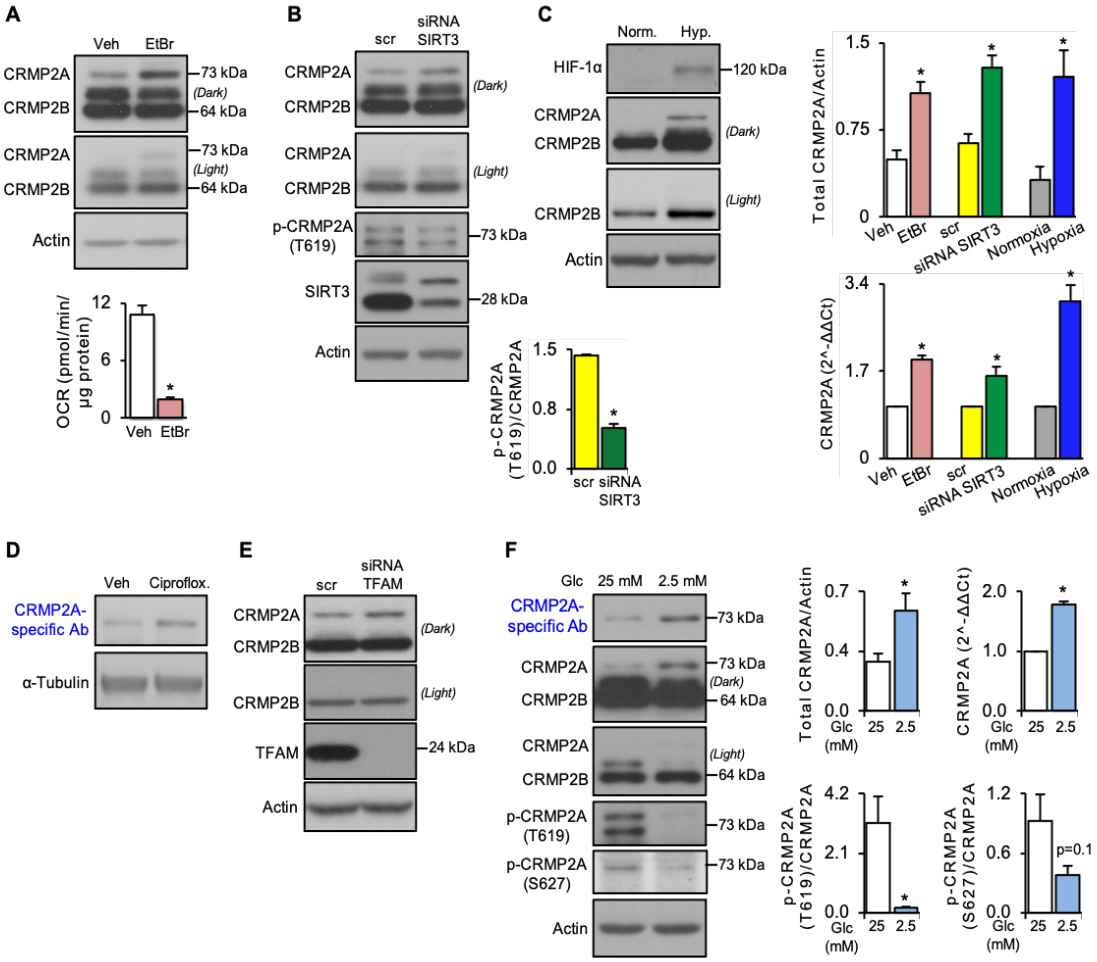
A
Veh
EtBr
CRMP2A
CRMP2B
73 kDa
(Dark)
64 kDa
73 kDa
(Light)
64 kDa
Actin
OCR (pmol/min/ µg protein)
12
6
0
Veh
EtBr
B
scr
siRNA SIRT3
CRMP2A
CRMP2B
(Dark)
(Light)
p-CRMP2A (T619)
73 kDa
SIRT3
28 kDa
Actin
p-CRMP2A (T619)/CRMP2A
1.5
0.8
0.0
scr
siRNA SIRT3
C
Norm.
Hyp.
HIF-1α
120 kDa
CRMP2A
CRMP2B
(Dark)
(Light)
Actin
Total CRMP2A/Actin
1.5
0.75
0
Veh
EtBr
scr
siRNA SIRT3
Normoxia
Hypoxia
CRMP2A (2^-ΔΔCt)
3.4
1.7
0
D
Veh
Ciproflox.
CRMP2A-specific Ab
α-Tubulin
E
scr
siRNA TFAM
CRMP2A
CRMP2B
(Dark)
(Light)
TFAM
24 kDa
Actin
F
Glc
25 mM
2.5 mM
CRMP2A-specific Ab
73 kDa
CRMP2A
CRMP2B
73 kDa
(Dark)
64 kDa
CRMP2A
CRMP2B
(Light)
64 kDa
p-CRMP2A (T619)
73 kDa
p-CRMP2A (S627)
73 kDa
Actin
Total CRMP2A/Actin
0.7
0.4
0.0
Glc (mM)
25
2.5
CRMP2A (2^-ΔΔCt)
2.0
1.0
0.0
p-CRMP2A (T619)/CRMP2A
4.2
2.1
0.0
p-CRMP2A (S627)/CRMP2A
1.2
0.6
0.0
p=0.1

Figure 2-4: The unphosphorylated form of CRMP2A is transcriptionally induced in A549 cells exposed to metabolic stress.

(A-F) Immunoblot analysis of the total and phosphorylated (Ser, Thr sites) CRMP2A shows an induction of the unphosphorylated CRMP2A protein in A549 cells exposed to different mitochondrial inhibitors (EtBr, SIRT3 siRNA, Ciprofloxacin, TFAM siRNA) as well as hypoxia (**A-E**) or low glucose (Glc) (**F**). Dark and light exposures are shown to address confounding saturation effects in CRMP2A and CRMP2B. Actin or α-Tubulin (**D**) were used as loading controls (means and SEM are shown for the total CRMP2A and the ratio of phosphorylated CRMP2A (both Ser and Thr sites) over total CRMP2A protein, n = 3-6; *$p<0.05$ compared to control conditions, two-tailed Mann-Whitney U test). Please note that n=1 for the Ciprofloxacin treatment and n=2 for the siRNA TFAM experiment. CRMP2A mRNA levels also increase under the same conditions using qRT-PCR. 18S was used as a housekeeping gene (n = 3-4; *$p<0.05$ compared to control conditions, two-tailed Mann-Whitney U test. Please note that if the SEM is too low, it may not show in lower magnifications of the figure).

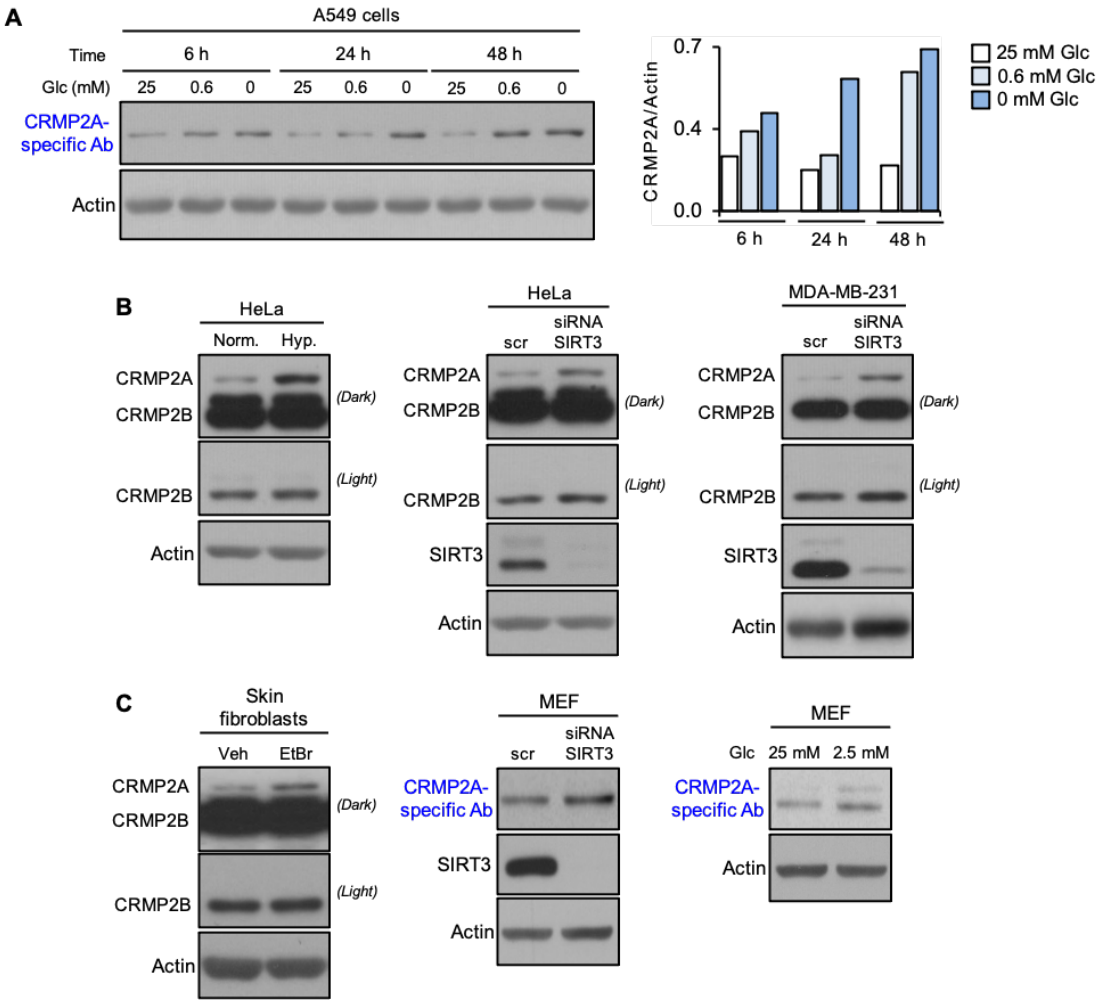
A
A549 cells
Time
6 h
24 h
48 h
Glc (mM)
25 0.6 0 25 0.6 0 25 0.6 0
CRMP2A-specific Ab
Actin
CRMP2A/Actin
0.7
0.4
0.0
6 h
24 h
48 h
25 mM Glc
0.6 mM Glc
0 mM Glc
B
HeLa
Norm. Hyp.
CRMP2A
CRMP2B
(Dark)
CRMP2B
(Light)
Actin
HeLa
scr siRNA SIRT3
CRMP2A
CRMP2B
(Dark)
CRMP2B
(Light)
SIRT3
Actin
MDA-MB-231
scr siRNA SIRT3
CRMP2A
CRMP2B
(Dark)
CRMP2B
(Light)
SIRT3
Actin
C
Skin fibroblasts
Veh EtBr
CRMP2A
CRMP2B
(Dark)
CRMP2B
(Light)
Actin
MEF
scr siRNA SIRT3
CRMP2A-specific Ab
SIRT3
Actin
MEF
Glc 25 mM 2.5 mM
CRMP2A-specific Ab
Actin

Figure 2-5: Increase in CRMP2A but not CRMP2B protein levels in response to metabolic stress is observed in other cancer as well as normal cell lines.

(A) In a combined dose-response and time-course exploratory experiment, CRMP2A protein levels show evidence of increase as early as 6 h. At the same time there was evidence of increasing expression at all timepoints (6, 24 and 48 h) as glucose (Glc) concentration in the medium decreased from 25 mM (baseline) to 0.6 mM, to almost 0 mM (achieved by using dialyzed serum, which removes glucose). While this particular experimental setup was only used once, similar exploratory experiments to identify the concentration of glucose and effective duration of glucose starvation yielded similar results. Therefore, we subsequently focused on 24 or 48 h in order to allow any downstream effects of CRMP2A induction to be evident, and on 2.5 mM glucose concentration since this is more physiologic, i.e. closer to what tumor cells may be exposed to *in vivo*. **(B)** CRMP2A protein increases in HeLa (cervix) and MDA-MB-231 (breast) cancer cells exposed to metabolic stress (hypoxia, SIRT3 siRNA), as assessed by immunoblots. Dark and light exposures are shown to address confounding saturation effects in CRMP2A and CRMP2B. Actin was used as a loading control. $n = 2$ for HeLa (normoxia vs. hypoxia), $n = 1$ for HeLa (scramble vs. siRNA SIRT3), $n = 2$ for MDA-MB-231 (scramble vs. siRNA SIRT3). **(C)** CRMP2A protein increases in proliferative normal cells that are also known to undergo EMT (human skin fibroblasts and mouse embryonic fibroblasts, MEF) exposed to metabolic stress (EtBr, SIRT3 siRNA, low glucose), as assessed by immunoblots. Dark and light exposures are shown to address confounding saturation effects in CRMP2A and CRMP2B. Actin was used as a loading control. $n = 2$ for skin

fibroblasts (Vehicle vs. EtBr), $n = 2$ for MEF (scramble vs. siRNA SIRT3), $n = 1$ for MEF (25mM Glucose vs. 2.5mM Glucose).

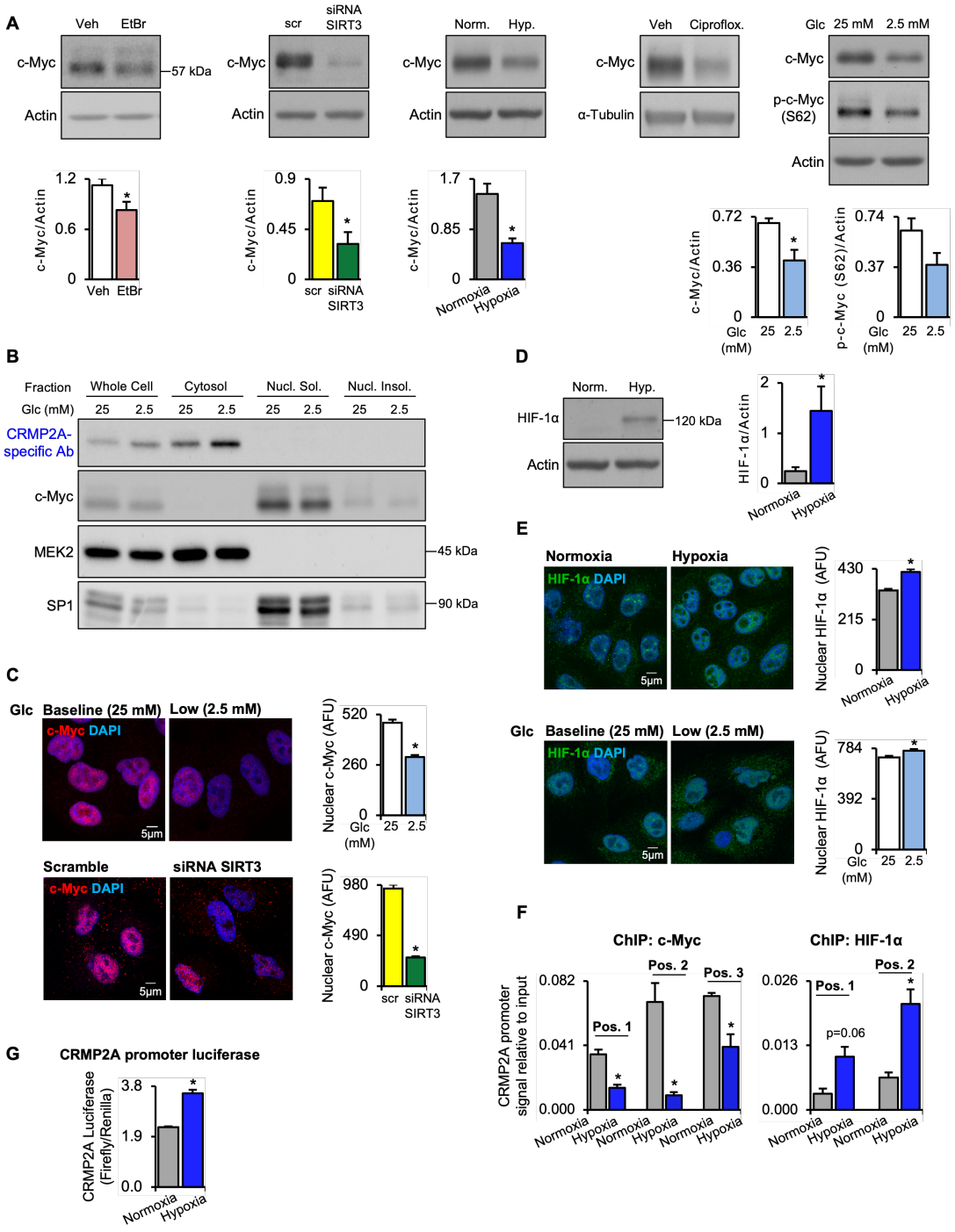
A
Veh
EtBr
c-Myc
Actin
57 kDa
scr
siRNA SIRT3
Norm.
Hyp.
Veh
Ciproflox.
α-Tubulin
Glc 25 mM 2.5 mM
p-c-Myc (S62)
c-Myc/Actin
p-c-Myc (S62)/Actin
Normoxia
Hypoxia
B
Fraction
Whole Cell
Cytosol
Nucl. Sol.
Nucl. Insol.
Glc (mM)
CRMP2A-specific Ab
MEK2
SP1
45 kDa
90 kDa
C
Glc
Baseline (25 mM)
Low (2.5 mM)
c-Myc DAPI
5μm
Nuclear c-Myc (AFU)
Scramble
siRNA SIRT3
D
HIF-1α
120 kDa
HIF-1α/Actin
E
Normoxia
Hypoxia
HIF-1α DAPI
Nuclear HIF-1α (AFU)
F
ChIP: c-Myc
ChIP: HIF-1α
CRMP2A promoter signal relative to input
Pos. 1
Pos. 2
Pos. 3
p=0.06
G
CRMP2A promoter luciferase
CRMP2A Luciferase (Firefly/Renilla)

Figure 2-6: Differential activity of c-Myc and HIF-1α controls the transcriptional induction of CRMP2A under metabolic stress.

(A) Immunoblots show increased whole-cell levels of c-Myc and p-c-Myc (Ser62) in A549 cells exposed to several different types of metabolic stress (means and SEM are shown for the total and (Ser62)-phosphorylated c-Myc levels, n = 3-4; *p<0.05 compared to control conditions, two-tailed Mann-Whitney U test. Please note that the Ciprofloxacin treatment was only performed once as a proof of concept of c-Myc reduction for antibiotic-induced mitochondrial stress). **(B)** Subcellular fractionation of A549 cells at baseline (25 mM) and low glucose (Glc) (2.5 mM, 48 h) conditions shows increased CRMP2A levels in the cytoplasm when nuclear c-Myc levels decrease during exposure to low glucose. Whole cell lysates are also included in the immunoblot. MEK2 and SP1 proteins were used as markers of purity for the cytoplasmic and soluble nuclear compartments respectively. Note that CRMP2A is not present in the nuclear (soluble and insoluble) fractions. This experiment was performed once. **(C)** Immunofluorescence analysis shows decreased nuclear c-Myc levels in A549 cells after exposure to low Glucose (Glc) (2.5 mM) or treatment with a SIRT3 siRNA (c-Myc: red, DAPI nuclear stain: blue; means and SEM are shown, n = 200-250 cells per group from 6-9 random fields per slide for the low Glucose treatment, n ~ 400 cells per group from 16 random fields per slide for the SIRT3 siRNA treatment; *p<0.05 compared to 25 mM Glucose or scramble respectively, two-tailed Mann-Whitney U test). **(D)** Exposure of A549 cells to hypoxia increases the whole-cell levels of HIF-1α (mean and SEM are shown for the HIF-1α levels, n = 4; *p<0.05 compared to control conditions, two-tailed Mann-Whitney U test). **(E)** Immunofluorescence analysis shows increased nuclear HIF-1α levels in A549 cells

after exposure to hypoxia or low glucose (Glc) (2.5mM) (HIF-1α: green, DAPI nuclear stain: blue; means and SEM are shown, n ~ 100-150 cells per group; at least 3 random fields were analyzed per slide; *$p<0.05$ compared to control conditions, two-tailed Mann-Whitney U test).

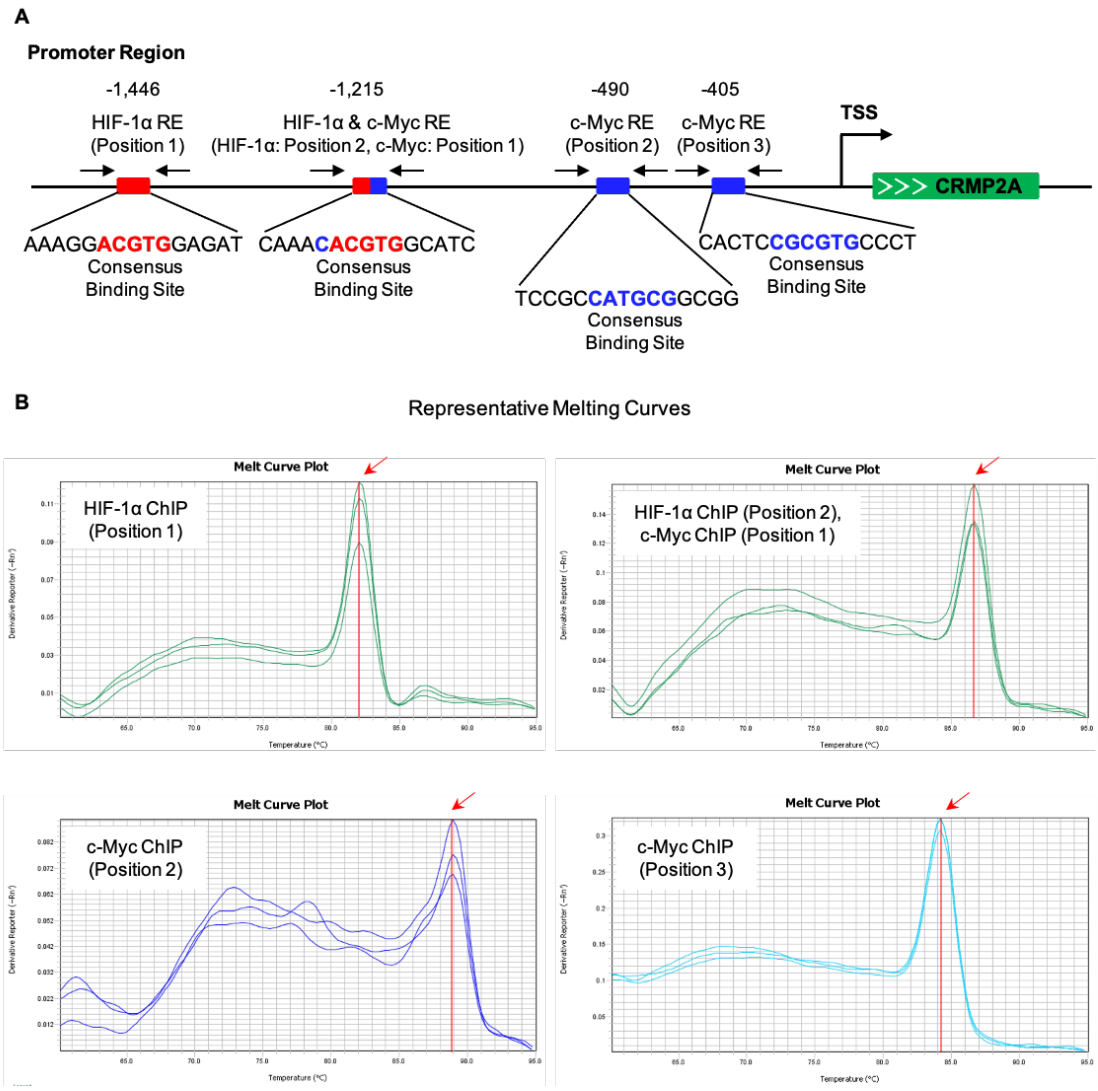

Figure 2-7: Schematic representation of the custom CRMP2A ChIP assay.

(A) The position of two putative HIF-1α (red boxes) and three c-Myc (blue boxes) response elements (RE) is shown on the CRMP2A promoter region. TSS is defined as position 0. Arrows indicate the position of the primers used for each qRT-PCR relative to the HIF-1α/c-Myc binding sites. **(B)** Representative profiles of the melting curves for each qRT-PCR product show lack of non-specific amplification. The largest peak in each image (red arrows) represents the main source of the fluorescence generated during qRT-PCR. Smaller humps to the left of the main peaks represent primer dimers.

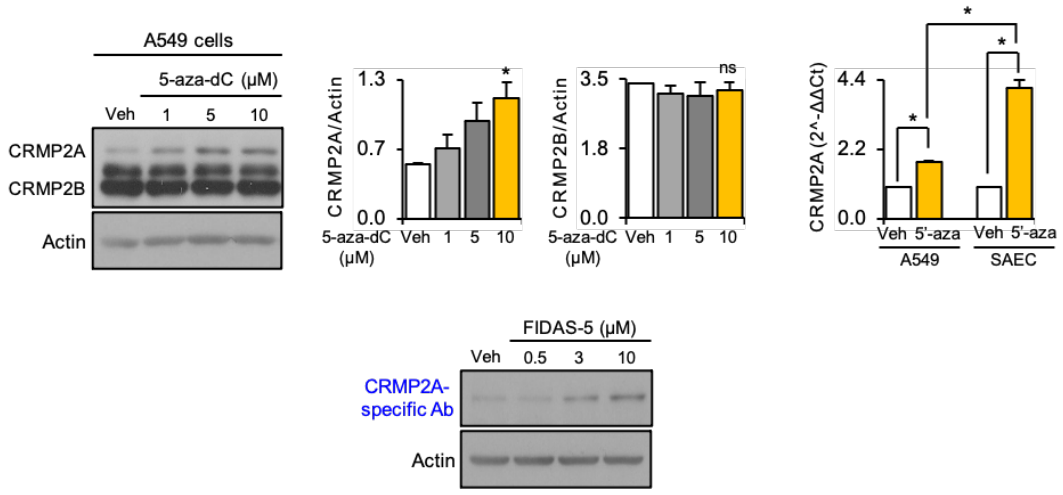

Figure 2-8: Methylation of the CRMP2A promoter is operational in normal and cancer cells.

Immunoblots show a dose-dependent increase in CRMP2A protein levels in A549 cells by the DNA methyltransferase inhibitor 5-aza-dC (72 h) and the S-adenosyltransferase 2A inhibitor FIDAS-5 (48 h). By contrast, 5-aza-dC treatment does not affect CRMP2B levels. Actin was used as a loading control (n = 3 for the 5-aza-dC treatment; *p<0.05 compared to Vehicle, Kruskal-Wallis test followed by one-tailed Mann-Whitney U test. The FIDAS-5 treatment was performed once as another way of reducing the amount of available methylation groups for DNA methylation). Treatment with a high 5-aza-dC dose (10 μM) increases the CRMP2A mRNA levels by 2-fold in A549 cells and by 4-fold in SAEC, using qRT-PCR. 18S was used as a housekeeping gene (n = 3, CRMP2A mRNA expression under Vehicle treatment was independently set to 1 for each cell line to allow direct comparison of the fold changes between the two cell lines; *p<0.05 compared to Vehicle, Kruskal-Wallis test followed by one-tailed Mann-Whitney U test. Please note that if the SEM is too low, it may not show in lower magnifications of the figure).

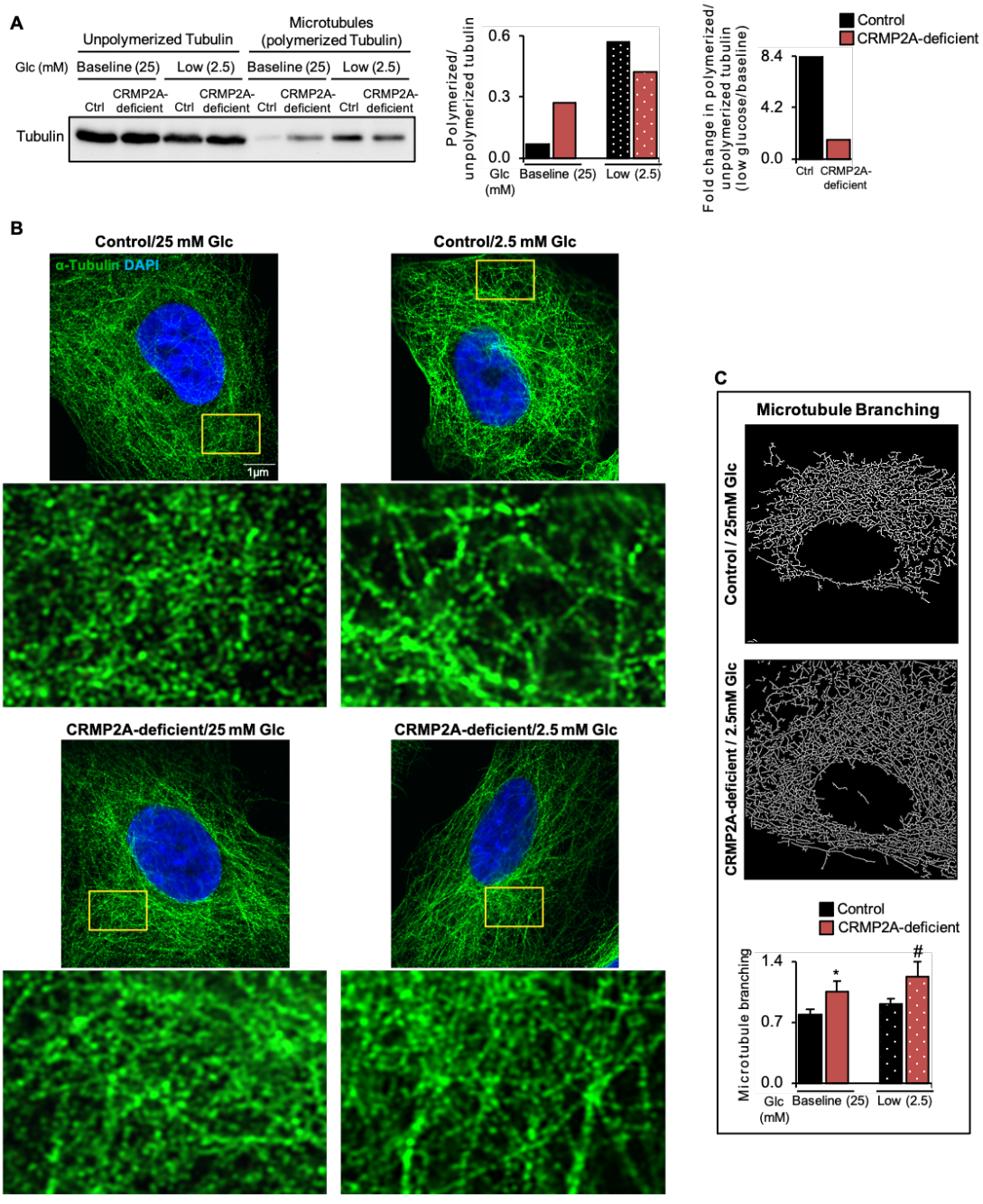
A
Unpolymerized Tubulin
Microtubules (polymerized Tubulin)
Glc (mM)
Baseline (25)
Low (2.5)
Baseline (25)
Low (2.5)
Ctrl
CRMP2A-deficient
Ctrl
CRMP2A-deficient
Ctrl
CRMP2A-deficient
Ctrl
CRMP2A-deficient
Tubulin
Polymerized/unpolymerized tubulin
0.6
0.3
0.0
Glc (mM)
Baseline (25)
Low (2.5)
Fold change in polymerized/unpolymerized tubulin (low glucose/baseline)
Control
CRMP2A-deficient
8.4
4.2
0.0
Ctrl
CRMP2A-deficient
B
Control/25 mM Glc
α-Tubulin DAPI
1μm
Control/2.5 mM Glc
CRMP2A-deficient/25 mM Glc
CRMP2A-deficient/2.5 mM Glc
C
Microtubule Branching
Control / 25mM Glc
CRMP2A-deficient / 2.5mM Glc
Control
CRMP2A-deficient
Microtubule branching
1.4
0.7
0.0
*
#
Glc (mM)
Baseline (25)
Low (2.5)

Figure 2-9: Reduction of CRMP2A promotes tubulin polymerization and microtubule branching.

(A) CRMP2A-deficient A549 cells have increased polymerized tubulin, compared to control (ctrl) cells at baseline. Exposure to low glucose (Glc) increases the amount of polymerized tubulin (microtubules) in control, but not in CRMP2A-deficient cells, as assessed by a microtubule/tubulin assay. Free (unpolymerized) tubulin and microtubule fractions were separated through an ultracentrifugation step, which precipitates microtubules only. Graphs show the ratio of polymerized over unpolymerized tubulin for each condition (left) and the fold change in polymerized over unpolymerized tubulin between baseline and low glucose conditions for each cell line (right). Experiment was performed once as a confirmatory technique, along with our immunofluorescence experiments, our main technique to identify the effects of CRMP2A loss on tubulin polymerization. **(B)** Immunofluorescence analysis of α-Tubulin in control A549 cells shows increased microtubule branching in response to metabolic stress (low glucose). This is not observed in CRMP2A-deficient cells, which had increased branching compared to control cells at both baseline and low glucose conditions (α-Tubulin: green, DAPI nuclear stain: blue). Bottom images in each group are high magnifications of representative areas (yellow boxes) from the images above. **(C)** Microtubule skeleton images generated via an ImageJ plugin (LPIXEL) based on tubulin staining and confocal imaging photomicrographs, were used to quantify the branching points of microtubules, showing increased branching in CRMP2A-deficient cells (n = 6 fields/group/plate, *$p<0.05$ compared to control cells-baseline; #$p<0.05$ compared to control-low glucose).

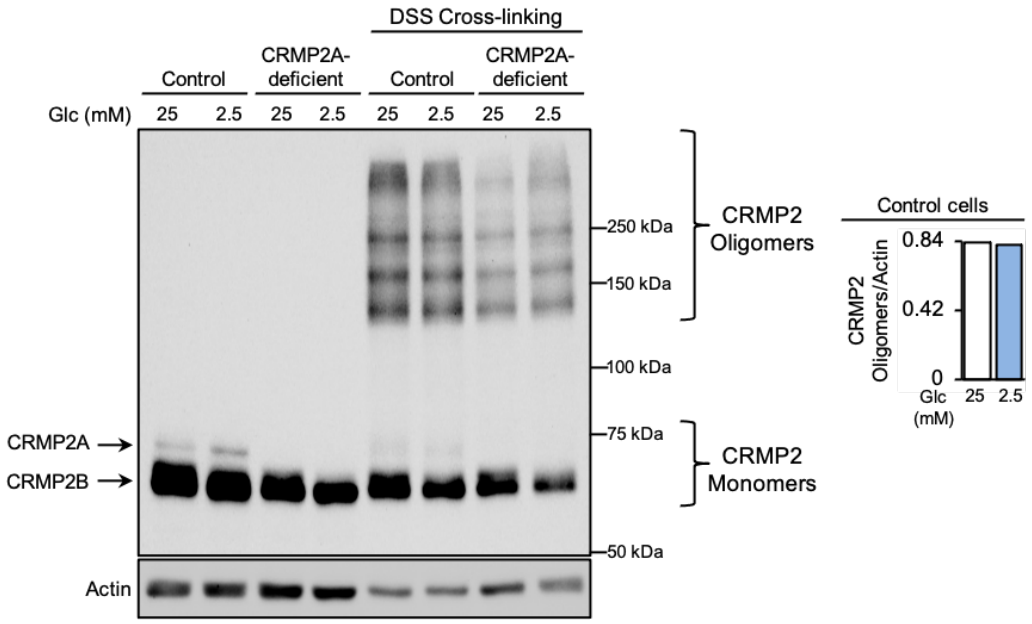

Figure 2-10: Induction of CRMP2A under metabolic stress does not affect the formation of CRMP2 oligomers.

Irreversible protein cross-linking with disuccinimidyl suberate (DSS) shows no significant difference in the amount of CRMP2 dimers and tetramers upon induction of CRMP2A under low glucose (Glc) conditions, using immunoblots. Actin was used as a loading control. The normalized levels of CRMP2 oligomers (dimers and tetramers) at baseline and low glucose conditions are shown for the control cells only. Experiment was performed once for the purpose of excluding changes in the amount CRMP2 oligomers upon glucose starvation.

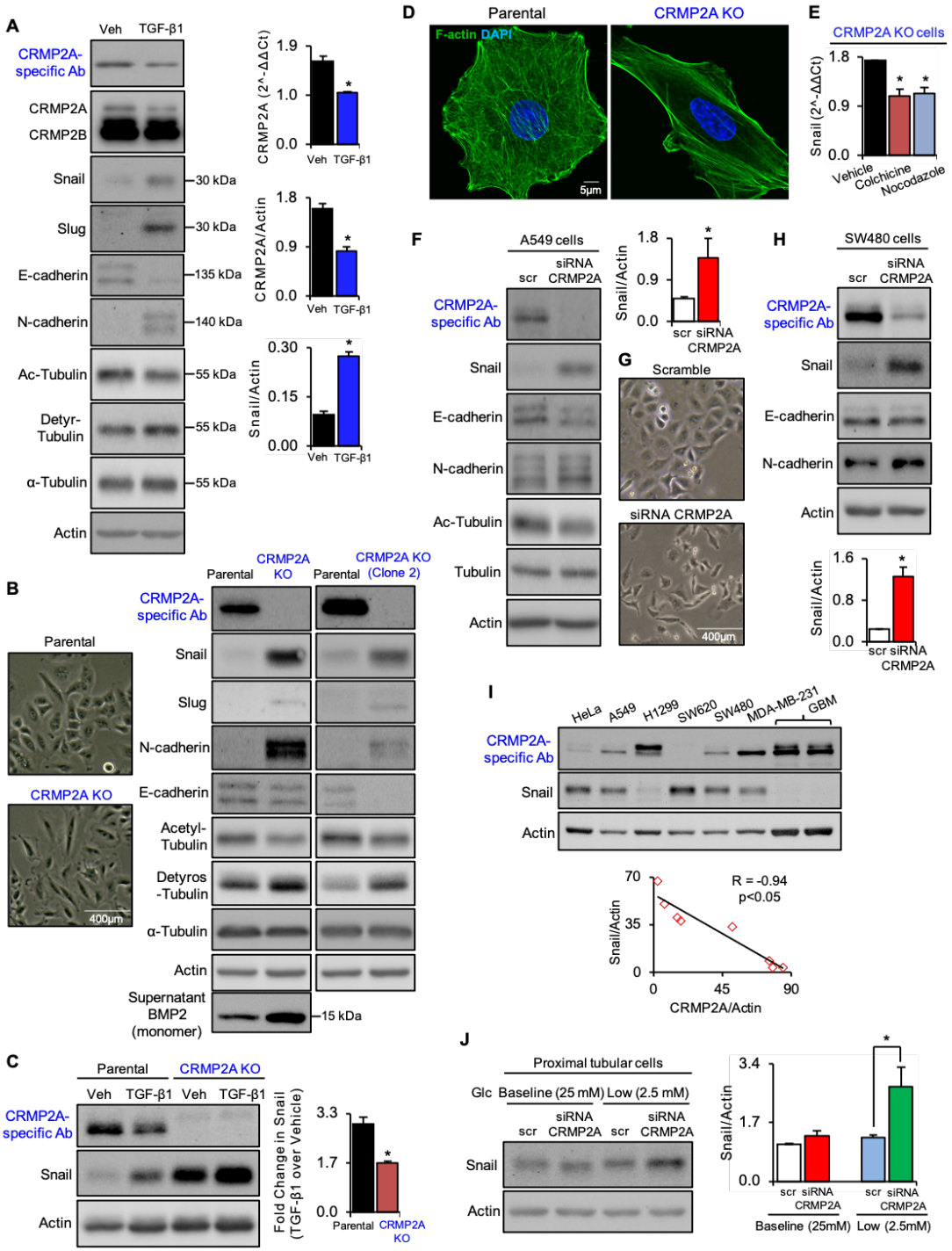
A
Veh
TGF-β1
CRMP2A-specific Ab
CRMP2A
CRMP2B
Snail
Slug
E-cadherin
N-cadherin
Ac-Tubulin
Detyr-Tubulin
α-Tubulin
Actin
30 kDa
30 kDa
135 kDa
140 kDa
55 kDa
55 kDa
55 kDa
CRMP2A (2^-ΔΔCt)
CRMP2A/Actin
Snail/Actin
B
Parental
CRMP2A KO
CRMP2A KO (Clone 2)
400μm
Acetyl-Tubulin
Detyros-Tubulin
Supernatant BMP2 (monomer)
15 kDa
C
Fold Change in Snail (TGF-β1 over Vehicle)
D
F-actin DAPI
5μm
E
CRMP2A KO cells
Snail (2^-ΔΔCt)
Vehicle
Colchicine
Nocodazole
F
A549 cells
siRNA
scr
CRMP2A
Snail/Actin
G
Scramble
siRNA CRMP2A
H
SW480 cells
I
HeLa
A549
H1299
SW620
SW480
MDA-MB-231
GBM
R = -0.94
p<0.05
CRMP2A/Actin
J
Proximal tubular cells
Glc
Baseline (25 mM)
Low (2.5 mM)
Baseline (25mM)
Low (2.5mM)

Figure 2-11: Loss of CRMP2A induces an EMT phenotype with extensive cytoskeletal reorganization.

(A) Treatment of A549 cells with rhTGF-β1 (48 h) induces several EMT-related molecular alterations, while also decreasing the CRMP2A mRNA and protein levels. The decrease in CRMP2A is associated with an increase in Snail, Slug, N-cadherin and a decrease in E-cadherin. The decrease in acetylated tubulin (Ac-tubulin) and increase in detyrosinated tubulin (Detyr-tubulin) are also compatible with induction of EMT. 18S and actin were used as loading controls respectively (means and SEM are shown for the CRMP2A mRNA as well as the CRMP2A and Snail protein levels, $n = 4$; *$p<0.05$ compared to Vehicle, two-tailed Mann-Whitney U test). **(B)** Two CRMP2A-deficient clones of A549 cells generated using the CRISPR/Cas9 system display several morphological and molecular features of EMT. Parental cells lost their cobblestone morphology and became elongated, spindle-shaped. CRMP2A-deficient cells show increased expression of Snail, Slug, N-cadherin, Detyr-tubulin as well as decreased expression of E-cadherin and Ac-tubulin. An immunoblot was also performed in the supernatant of cells, showing marked increase in secreted BMP2, also compatible with EMT phenotype. Actin was used as a loading control. **(C)** rhTGF-β1-mediated Snail induction is lower in CRMP2A-deficient cells compared to parental cells. Actin was used as a loading control (means and SEM are shown for the fold change in Snail post-rhTGF-β1 treatment, $n = 4$; *$p<0.05$ compared to parental cells, two-tailed Mann-Whitney U test). **(D)** CRMP2A-deficient cells show reorganization of F-actin filaments into thick, contractile bundles compared to the thin, cortical filaments of parental cells, using confocal microscopy (F-actin: green, DAPI nuclear stain: blue). **(E)** Treatment of CRMP2A-deficient A549 cells with the

microtubule-destabilizing agents colchicine and nocodazole significantly decreases the Snail mRNA levels, using qRT-PCR. 18S was used as a housekeeping gene (n = 4; *p<0.05 compared to Vehicle, Kruskal-Wallis test followed by two-tailed Mann-Whitney U test). **(F)** Immunoblots show increased Snail levels, an E-to-N-cadherin switch and decreased Ac-Tubulin levels, all EMT-compatible changes, in A549 cells treated with a CRMP2A siRNA. Actin was used as a loading control (means and SEM are shown for the Snail protein, n = 5; *p<0.05 compared to scramble, two-tailed Mann-Whitney U test). **(G)** Brightfield microscopy shows that CRMP2A siRNA-treated A549 cells have a more elongated, spindle-like shape compared to scramble-treated cells, resembling the CRISPR-generated CRMP2A-deficient cells. **(H)** Immunoblots show increased Snail levels and an E-to-N-cadherin switch in SW480 (colon) cancer cells treated with a CRMP2A siRNA. Actin was used as a loading control (means and SEM are shown for the Snail protein, n = 4; *p<0.05 compared to scramble, two-tailed Mann-Whitney U test). **(I)** Correlation plot shows a strong negative correlation between total CRMP2A and Snail levels in a panel of 8 different human cancer cell lines (r ~ -0.94; *p<0.05, Spearman's correlation). **(J)** Exposure of normal epithelial cells (renal proximal tubule) to low glucose (Glc) does not induce Snail. However, pre-treatment with a CRMP2A siRNA allows for the induction of Snail, suggesting that CRMP2A is a break to the induction of EMT under metabolic stress in normal epithelial cells. Actin was used as a loading control (means and SEM are shown, n = 3; *p<0.05 compared to scramble/low glucose, Kruskal-Wallis test followed by one-tailed Mann-Whitney U test).

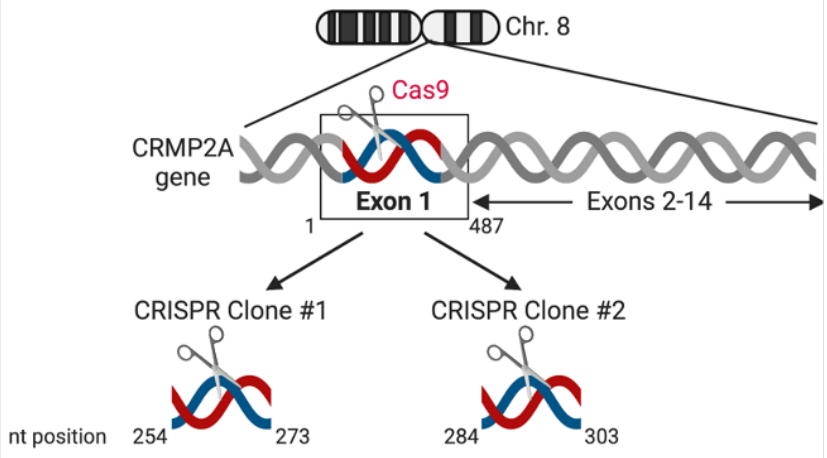

Figure 2-12: CRISPR-based strategy for generation of CRMP2A-deficient cells. Schematic shows the strategy for the generation of CRMP2A-deficient A549 cells, using the CRISPR/Cas9 system. Cleavage was targeted against Exon 1 (unique to CRMP2A but not CRMP2B) of the CRMP2A gene for both clones. The exact position of each guide RNA is also shown. (Created with BioRender.com).

A

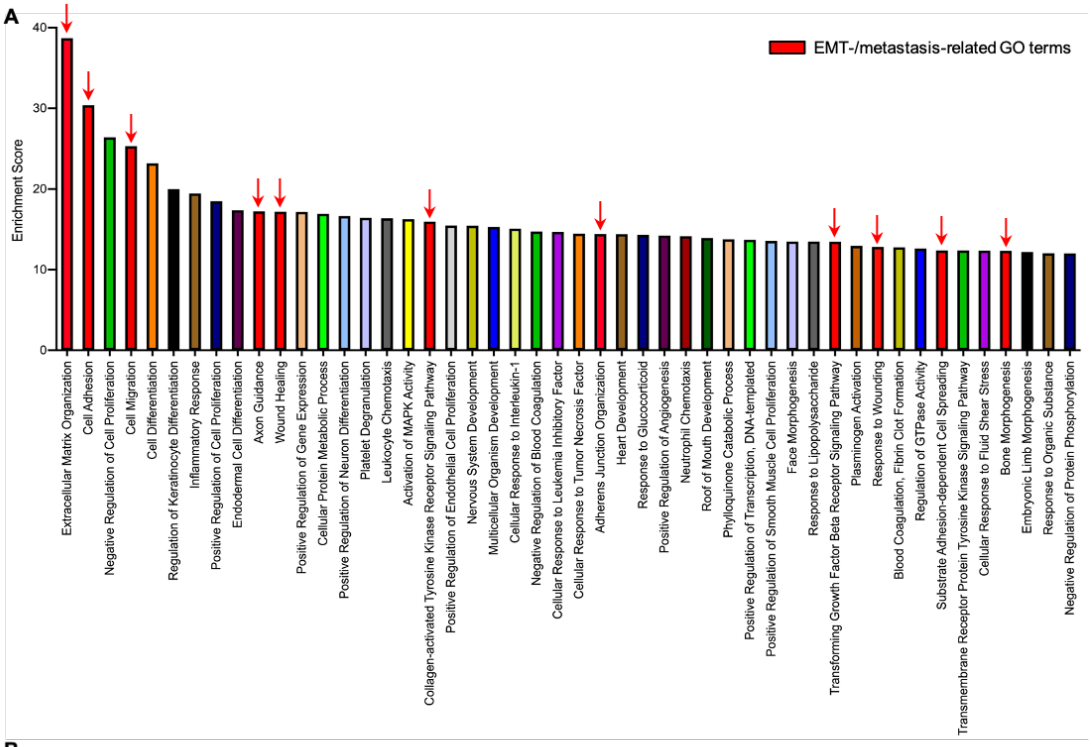

B

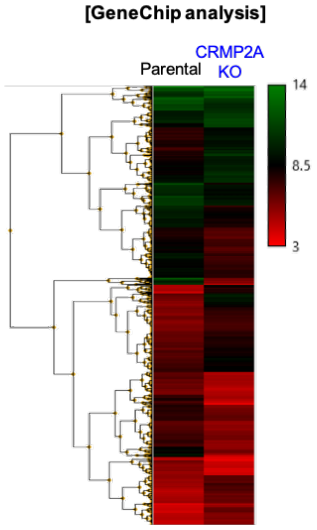

	Gene Name	Fold Change: CRMP2A KO vs. Parental	Full name
UP	*BMP2	> +20	Bone Morphogenetic Protein 2
	*COL5A1	> +10	Collagen, Type V, alpha 1
	*SPARC	+ 9.56	Secreted protein, acidic, cysteine-rich
	MMP2	+ 5.24	Matrix Metallopeptidase 2
	TWIST1	+ 5.15	Twist family bHLH transciption factor 1
	CDH2	+ 5.03	Cadherin 2, type 1, N-cadherin (neuronal)
	SLUG	+ 3.9	Snail family zinc finger 2
	TGFB2	+ 3.56 (1.6)	Transforming Growth Factor Beta 2
	*ACTA2	+ 2.8	Actin, alpha 2, smooth muscle, aorta
	*TGFBI	+ 2.79	Transforming Growth Factor, Beta-induced
	FOXF2	+ 2.23	Forkhead Box F2
	ITGB3	+ 2.04	Integrin beta 3
	SOX2	+ 2.02	SRY Box 2
	*CD44	+ 1.7	CD44 antigen
	*SNAI1	+ 1.66	Snail family zinc finger 1
DOWN	*PTAFR	- 1.31	Platelet-Activating Factor Receptor
	UBQLN1	- 1.78	Ubiquilin 1
	*HOOK-1	- 1.89	Hook Microtubule-tethering protein 1
	DSP	- 2.61	Desmoplakin
	JUP	-2.66	Junction plakoglobin
	*HNF-4α	- 3.14	Hepatocyte nuclear factor 4, alpha
	*OCLN	-4.72	Occludin

Figure 2-13: CRMP2A-deficient cells show enrichment of EMT/metastasis- and stemness-associated pathways.

(A) Unbiased GO (gene ontology) enrichment analysis of a GeneChip assay comparing parental to CRMP2A-deficient cells reveals significant enrichment of EMT- and metastasis-related processes (red bars and also denoted by red arrows) in the CRMP2A-deficient cells. The top 48 enriched GO terms are shown after analysis using the GeneAnalytics software. **(B)** Hierarchical clustering heatmap shows the GeneChip results from parental and CRMP2A-deficient cells (left). Values represent the average of log (base 2) expression for each gene. The color scale bar for heat intensity is shown next to the heatmap. The most significantly altered EMT-related genes are listed in a Table (right). Asterisks denote some of the mRNAs (with at least 1.5-fold change) that were similarly regulated between CRMP2A-deficient (CRISPR) and CRMP2A siRNA-treated cells. Almost all of these genes are compatible with a phenotype switch towards EMT and increased stemness.

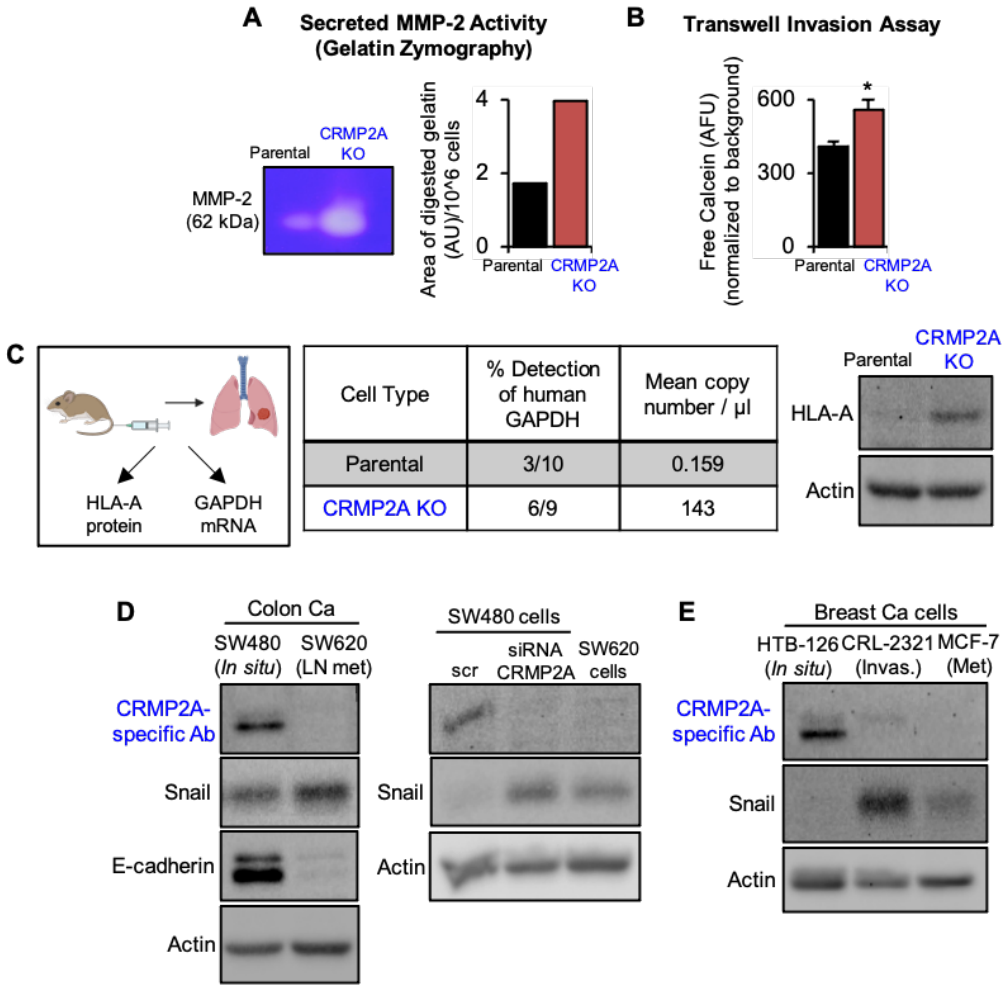
A
Secreted MMP-2 Activity
(Gelatin Zymography)
Parental
CRMP2A KO
MMP-2
(62 kDa)
Area of digested gelatin
(AU)/10^6 cells
4
2
0
Parental
CRMP2A KO
B
Transwell Invasion Assay
Free Calcein (AFU)
(normalized to background)
600
300
0
*
Parental
CRMP2A KO
C
HLA-A
protein
GAPDH
mRNA
Cell Type
% Detection of human GAPDH
Mean copy number / µl
Parental
3/10
0.159
CRMP2A KO
6/9
143
Parental
CRMP2A KO
HLA-A
Actin
D
Colon Ca
SW480 (In situ)
SW620 (LN met)
CRMP2A-specific Ab
Snail
E-cadherin
Actin
SW480 cells
scr
siRNA CRMP2A
SW620 cells
Snail
Actin
E
Breast Ca cells
HTB-126 (In situ)
CRL-2321 (Invas.)
MCF-7 (Met)
CRMP2A-specific Ab
Snail
Actin

Figure 2-14: CRMP2A-deficient cells have increased invasive and metastatic properties.

(A) Gelatinolytic activity of secreted MMP-2 is higher in CRMP2A-deficient cells compared to parental cells, as assessed by an MMP-2 zymography assay (graph shows the area of digested gelatin per million cells). **(B)** CRMP2A-deficient cells are more invasive *in vitro* compared to parental cells, using a cell invasion assay. We quantified the free Calcein fluorescence, which reflects the number of cells that invaded through the membrane of the transwell assay (see methods) (n = 16 wells; *$p<0.05$ compared to parental cells, two-tailed Mann-Whitney U test). **(C)** Schematic shows the methodology for the detection of metastatic A549 cells in the lungs of tail vein-injected mice (n = 9-10 mice injected with parental or CRMP2A-deficient cells). Table shows the number of mice per group with detectable human GAPDH mRNA in the lungs and the mean GAPDH copy number per μl. The specificity of the human GAPDH TaqMan assay (primers and probe) was confirmed in mouse vs. human cells, showing no amplification in mouse cells (data not shown). Immunoblot shows the detection of HLA-A in the lung of a CRMP2A-deficient cells-injected mouse with strong metastatic burden. **(D)** Two types of colon cancer cells were studied: a) a cell line from a primary colon cancer (SW480) and b) a cell line from a metastatic (lymph node) tumor (SW620). Both cell lines came from the *same* patient. Note the decreased levels of CRMP2A and increased levels of Snail in the metastatic (SW620) cells compared to primary tumor (SW480) cells. Upon treatment of SW480 cells with a CRMP2A siRNA, Snail protein expression increases to the levels observed in the metastatic SW620 cells. Actin was used as a loading control. **(E)** Immunoblots show CRMP2A and Snail levels in three breast cancer cell lines established from different

individuals at different tumor stages: HTB-126 (*in situ*), CRL-2321 (invasive ductal) and MCF-7 (metastatic, pleural effusion). Note the loss of CRMP2A and the increase in Snail expression in the invasive and metastatic cells, compared to the *in situ* carcinoma cells. Actin was used as a loading control.

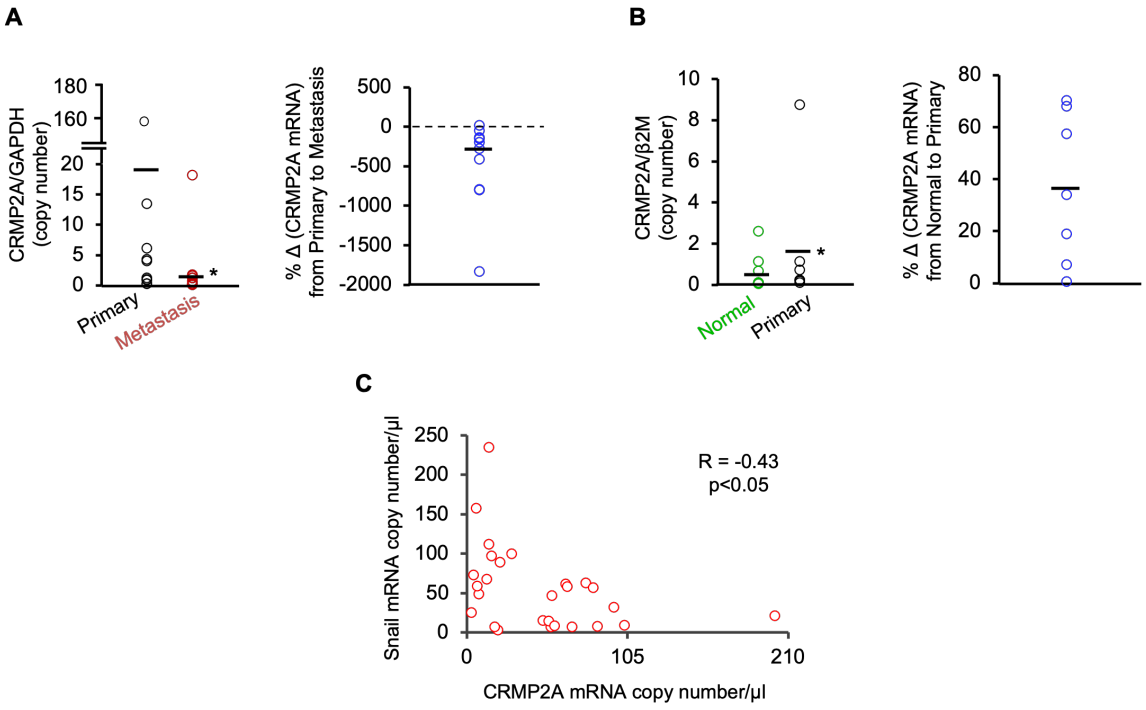
A
CRMP2A/GAPDH (copy number)
180
160
20
15
10
5
0
*
Primary
Metastasis
% Δ (CRMP2A mRNA) from Primary to Metastasis
500
0
-500
-1000
-1500
-2000
B
CRMP2A/β2M (copy number)
10
8
6
4
2
0
*
Normal
Primary
% Δ (CRMP2A mRNA) from Normal to Primary
80
60
40
20
0
C
Snail mRNA copy number/µl
250
200
150
100
50
0
R = -0.43
p<0.05
0
105
210
CRMP2A mRNA copy number/µl

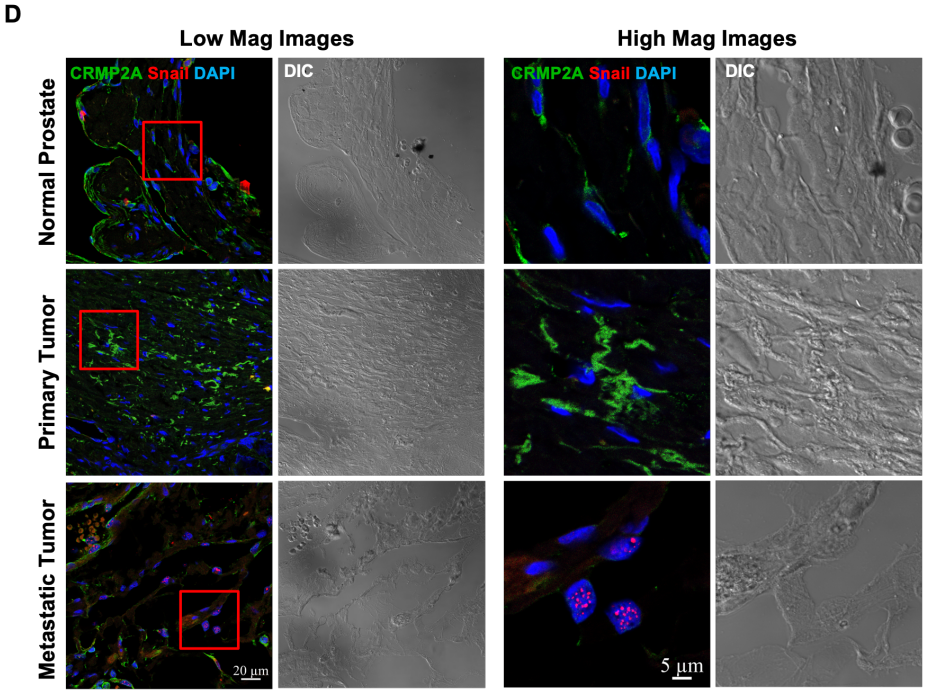
D
Low Mag Images
High Mag Images
CRMP2A Snail DAPI
DIC
CRMP2A Snail DAPI
DIC
Normal Prostate
Primary Tumor
Metastatic Tumor
20 µm
5 µm

Figure 2-15: In a small cohort of prostate cancer patients, CRMP2A expression is higher in biopsies from primary prostate tumors compared to metastatic tumor tissues and normal prostate tissues, while Snail is negatively correlated with CRMP2A.

(A) CRMP2A mRNA levels are lower in sites of metastatic prostate cancer compared to primary tumor sites from the *same* patient (left), resulting in a % decrease (primary tumor site to metastatic site) of the CRMP2A mRNA of ~ 400% on average (right). The clinical data for this cohort are shown in **Fig. 2-16**. GAPDH was used as a housekeeping gene (n = 10; *p<0.05 compared to primary tumor sites, Wilcoxon signed-rank test). **(B)** CRMP2A mRNA levels are higher in biopsies of primary prostate cancer compared to normal prostate tissue from the *same* patient (left), resulting in a % increase (normal tissue to primary tumor site) of the CRMP2A mRNA of ~ 40% on average (right). β2M was used as a housekeeping gene, instead of GAPDH, since GAPDH is known to increase specifically in cancer compared to normal tissues (n = 7; *p<0.05 compared to normal prostate tissues). **(C)** Correlation plot shows a moderate but significant negative correlation between CRMP2A and Snail mRNA levels in a grouped analysis of all available 27 samples, including normal prostate tissues (n = 7), primary tumor tissues (n = 10) and metastatic prostate cancer tissues (n = 10) (n = 27, r = -0.43; *p<0.05, Spearman's correlation). **(D)** Immunofluorescence shows the levels of CRMP2A (cytoplasmic signal) and Snail (nuclear signal) in biopsies of normal prostate (top), primary tumor (middle) and metastatic tumor (bottom) tissue from the *same* individual (part of our prostate cancer cohort) (Snail: red, CRMP2A: green, DAPI nuclear stain: blue). DIC images from the same fields are also shown. Images on the right side (High Mag) are high

magnifications of representative areas (red boxes) from the images on the left (Low Mag). Note that the CRMP2A signal is higher in the primary tumor tissue compared to both normal prostate and metastatic tumor tissue (in keeping with our mRNA expression data), whereas Snail is highest in the metastatic tissue. **c**, Table lists the demographic and clinical data as well as the available tissues for analysis in our cohort of prostate cancer patients.

Patient Data (prostate cancer tissues)

Patient #	Age at metastasis	Serum PSA at metastasis	Primary Gleason Score	TNM Staging	Site of Metastasis	Systemic treatment at the time of metastasis biopsy	Normal Prostate tissue	Prim. Tumor tissue	Met tissue
1	71	53	4+5=9	T4N1M1b	Bone	ADT	x	Yes	Yes
2	61	1202	4+4=8	T3N0M1b	Retroperitoneal LN	None	x	Yes	Yes
3	69	32	3+4=7	T3N0M1c	Lung	None	x	Yes	Yes
4	74	7.9	4+4=8	T2N0M1c	Lung	None	Yes	Yes	Yes
5	79	10.1	4+4=8	T1cN1M1c	Lung	None	Yes	Yes	Yes
6	68	20.8	4+4=8	T3N1M1c	Lung	None	Yes	Yes	Yes
7	57	3.3	5+4=9	T3aN1M0	Pelvic LN	None	Yes	Yes	Yes
8	66	6.8	4+3=7	T3aN1M0	Pelvic LN	None	Yes	Yes	Yes
9	66	11.3	4+5=9	T3bN1M0	Pelvic LN	None	Yes	Yes	Yes
10	55	5.5	4+3=7	T3bN1M0	Pelvic LN	None	Yes	Yes	Yes

ADT: Androgen Deprivation Therapy
LN: Lymph Node

Figure 2-16: Demographic and clinical data as well as tissue availability for analysis in our cohort of prostate cancer patients.

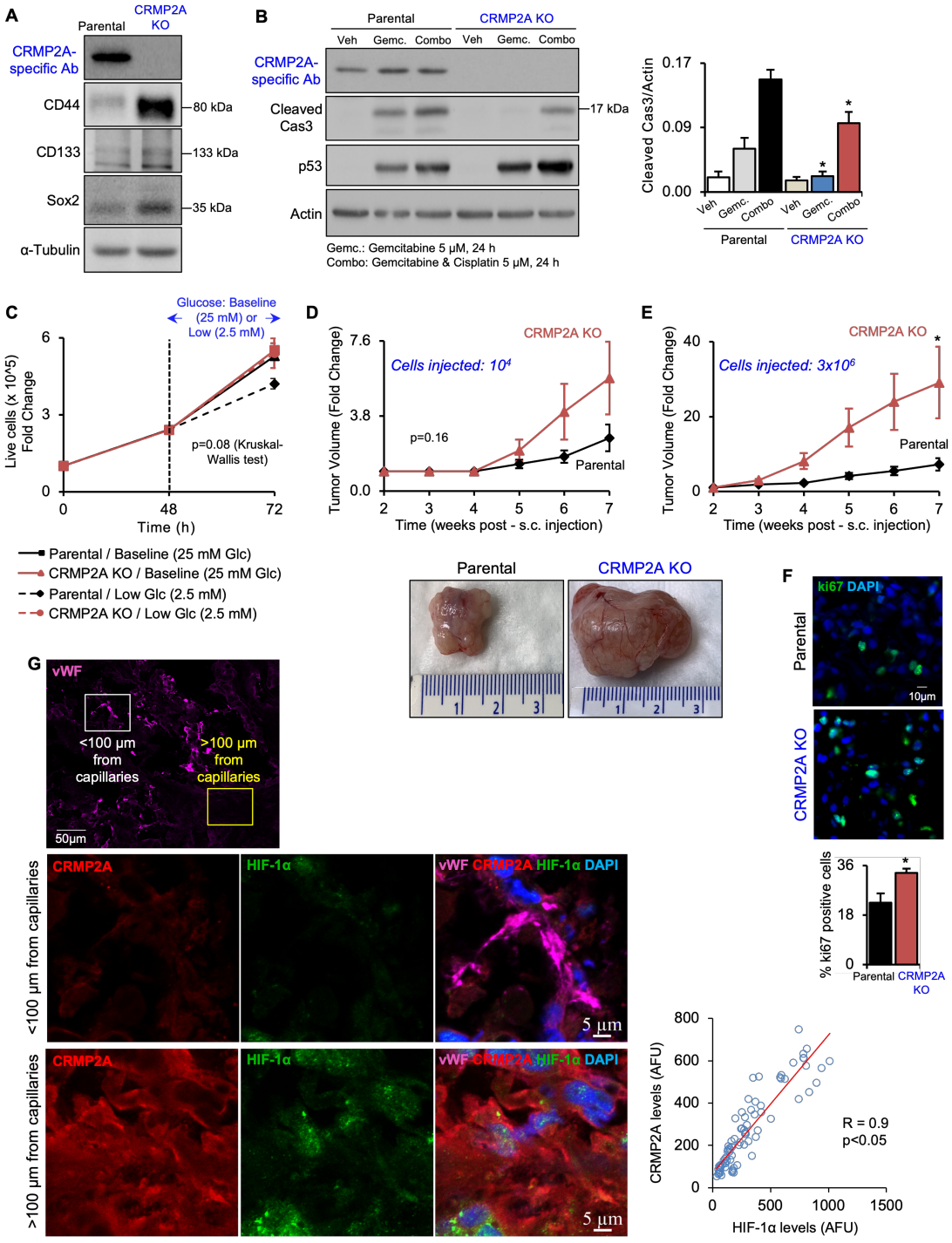
A
Parental
CRMP2A KO
CRMP2A-specific Ab
CD44
CD133
Sox2
α-Tubulin
80 kDa
133 kDa
35 kDa
B
Parental
CRMP2A KO
Veh
Gemc.
Combo
CRMP2A-specific Ab
Cleaved Cas3
p53
Actin
17 kDa
Gemc.: Gemcitabine 5 μM, 24 h
Combo: Gemcitabine & Cisplatin 5 μM, 24 h
Cleaved Cas3/Actin
0.17
0.09
0.00
C
Glucose: Baseline (25 mM) or Low (2.5 mM)
Live cells (x 10^5) Fold Change
p=0.08 (Kruskal-Wallis test)
Time (h)
Parental / Baseline (25 mM Glc)
CRMP2A KO / Baseline (25 mM Glc)
Parental / Low Glc (2.5 mM)
CRMP2A KO / Low Glc (2.5 mM)
D
CRMP2A KO
Cells injected: 10⁴
p=0.16
Parental
Tumor Volume (Fold Change)
Time (weeks post - s.c. injection)
E
CRMP2A KO
Cells injected: 3x10⁶
Parental
Tumor Volume (Fold Change)
Time (weeks post - s.c. injection)
Parental
CRMP2A KO
F
ki67 DAPI
Parental
CRMP2A KO
10μm
% ki67 positive cells
Parental
CRMP2A KO
G
vWF
<100 μm from capillaries
>100 μm from capillaries
50μm
<100 μm from capillaries
>100 μm from capillaries
CRMP2A
HIF-1α
vWF CRMP2A HIF-1α DAPI
5 μm
CRMP2A levels (AFU)
HIF-1α levels (AFU)
R = 0.9
p<0.05

Figure 2-17: CRMP2A-deficient cells have cancer stem cell-like features.

(A) CRMP2A-deficient cells have increased levels of common cancer stem cell markers (CD44, CD133, Sox2) compared to parental cells, using immunoblots. α-Tubulin was used as a loading control. **(B)** CRMP2A-deficient cells treated with Gemcitabine alone or the combination of Gemcitabine and Cisplatin show decreased cleaved Caspase 3 levels (an effector of apoptosis) compared to parental cells, despite a larger increase in p53. Actin was used as a loading control (means and SEM are shown for cleaved Caspase 3, $n = 4$; *$p<0.05$ compared to parental cells, Kruskal-Wallis test followed by two-tailed Mann-Whitney U test). **(C)** Fold change in live cell number (parental or CRMP2A-deficient cells) at 48 and 72 h after plating an equal number of cells at time 0 h (Baseline). Between 48 and 72 h, cells were cultured either in regular/Baseline glucose (25 mM) (solid lines) or in low glucose (2.5 mM) medium. Graph shows increased growth (approaching significance) of CRMP2A-deficient cells under low glucose, suggesting increased resistance to metabolic stress ($n = 4$; $p=0.08$, Kruskal-Wallis test). (**D-E)** CRMP2A-deficient cells grow larger tumors compared to parental cells when injected into the flanks of immunodeficient mice. 10^4 (**D**) or $3x10^6$ (**E**) cells were injected into the left (parental) and right flanks (CRMP2A-deficient) of mice. The CRMP2A-deficient tumors were more detectable at earlier timepoints as described in the main text (means and SEM are shown for the tumor volume fold change over time, $n = 6$ parental or CRMP2A-deficient tumors for the 10^4 cells; $n = 8$ parental or CRMP2A-deficient tumors for the $3x10^6$ cells, *$p<0.05$ compared to parental tumors at 7 weeks post-injection for the $3x10^6$ cells, two-tailed Mann-Whitney U test). Representative images of s.c. xenografts ($3x10^6$ cells) are also shown (bottom). **(F)** CRMP2A-

deficient tumors have higher levels of ki67 staining compared to parental tumors, using confocal microscopy (n = 5-7 random fields per slide for a total of ~20 fields per group; *p<0.05 compared to parental tumors, two-tailed Mann-Whitney U test). **(G)** Immunofluorescence shows that CRMP2A expression is much higher in poorly vascularized, hypoxic tumor areas compared to capillary-rich areas. Parental tumor xenografts were co-stained with von Willebrand factor (vWF, magenta), CRMP2A (red), HIF-1α (green) and DAPI nuclear stain (blue), and then analyzed for CRMP2A and HIF-1α expression in areas close to (<100 μM) and away (>100 μM) from the capillary network (visualized with vWF). Bottom images are high magnifications of representative tumor areas (<100 μM distance from capillaries: white box, >100 μM distance from capillaries: yellow box) identified on a low mag image (vWF signal only is shown for the low mag image). Graph on the right shows a strong positive correlation between HIF-1α and CRMP2A expression *in vivo*, in keeping with our *in vitro* data on HIF-1α and CRMP2A (n = 80 random fields, R=0.9; *p<0.05, Spearman's correlation).

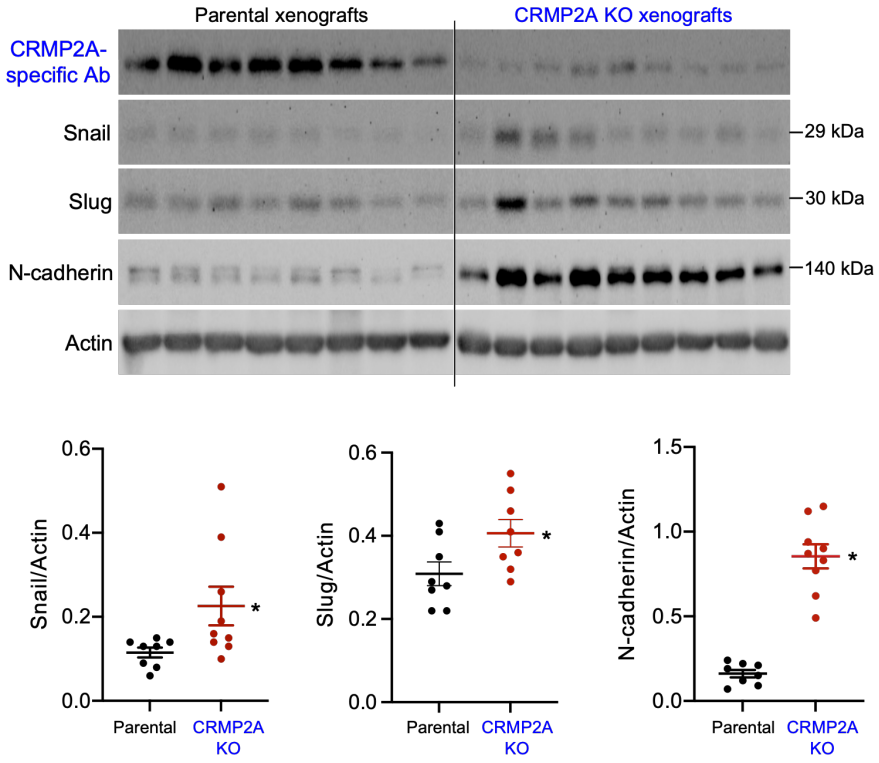

Figure 2-18: CRMP2A-deficient xenografts retain increased expression of EMT markers compared to parental xenografts.

Levels of CRMP2A, Snail, Slug and N-cadherin were measured in s.c. tumor xenografts formed by parental or CRMP2A-deficient cells using immunoblots. The samples were loaded on two different gels (margins indicated by the black vertical line) but treated identically thereafter. Actin was used as a loading control (n = 8 parental tumors and 9 CRMP2A-deficient tumors, *$p<0.05$ compared to parental tumors, two-tailed Mann-Whitney U test).

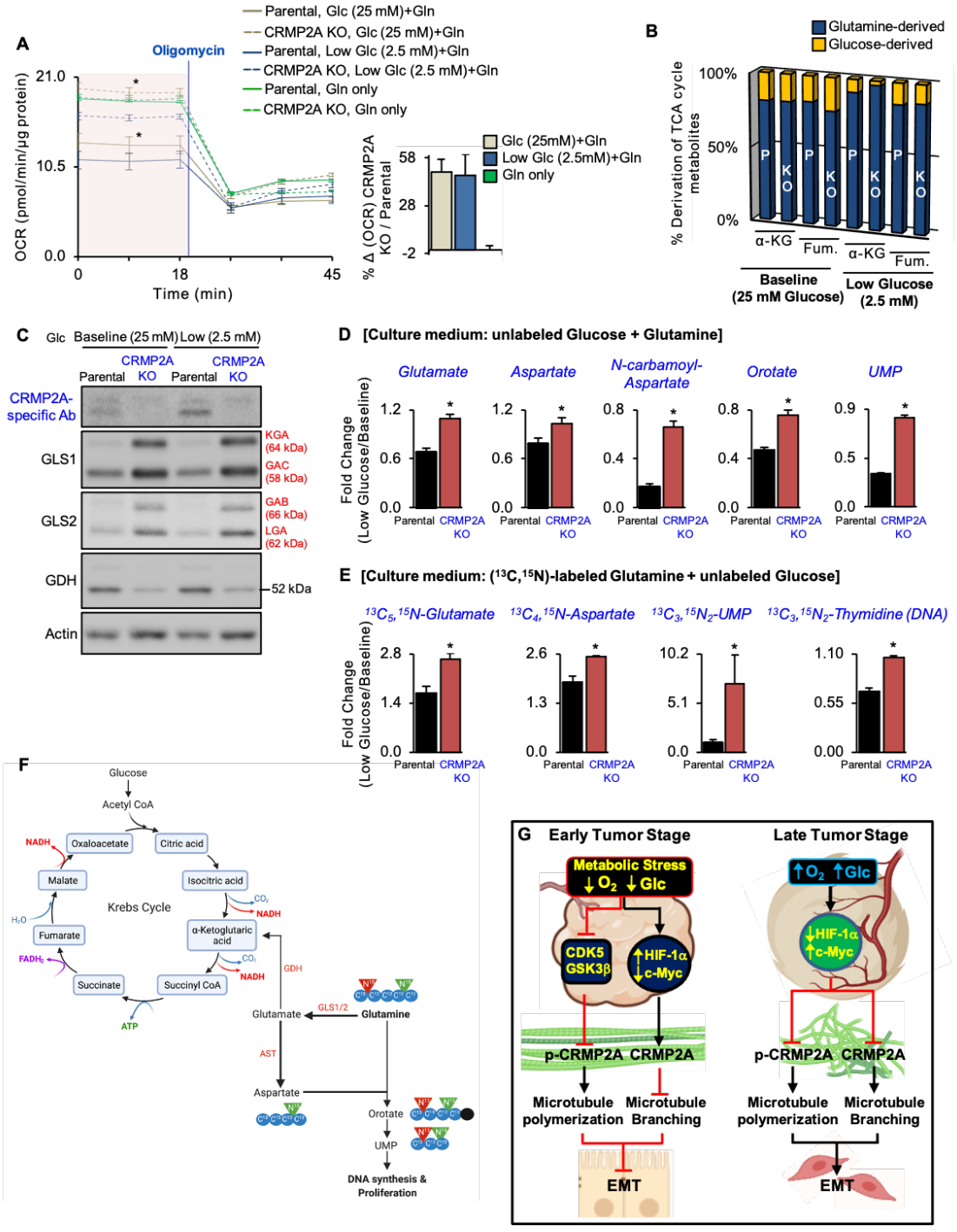
A
Parental, Glc (25 mM)+Gln
CRMP2A KO, Glc (25 mM)+Gln
Parental, Low Glc (2.5 mM)+Gln
CRMP2A KO, Low Glc (2.5 mM)+Gln
Parental, Gln only
CRMP2A KO, Gln only
Oligomycin
OCR (pmol/min/μg protein)
21.0
10.5
0.0
0
18
45
Time (min)
Glc (25mM)+Gln
Low Glc (2.5mM)+Gln
Gln only
% Δ (OCR) CRMP2A KO / Parental
58
28
-2
B
Glutamine-derived
Glucose-derived
% Derivation of TCA cycle metabolites
100%
50%
0%
P
KO
α-KG
Fum.
Baseline (25 mM Glucose)
Low Glucose (2.5 mM)
C
Glc
Baseline (25 mM)
Low (2.5 mM)
Parental
CRMP2A KO
CRMP2A-specific Ab
GLS1
KGA (64 kDa)
GAC (58 kDa)
GLS2
GAB (66 kDa)
LGA (62 kDa)
GDH
52 kDa
Actin
D
[Culture medium: unlabeled Glucose + Glutamine]
Glutamate
Aspartate
N-carbamoyl-Aspartate
Orotate
UMP
Fold Change (Low Glucose/Baseline)
E
[Culture medium: (13C,15N)-labeled Glutamine + unlabeled Glucose]
13C5,15N-Glutamate
13C4,15N-Aspartate
13C3,15N2-UMP
13C3,15N2-Thymidine (DNA)
F
Glucose
Acetyl CoA
Oxaloacetate
Citric acid
Malate
Isocitric acid
Krebs Cycle
Fumarate
α-Ketoglutaric acid
Succinate
Succinyl CoA
ATP
NADH
FADH2
GDH
GLS1/2
Glutamine
Glutamate
AST
Aspartate
Orotate
UMP
DNA synthesis & Proliferation
G
Early Tumor Stage
Late Tumor Stage
Metabolic Stress
↓O2 ↓Glc
↑O2 ↑Glc
CDK5
GSK3β
HIF-1α
c-Myc
p-CRMP2A
CRMP2A
Microtubule polymerization
Microtubule Branching
EMT

Figure 2-19: CRMP2A-deficient cells have an EMT- and stemness-compatible metabolic rearrangement that supports nucleotide synthesis under low glucose conditions.

(A) CRMP2A-deficient cells have ~50% higher oxygen consumption (OCR) at baseline (25 mM glucose + glutamine) and low glucose (2.5 mM glucose + glutamine) conditions, as determined on a Seahorse Analyzer system. This difference is eliminated when the only fuel in the medium is Glutamine. Oligomycin injection (indicated by the blue vertical line at time 18 min) was used to determine the non-mitochondrial respiration (n = 5/group; *$p<0.05$ compared to parental cells at baseline or low glucose conditions, two-tailed Mann-Whitney U test). **(B)** Graph shows the relative contribution of glucose and glutamine towards production of key metabolites of the TCA cycle (α-KG, Fumarate: Fum.) at baseline and low glucose conditions. Cells were cultured with [^{13}C,^{15}N]-L-glutamine and unlabeled glucose. P: parental cells, KO: CRMP2A-deficient cells. **(C)** Immunoblots show that CRMP2A-deficient cells have higher levels of Glutaminase 1 and 2 (GLS1, GLS2) but lower levels of Glutamate Dehydrogenase (GDH) both at baseline (25 mM) and under low glucose (Glc) (2.5 mM) conditions compared to parental cells. GLS1 (KGA, GAC) and GLS2 (GAB, LGA)-specific isoforms, along with their respective molecular weights are indicated in red. Actin was used as a loading control. **(D)** CRMP2A-deficient cells have higher ratios of low glucose/baseline levels for glutamate, aspartate as well as three metabolites (N-carbamoyl-aspartate, Orotate, UMP) of the de novo pyrimidine synthesis pathway compared to parental cells, as determined by Mass Spectrometry. Cells were cultured in medium containing unlabeled glucose and glutamine (means and SEM are shown for the low glucose/baseline fold change, n =

4; *p<0.05 compared to parental cells, two-tailed Mann-Whitney U test). **(E)** CRMP2A-deficient cells have higher ratios of low glucose/baseline levels for [^{13}C,^{15}N]-labeled glutamate, aspartate, UMP and DNA-incorporated thymidine (a UMP derivative), as determined by Mass Spectrometry. Cells were cultured in medium containing [^{13}C,^{15}N]-glutamine and unlabeled glucose in order to trace the origin of carbon and nitrogen in the measured metabolites (means and SEM are shown for the low glucose/baseline fold change, n = 4; *p<0.05 compared to parental cells, two-tailed Mann-Whitney U test). **(F)** Schematic shows the flow (thick black arrows) of (labeled) carbon and nitrogen from glutamine into aspartate and the de novo pyrimidine synthesis pathway. ^{12}C-atoms: black spheres, ^{13}C-atoms: blue spheres, ^{15}N-atoms: red and green triangles. (Created with BioRender.com). **(G)** Proposed schematic of the role of CRMP2A in the induction of an EMT/stemness program that promotes metastasis.

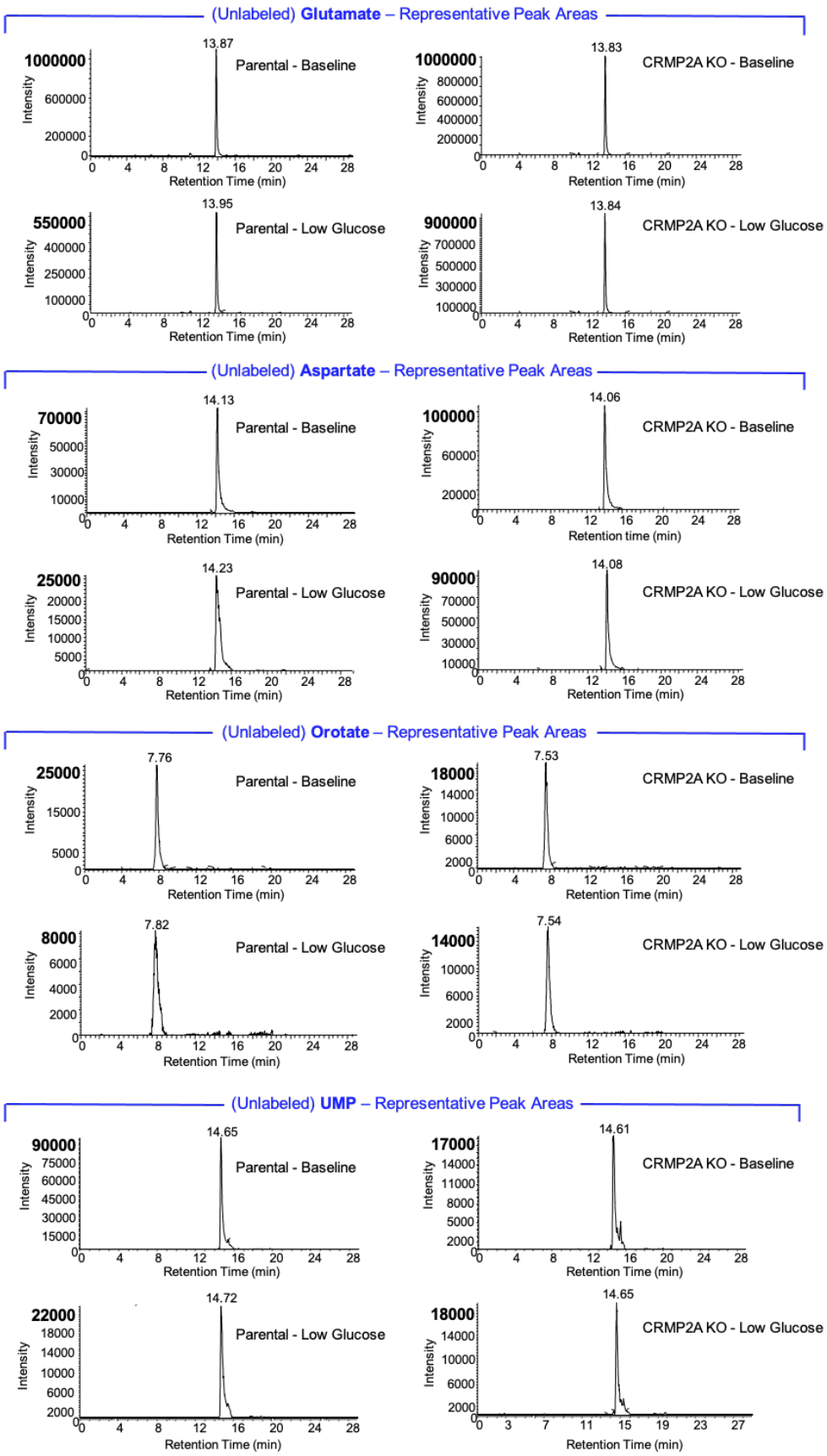
(Unlabeled) Glutamate – Representative Peak Areas
13.87
Parental - Baseline
13.83
CRMP2A KO - Baseline
13.95
Parental - Low Glucose
13.84
CRMP2A KO - Low Glucose
(Unlabeled) Aspartate – Representative Peak Areas
14.13
Parental - Baseline
14.06
CRMP2A KO - Baseline
14.23
Parental - Low Glucose
14.08
CRMP2A KO - Low Glucose
(Unlabeled) Orotate – Representative Peak Areas
7.76
Parental - Baseline
7.53
CRMP2A KO - Baseline
7.82
Parental - Low Glucose
7.54
CRMP2A KO - Low Glucose
(Unlabeled) UMP – Representative Peak Areas
14.65
Parental - Baseline
14.61
CRMP2A KO - Baseline
14.72
Parental - Low Glucose
14.65
CRMP2A KO - Low Glucose
Intensity
Retention Time (min)

Figure 2-20: HPLC chromatograms of metabolites downstream of glutamine metabolism.

Representative chromatograms of unlabeled glutamate, aspartate, orotate and UMP in parental and CRMP2A-deficient cells at baseline and low glucose conditions. X-axis: retention time, Y-axis: (signal) intensity. Plots were created using the Xcalibur software. For comparison purposes, the top value of the Y-axis is shown in bold.

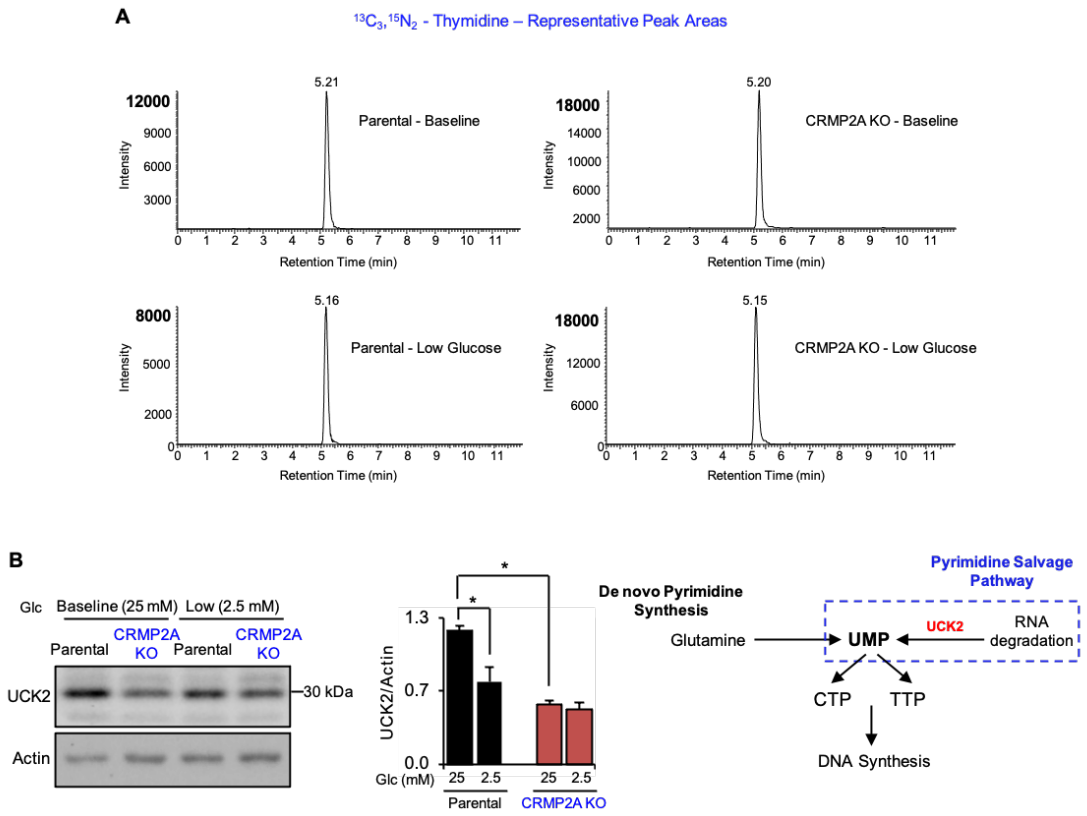

Figure 2-21: CRMP2A-deficient cells support pyrimidine synthesis under low glucose conditions through both the de novo synthetic as well as the pyrimidine salvage pathway.

(A) Representative HPLC chromatograms of [$^{13}C_3$,$^{15}N_2$]-thymidine in parental and CRMP2A-deficient cells at baseline and low glucose conditions. X-axis: retention time, Y-axis: (signal) intensity. Plots were created using the Xcalibur software. For comparison purposes, the top value of the Y-axis is shown in bold. **(B)** Immunoblots show that baseline levels of UCK2 are higher in parental compared to CRMP2A-deficient cells. However, at low glucose (Glc) conditions, UCK2 levels drop significantly in parental but not in CRMP2A-deficient cells. Actin was used as a loading control (n = 5; *p<0.05 compared to parental/baseline, Kruskal-Wallis test followed by two-tailed Mann-Whitney U test).

References

1 Faubert, B., Solmonson, A. & DeBerardinis, R. J. Metabolic reprogramming and cancer progression. *Science* **368**, doi:10.1126/science.aaw5473 (2020).

2 Kinnaird, A., Zhao, S., Wellen, K. E. & Michelakis, E. D. Metabolic control of epigenetics in cancer. *Nat Rev Cancer* **16**, 694-707, doi:10.1038/nrc.2016.82 (2016).

3 Dongre, A. & Weinberg, R. A. New insights into the mechanisms of epithelial-mesenchymal transition and implications for cancer. *Nat Rev Mol Cell Biol* **20**, 69-84, doi:10.1038/s41580-018-0080-4 (2019).

4 Balastik, M. *et al.* Prolyl Isomerase Pin1 Regulates Axon Guidance by Stabilizing CRMP2A Selectively in Distal Axons. *Cell Rep* **13**, 812-828, doi:10.1016/j.celrep.2015.09.026 (2015).

5 Petratos, S. *et al.* The beta-amyloid protein of Alzheimer's disease increases neuronal CRMP-2 phosphorylation by a Rho-GTP mechanism. *Brain* **131**, 90-108, doi:10.1093/brain/awm260 (2008).

6 Tobe, B. T. D. *et al.* Probing the lithium-response pathway in hiPSCs implicates the phosphoregulatory set-point for a cytoskeletal modulator in bipolar pathogenesis. *Proc Natl Acad Sci U S A* **114**, E4462-E4471, doi:10.1073/pnas.1700111114 (2017).

7 Sciacovelli, M. & Frezza, C. Metabolic reprogramming and epithelial-to-mesenchymal transition in cancer. *FEBS J* **284**, 3132-3144, doi:10.1111/febs.14090 (2017).

8 Teo, Z. *et al.* Elevation of adenylate energy charge by angiopoietin-like 4 enhances epithelial-mesenchymal transition by inducing 14-3-3gamma expression. *Oncogene* **36**, 6408-6419, doi:10.1038/onc.2017.244 (2017).

9 Dromparis, P. & Michelakis, E. D. Mitochondria in vascular health and disease. *Annu Rev Physiol* **75**, 95-126, doi:10.1146/annurev-physiol-030212-183804 (2013).

10 Nass, M. M. Differential effects of ethidium bromide on mitochondrial and nuclear DNA synthesis in vivo in cultured mammalian cells. *Exp Cell Res* **72**, 211-222, doi:10.1016/0014-4827(72)90583-6 (1972).

11 Ahn, B. H. *et al.* A role for the mitochondrial deacetylase Sirt3 in regulating energy homeostasis. *Proc Natl Acad Sci U S A* **105**, 14447-14452, doi:10.1073/pnas.0803790105 (2008).

12 Hsieh, A. L., Walton, Z. E., Altman, B. J., Stine, Z. E. & Dang, C. V. MYC and metabolism on the path to cancer. *Semin Cell Dev Biol* **43**, 11-21, doi:10.1016/j.semcdb.2015.08.003 (2015).

13 Dang, C. V. MYC on the path to cancer. *Cell* **149**, 22-35, doi:10.1016/j.cell.2012.03.003 (2012).

14 Nanbru, C. *et al.* Alternative translation of the proto-oncogene c-myc by an internal ribosome entry site. *J Biol Chem* **272**, 32061-32066, doi:10.1074/jbc.272.51.32061 (1997).

15 Bretin, S. *et al.* Differential expression of CRMP1, CRMP2A, CRMP2B, and CRMP5 in axons or dendrites of distinct neurons in the mouse brain. *J Comp Neurol* **486**, 1-17, doi:10.1002/cne.20465 (2005).

16 Quinn, C. C. *et al.* TUC-4b, a novel TUC family variant, regulates neurite outgrowth and associates with vesicles in the growth cone. *J Neurosci* **23**, 2815-2823 (2003).

17 Yuasa-Kawada, J. *et al.* Axonal morphogenesis controlled by antagonistic roles of two CRMP subtypes in microtubule organization. *Eur J Neurosci* **17**, 2329-2343, doi:10.1046/j.1460-9568.2003.02664.x (2003).

18 Grant, N. J. *et al.* Phosphorylation of a splice variant of collapsin response mediator protein 2 in the nucleus of tumour cells links cyclin dependent kinase-5 to oncogenesis. *BMC Cancer* **15**, 885, doi:10.1186/s12885-015-1691-1 (2015).

19 Huang, L. E. Carrot and stick: HIF-alpha engages c-Myc in hypoxic adaptation. *Cell Death Differ* **15**, 672-677, doi:10.1038/sj.cdd.4402302 (2008).

20 Hangas, A. *et al.* Ciprofloxacin impairs mitochondrial DNA replication initiation through inhibition of Topoisomerase 2. *Nucleic Acids Res* **46**, 9625-9636, doi:10.1093/nar/gky793 (2018).

21 Kang, D., Kim, S. H. & Hamasaki, N. Mitochondrial transcription factor A (TFAM): roles in maintenance of mtDNA and cellular functions. *Mitochondrion* **7**, 39-44, doi:10.1016/j.mito.2006.11.017 (2007).

22 Cole, A. R. *et al.* Distinct priming kinases contribute to differential regulation of collapsin response mediator proteins by glycogen synthase kinase-3 in vivo. *J Biol Chem* **281**, 16591-16598, doi:10.1074/jbc.M513344200 (2006).

23 Yeh, E. *et al.* A signalling pathway controlling c-Myc degradation that impacts oncogenic transformation of human cells. *Nat Cell Biol* **6**, 308-318, doi:10.1038/ncb1110 (2004).

24 Higaki, T. Quantitative evaluation of cytoskeletal organizations by microscopic image analysis. *Plant Morphology* **29**, 15-21 (2017).

25 Ma, Q., Sun, J. & Mao, T. Microtubule bundling plays a role in ethylene-mediated cortical microtubule reorientation in etiolated Arabidopsis hypocotyls. *J Cell Sci* **129**, 2043-2051, doi:10.1242/jcs.184408 (2016).

26 Niwa, S. *et al.* Structural basis for CRMP2-induced axonal microtubule formation. *Sci Rep* **7**, 10681, doi:10.1038/s41598-017-11031-4 (2017).

27 Alexandrova, N. *et al.* The N-terminal domain of c-Myc associates with alpha-tubulin and microtubules in vivo and in vitro. *Mol Cell Biol* **15**, 5188-5195, doi:10.1128/mcb.15.9.5188 (1995).

28 Sun, B. O., Fang, Y., Li, Z., Chen, Z. & Xiang, J. Role of cellular cytoskeleton in epithelial-mesenchymal transition process during cancer progression. *Biomed Rep* **3**, 603-610, doi:10.3892/br.2015.494 (2015).

29 Xu, J., Lamouille, S. & Derynck, R. TGF-beta-induced epithelial to mesenchymal transition. *Cell Res* **19**, 156-172, doi:10.1038/cr.2009.5 (2009).

30 Gu, S. *et al.* Loss of alpha-Tubulin Acetylation Is Associated with TGF-beta-induced Epithelial-Mesenchymal Transition. *J Biol Chem* **291**, 5396-5405, doi:10.1074/jbc.M115.713123 (2016).

31 Whipple, R. A. *et al.* Epithelial-to-mesenchymal transition promotes tubulin detyrosination and microtentacles that enhance endothelial engagement. *Cancer Res* **70**, 8127-8137, doi:10.1158/0008-5472.CAN-09-4613 (2010).

32 Michelakis, E. D. *et al.* Metabolic modulation of glioblastoma with dichloroacetate. *Sci Transl Med* **2**, 31ra34, doi:10.1126/scitranslmed.3000677 (2010).

33 Gialeli, C., Theocharis, A. D. & Karamanos, N. K. Roles of matrix metalloproteinases in cancer progression and their pharmacological targeting. *FEBS J* **278**, 16-27, doi:10.1111/j.1742-4658.2010.07919.x (2011).

34 Gomez-Cuadrado, L., Tracey, N., Ma, R., Qian, B. & Brunton, V. G. Mouse models of metastasis: progress and prospects. *Dis Model Mech* **10**, 1061-1074, doi:10.1242/dmm.030403 (2017).

35 Walcher, L. *et al.* Cancer Stem Cells-Origins and Biomarkers: Perspectives for Targeted Personalized Therapies. *Front Immunol* **11**, 1280, doi:10.3389/fimmu.2020.01280 (2020).

36 Zhao, W., Li, Y. & Zhang, X. Stemness-Related Markers in Cancer. *Cancer Transl Med* **3**, 87-95, doi:10.4103/ctm.ctm_69_16 (2017).

37 Dewhirst, M. W., Secomb, T. W., Ong, E. T., Hsu, R. & Gross, J. F. Determination of local oxygen consumption rates in tumors. *Cancer Res* **54**, 3333-3336 (1994).

38 Gatenby, R. A. & Gillies, R. J. Why do cancers have high aerobic glycolysis? *Nat Rev Cancer* **4**, 891-899, doi:10.1038/nrc1478 (2004).

39 Helmlinger, G., Yuan, F., Dellian, M. & Jain, R. K. Interstitial pH and pO2 gradients in solid tumors in vivo: high-resolution measurements reveal a lack of correlation. *Nat Med* **3**, 177-182, doi:10.1038/nm0297-177 (1997).

40 Luo, M., Brooks, M. & Wicha, M. S. Asparagine and Glutamine: Co-conspirators Fueling Metastasis. *Cell Metab* **27**, 947-949, doi:10.1016/j.cmet.2018.04.012 (2018).

41 Sullivan, L. B. *et al.* Supporting Aspartate Biosynthesis Is an Essential Function of Respiration in Proliferating Cells. *Cell* **162**, 552-563, doi:10.1016/j.cell.2015.07.017 (2015).

42 Sullivan, L. B. *et al.* Aspartate is an endogenous metabolic limitation for tumour growth. *Nat Cell Biol* **20**, 782-788, doi:10.1038/s41556-018-0125-0 (2018).

43 Wu, Y. *et al.* Uridine-cytidine kinase 2 (UCK2): A potential diagnostic and prognostic biomarker for lung cancer. *Cancer Sci* **110**, 2734-2747, doi:10.1111/cas.14125 (2019).

44 Mani, S. A. *et al.* The epithelial-mesenchymal transition generates cells with properties of stem cells. *Cell* **133**, 704-715, doi:10.1016/j.cell.2008.03.027 (2008).

45 Morel, A. P. *et al.* Generation of breast cancer stem cells through epithelial-mesenchymal transition. *PLoS One* **3**, e2888, doi:10.1371/journal.pone.0002888 (2008).

46 Gonzalez, D. M. & Medici, D. Signaling mechanisms of the epithelial-mesenchymal transition. *Sci Signal* **7**, re8, doi:10.1126/scisignal.2005189 (2014).

47 Guen, V. J. *et al.* EMT programs promote basal mammary stem cell and tumor-initiating cell stemness by inducing primary ciliogenesis and Hedgehog

signaling. *Proc Natl Acad Sci U S A* **114**, E10532-E10539, doi:10.1073/pnas.1711534114 (2017).

48 Ou, Y. *et al.* Targeting of CRMP-2 to the primary cilium is modulated by GSK-3beta. *PLoS One* **7**, e48773, doi:10.1371/journal.pone.0048773 (2012).

49 Saleme, B. *et al.* Tissue-specific regulation of p53 by PKM2 is redox dependent and provides a therapeutic target for anthracycline-induced cardiotoxicity. *Sci Transl Med* **11**, doi:10.1126/scitranslmed.aau8866 (2019).

50 Cromwell, C. R. *et al.* Incorporation of bridged nucleic acids into CRISPR RNAs improves Cas9 endonuclease specificity. *Nat Commun* **9**, 1448, doi:10.1038/s41467-018-03927-0 (2018).

Chapter Three: Overall Conclusions and Future Directions

3.1 Overall Conclusions

In this dissertation we provide evidence that the microtubule-associated protein CRMP2A, previously studied in neurons in relation to axonal growth and development, is an endogenous "break" to EMT and stemness, regulating the metastatic potential of cancer cells in a metabolic stress-sensitive manner. We found that the unphosphorylated form of CRMP2A is induced in response to a variety of metabolic stresses, most importantly low oxygen and glucose. This net increase in total CRMP2A prevents an extensive cytoskeletal remodeling, including microtubule branching, an EMT-promoting process. By contrast, absence of CRMP2A permits a substantial cytoskeletal remodeling with increased microtubule polymerization and branching as well as actin reorganization, initiating a robust EMT program downstream of it. CRMP2A-deficient cancer cells have increased invasive and metastatic potential, but importantly also features of cancer stem cells (chemoresistance and increased tumor-initiating capacity) as well as a dynamic metabolic remodeling that allows them to produce increased amounts of pyrimidines from glutamine under glucose-poor conditions. Intriguingly, acquisition of this (partial) EMT phenotype occurred in a cell-autonomous manner in contrast to how EMT is usually induced in cancer cells in response to extrinsic stimuli (pro-inflammatory signals, circulating metabolites). Whether the observed metabolic remodelling in CRMP2A-deficient cells is a critical EMT-mediator or a secondary effect downstream of the activation of several EMT transcription factors remains to be explored in the future. Intricate links between metabolism and metastasis have been described in some recent reports. For example, Torrino et al. provided evidence

for the presence of a bidirectional signalling mechanism in breast cancer cells, where stiffening of the matrix in response to microenvironmental cues rewires glutamine metabolism to enhance microtubule glutamylation (a tubulin PTM) and stabilization, thereby promoting cell invasion[1]. Similarly, Wu et al. showed that intracellular energy levels and oxidative phosphorylation were necessary for membrane ruffling and correlated with cell elongation and spreading[2].

Translationally, our findings suggest that the ability of cancer cells to undergo EMT/metastasize and/or acquire aggressive stem cell features may also be closely regulated by CRMP2A depending on the availability of fuel (oxygen, glucose), i.e. their proximity to blood vessels. We preliminarily confirmed this hypothesis in xenotransplanted human tumors *in vivo*, where cancer cells in hypovascular, hypoxic zones had high levels of CRMP2A (and HIF-1α) and low levels of Snail, while the opposite was observed in capillary-rich areas.

Overall, the ability of a single MAP to integrate metabolic inputs and profoundly affect important EMT and stemness is intriguing as it provides a comprehensive mechanism on how (cancer) cells may couple important cell fate decisions with their energetic state.

3.2 Future Directions

Overall, our work offers several interesting lessons for basic scientists, but also has multiple important implications for future translational and clinical research:

- The discovery of CRMP2A as a metabolic stress-responsive protein was "accidental". However, the appearance of unexpected bands on immunoblots is not

uncommon, especially with polyclonal antibodies due to their ability to recognize multiple epitopes. Whether these bands represent true isoforms (characterized, predicted or completely novel) of the protein under study or are merely caused by antibody cross-reactivity is subject to the experimentator's judgment. We believe that unexpected findings like ours should not be rejected up front without careful consideration and in relation to the main hypothesis and the applied experimental conditions. Discovery of the Hypoxia-inducible factor 1 (HIF-1) by Dr. Gregg Semenza (a 2020 Nobel prize winner) and colleagues is probably the best example of this statement.

- This is the first report on how a member of the large CRMP family of microtubule-associated proteins can be regulated **downstream** of metabolic stress. In our study we characterized HIF-1α and c-Myc as two important mediators of this regulation. Specifically for HIF-1α, since HIF-1α levels are tightly regulated by the activity of the α-KG-dependent enzymes prolyl-hydroxylases (HPHs), an interesting and so far unexplored hypothesis in this study is that in response to different types of metabolic stress α-KG levels decrease thus inhibiting the activity of HPHs, which in turn stabilizes HIF-1α levels. We speculate that there may be other signals and regulatory factors, besides HIF-1α and c-Myc, that impinge on CRMP2A. Identification of these pathways may open new perspectives on how CRMP2A (and perhaps other CRMPs) affect the cellular homeostasis. Moreover, the presence of CRMP2A at the crossroads of metabolism and EMT/stemness could be exploited in drug discovery programs, exposing potential vulnerabilities of cancer cells.

- The ability of CRMP2A-deficient cells to synthesize more pyrimidines under low glucose conditions and integrate them into nuclear DNA is an important finding.

As part of future work, it will be important to determine whether loss of CRMP2A is also associated with increased production of the other class of nucleotides, purines, and what the exact molecular drivers might be behind this effect.

- In our study we show that (transient or permanent) loss of CRMP2A induced a partial EMT phenotype with increased invasive and metastatic properties. CRMP2A-deficient cells injected in the bloodstream were able to seed into mouse lungs more than parental cells as determined by the detection of human GAPDH mRNA. However, we were unable to detect large, visible metastatic lesions. One possible explanation for this is that CRMP2A-deficient cells are "locked" in a permanent EMT state and are unable to undergo MET, which would be required for the expansion of metastatic cells in the host organ. To address whether the effects of loss of CRMP2A on EMT are permanent, we will re-introduce CRMP2A into CRMP2A-deficient cells through a tetracycline-inducible Tet-on system. Early administration of doxycycline to animals after iv injection of cells will allow us to see whether CRMP2A-deficient cells are still able to seed into lungs, whereas later administration will allow us to see whether these cells are able to form larger, visible foci in the lungs.

- It remains unknown whether similar metabolism – EMT signaling pathways are operational in other forms of EMT. Although our work focused on EMT in cancer, exploring the role of CRMP2A in the developmental EMT during embryogenesis, a process with high metabolic requirements and little room for errors, will be equally important. Since CRMP2A expression is highest in the developing brain, studying how CRMP2A may potentially integrate metabolic inputs in order to regulate the cell fate (growth, migration) of brain neurons may be an ideal starting

point. Similarly, identifying the potential role of CRMP2A in pathological EMT may provide a novel approach for at least mitigating EMT-related damage in several different diseases (cutaneous wound healing/keloid scar, post-ischemic cardiac fibrosis, renal fibrosis etc.).

- Building on the promising findings from our small cohort of patients with prostate cancer, determining whether CRMP2A could have a role as a prognostic factor for the development of metastatic disease (metastatic biomarker) would be an important question to answer. We would explore this hypothesis by designing a cohort study and enrolling patients with different types of early-stage cancer. CRMP2A expression would be measured in the primary tumor. We would then follow these patients over the course of several years, monitor the development and extent of metastatic disease and correlate it with the levels of CRMP2A in the primary tumor.

References

1 Torrino, S. et al. Mechano-induced cell metabolism promotes microtubule glutamylation to force metastasis. *Cell Metab* **33**, 1342-1357 e1310, doi:10.1016/j.cmet.2021.05.009 (2021).

2 Wu, Y., Zanotelli, M. R., Zhang, J. & Reinhart-King, C. A. Matrix-driven changes in metabolism support cytoskeletal activity to promote cell migration. *Biophys J* **120**, 1705-1717, doi:10.1016/j.bpj.2021.02.044 (2021).

Bibliography

Ahn, B. H. *et al.* A role for the mitochondrial deacetylase Sirt3 in regulating energy homeostasis. *Proc Natl Acad Sci U S A* **105**, 14447-14452, doi:10.1073/pnas.0803790105 (2008).

Alexandrova, N. *et al.* The N-terminal domain of c-Myc associates with alpha-tubulin and microtubules in vivo and in vitro. *Mol Cell Biol* **15**, 5188-5195, doi:10.1128/mcb.15.9.5188 (1995).

Arimura, N. *et al.* CRMP-2 directly binds to cytoplasmic dynein and interferes with its activity. *J Neurochem* **111**, 380-390, doi:10.1111/j.1471-4159.2009.06317.x (2009).

Arimura, N. *et al.* Phosphorylation of collapsin response mediator protein-2 by Rho-kinase. Evidence for two separate signaling pathways for growth cone collapse. *J Biol Chem* **275**, 23973-23980, doi:10.1074/jbc.M001032200 (2000).

Balastik, M. *et al.* Prolyl Isomerase Pin1 Regulates Axon Guidance by Stabilizing CRMP2A Selectively in Distal Axons. *Cell Rep* **13**, 812-828, doi:10.1016/j.celrep.2015.09.026 (2015).

Bretin, S. *et al.* Differential expression of CRMP1, CRMP2A, CRMP2B, and CRMP5 in axons or dendrites of distinct neurons in the mouse brain. *J Comp Neurol* **486**, 1-17, doi:10.1002/cne.20465 (2005).

Cole, A. R. *et al.* Distinct priming kinases contribute to differential regulation of collapsin response mediator proteins by glycogen synthase kinase-3 in vivo. *J Biol Chem* **281**, 16591-16598, doi:10.1074/jbc.M513344200 (2006).

Colvin, H. et al. Oncometabolite D-2-Hydroxyglurate Directly Induces Epithelial-Mesenchymal Transition and is Associated with Distant Metastasis in Colorectal Cancer. Sci Rep 6, 36289, doi:10.1038/srep36289 (2016).

Cromwell, C. R. *et al.* Incorporation of bridged nucleic acids into CRISPR RNAs improves Cas9 endonuclease specificity. *Nat Commun* **9**, 1448, doi:10.1038/s41467-018-03927-0 (2018).

Dang, C. V. MYC on the path to cancer. *Cell* **149**, 22-35, doi:10.1016/j.cell.2012.03.003 (2012).

Dewhirst, M. W., Secomb, T. W., Ong, E. T., Hsu, R. & Gross, J. F. Determination of local oxygen consumption rates in tumors. *Cancer Res* **54**, 3333-3336 (1994).

Dongre, A. & Weinberg, R. A. New insights into the mechanisms of epithelial-mesenchymal transition and implications for cancer. *Nat Rev Mol Cell Biol* **20**, 69-84, doi:10.1038/s41580-018-0080-4 (2019).

Dromparis, P. & Michelakis, E. D. Mitochondria in vascular health and disease. *Annu Rev Physiol* **75**, 95-126, doi:10.1146/annurev-physiol-030212-183804 (2013).

Dustrude, E. T. *et al.* Hierarchical CRMP2 posttranslational modifications control NaV1.7 function. *Proc Natl Acad Sci U S A* **113**, E8443-E8452, doi:10.1073/pnas.1610531113 (2016).

Fan, J. et al. Glutamine-driven oxidative phosphorylation is a major ATP source in transformed mammalian cells in both normoxia and hypoxia. Mol Syst Biol 9, 712, doi:10.1038/msb.2013.65 (2013).

Faubert, B., Solmonson, A. & DeBerardinis, R. J. Metabolic reprogramming and cancer progression. *Science* **368**, doi:10.1126/science.aaw5473 (2020).

Fischer, K. R. *et al.* Epithelial-to-mesenchymal transition is not required for lung metastasis but contributes to chemoresistance. *Nature* **527**, 472-476, doi:10.1038/nature15748 (2015).

Fukata, Y. *et al.* CRMP-2 binds to tubulin heterodimers to promote microtubule assembly. *Nat Cell Biol* **4**, 583-591, doi:10.1038/ncb825 (2002).

Gatenby, R. A. & Gillies, R. J. Why do cancers have high aerobic glycolysis? *Nat Rev Cancer* **4**, 891-899, doi:10.1038/nrc1478 (2004).

Gialeli, C., Theocharis, A. D. & Karamanos, N. K. Roles of matrix metalloproteinases in cancer progression and their pharmacological targeting. *FEBS J* **278**, 16-27, doi:10.1111/j.1742-4658.2010.07919.x (2011).

Gomez-Cuadrado, L., Tracey, N., Ma, R., Qian, B. & Brunton, V. G. Mouse models of metastasis: progress and prospects. *Dis Model Mech* **10**, 1061-1074, doi:10.1242/dmm.030403 (2017).

Gonzalez, D. M. & Medici, D. Signaling mechanisms of the epithelial-mesenchymal transition. *Sci Signal* **7**, re8, doi:10.1126/scisignal.2005189 (2014).

Goshima, Y., Nakamura, F., Strittmatter, P. & Strittmatter, S. M. Collapsin-induced growth cone collapse mediated by an intracellular protein related to UNC-33. *Nature* **376**, 509-514, doi:10.1038/376509a0 (1995).

Grant, N. J. *et al.* Phosphorylation of a splice variant of collapsin response mediator protein 2 in the nucleus of tumour cells links cyclin dependent kinase-5 to oncogenesis. *BMC Cancer* **15**, 885, doi:10.1186/s12885-015-1691-1 (2015).

Grassian, A. R. et al. Isocitrate dehydrogenase (IDH) mutations promote a reversible ZEB1/microRNA (miR)-200-dependent epithelial-mesenchymal transition (EMT). J Biol Chem 287, 42180-42194, doi:10.1074/jbc.M112.417832 (2012).

Gu, S. *et al.* Loss of alpha-Tubulin Acetylation Is Associated with TGF-beta-induced Epithelial-Mesenchymal Transition. *J Biol Chem* **291**, 5396-5405, doi:10.1074/jbc.M115.713123 (2016).

Gu, Y., Hamajima, N. & Ihara, Y. Neurofibrillary tangle-associated collapsin response mediator protein-2 (CRMP-2) is highly phosphorylated on Thr-509, Ser-518, and Ser-522. *Biochemistry* **39**, 4267-4275, doi:10.1021/bi992323h (2000).

Guen, V. J. *et al.* EMT programs promote basal mammary stem cell and tumor-initiating cell stemness by inducing primary ciliogenesis and Hedgehog signaling. *Proc Natl Acad Sci U S A* **114**, E10532-E10539, doi:10.1073/pnas.1711534114 (2017).

Haensel, D. & Dai, X. Epithelial-to-mesenchymal transition in cutaneous wound healing: Where we are and where we are heading. *Dev Dyn* **247**, 473-480, doi:10.1002/dvdy.24561 (2018).

Hamajima, N. *et al.* A novel gene family defined by human dihydropyrimidinase and three related proteins with differential tissue distribution. *Gene* **180**, 157-163, doi:10.1016/s0378-1119(96)00445-3 (1996).

Hanahan, D. & Weinberg, R. A. Hallmarks of cancer: the next generation. *Cell* **144**, 646-674, doi:10.1016/j.cell.2011.02.013 (2011).

Hangas, A. *et al.* Ciprofloxacin impairs mitochondrial DNA replication initiation through inhibition of Topoisomerase 2. *Nucleic Acids Res* **46**, 9625-9636, doi:10.1093/nar/gky793 (2018).

Helmlinger, G., Yuan, F., Dellian, M. & Jain, R. K. Interstitial pH and pO2 gradients in solid tumors in vivo: high-resolution measurements reveal a lack of correlation. *Nat Med* **3**, 177-182, doi:10.1038/nm0297-177 (1997).

Higaki, T. Quantitative evaluation of cytoskeletal organizations by microscopic image analysis. *Plant Morphology* **29**, 15-21 (2017).

Hosios, A. M. et al. Amino Acids Rather than Glucose Account for the Majority of Cell Mass in Proliferating Mammalian Cells. Dev Cell 36, 540-549, doi:10.1016/j.devcel.2016.02.012 (2016).

Hou, S. T. *et al.* CaMKII phosphorylates collapsin response mediator protein 2 and modulates axonal damage during glutamate excitotoxicity. *J Neurochem* **111**, 870-881, doi:10.1111/j.1471-4159.2009.06375.x (2009).

Hsieh, A. L., Walton, Z. E., Altman, B. J., Stine, Z. E. & Dang, C. V. MYC and metabolism on the path to cancer. *Semin Cell Dev Biol* **43**, 11-21, doi:10.1016/j.semcdb.2015.08.003 (2015).

Huang, L. E. Carrot and stick: HIF-alpha engages c-Myc in hypoxic adaptation. *Cell Death Differ* **15**, 672-677, doi:10.1038/sj.cdd.4402302 (2008).

Ju, W. *et al.* SUMOylation alters CRMP2 regulation of calcium influx in sensory neurons. *Channels (Austin)* **7**, 153-159, doi:10.4161/chan.24224 (2013).

Kang, D., Kim, S. H. & Hamasaki, N. Mitochondrial transcription factor A (TFAM): roles in maintenance of mtDNA and cellular functions. *Mitochondrion* **7**, 39-44, doi:10.1016/j.mito.2006.11.017 (2007).

Kato, Y. et al. Acidic extracellular microenvironment and cancer. Cancer Cell Int 13, 89, doi:10.1186/1475-2867-13-89 (2013).

Kawano, Y. *et al.* CRMP-2 is involved in kinesin-1-dependent transport of the Sra-1/WAVE1 complex and axon formation. *Mol Cell Biol* **25**, 9920-9935, doi:10.1128/MCB.25.22.9920-9935.2005 (2005).

Kim, N. H. *et al.* Snail reprograms glucose metabolism by repressing phosphofructokinase PFKP allowing cancer cell survival under metabolic stress. *Nat Commun* **8**, 14374, doi:10.1038/ncomms14374 (2017).

Kinnaird, A., Zhao, S., Wellen, K. E. & Michelakis, E. D. Metabolic control of epigenetics in cancer. *Nat Rev Cancer* **16**, 694-707, doi:10.1038/nrc.2016.82 (2016).

Kudo-Saito, C., Shirako, H., Takeuchi, T. & Kawakami, Y. Cancer metastasis is accelerated through immunosuppression during Snail-induced EMT of cancer cells. *Cancer Cell* **15**, 195-206, doi:10.1016/j.ccr.2009.01.023 (2009).

Li, X. *et al.* Intrinsic resistance of tumorigenic breast cancer cells to chemotherapy. *J Natl Cancer Inst* **100**, 672-679, doi:10.1093/jnci/djn123 (2008).

Liberti, M. V. & Locasale, J. W. The Warburg Effect: How Does it Benefit Cancer Cells? *Trends Biochem Sci* **41**, 211-218, doi:10.1016/j.tibs.2015.12.001 (2016).

Lim, J. & Thiery, J. P. Epithelial-mesenchymal transitions: insights from development. *Development* **139**, 3471-3486, doi:10.1242/dev.071209 (2012).

Lin, Y., Dong, C. & Zhou, B. P. Epigenetic regulation of EMT: the Snail story. *Curr Pharm Des* **20**, 1698-1705, doi:10.2174/13816128113199990512 (2014).

Liu, Y. *et al.* Functional variants in DPYSL2 sequence increase risk of schizophrenia and suggest a link to mTOR signaling. *G3 (Bethesda)* **5**, 61-72, doi:10.1534/g3.114.015636 (2014)

Liu, Y. & Yang, C. Oncometabolites in Cancer: Current Understanding and Challenges. Cancer Res 81, 2820-2823, doi:10.1158/0008-5472.CAN-20-3730 (2021).

Luo, M., Brooks, M. & Wicha, M. S. Asparagine and Glutamine: Co-conspirators Fueling Metastasis. *Cell Metab* **27**, 947-949, doi:10.1016/j.cmet.2018.04.012 (2018).

Luo, Y., Raible, D. & Raper, J. A. Collapsin: a protein in brain that induces the collapse and paralysis of neuronal growth cones. *Cell* **75**, 217-227, doi:10.1016/0092-8674(93)80064-l (1993).

Ma, Q., Sun, J. & Mao, T. Microtubule bundling plays a role in ethylene-mediated cortical microtubule reorientation in etiolated Arabidopsis hypocotyls. *J Cell Sci* **129**, 2043-2051, doi:10.1242/jcs.184408 (2016).

Majmundar, A. J., Wong, W. J. & Simon, M. C. Hypoxia-inducible factors and the response to hypoxic stress. *Mol Cell* **40**, 294-309, doi:10.1016/j.molcel.2010.09.022 (2010).

Mani, S. A. *et al.* The epithelial-mesenchymal transition generates cells with properties of stem cells. *Cell* **133**, 704-715, doi:10.1016/j.cell.2008.03.027 (2008).

Mecollari, V., Nieuwenhuis, B. & Verhaagen, J. A perspective on the role of class III semaphorin signaling in central nervous system trauma. *Front Cell Neurosci* **8**, 328, doi:10.3389/fncel.2014.00328 (2014).

Metallo, C. M. et al. Reductive glutamine metabolism by IDH1 mediates lipogenesis under hypoxia. Nature 481, 380-384, doi:10.1038/nature10602 (2011).

Michelakis, E. D. *et al.* Metabolic modulation of glioblastoma with dichloroacetate. *Sci Transl Med* **2**, 31ra34, doi:10.1126/scitranslmed.3000677 (2010).

Mokhtar, S. H. *et al.* Amyloid-beta-dependent phosphorylation of collapsin response mediator protein-2 dissociates kinesin in Alzheimer's disease. *Neural Regen Res* **13**, 1066-1080, doi:10.4103/1673-5374.233451 (2018).

Morel, A. P. *et al.* Generation of breast cancer stem cells through epithelial-mesenchymal transition. *PLoS One* **3**, e2888, doi:10.1371/journal.pone.0002888 (2008).

Myllykoski, M., Baumann, A., Hensley, K. & Kursula, P. Collapsin response mediator protein 2: high-resolution crystal structure sheds light on small-molecule binding, post-translational modifications, and conformational flexibility. *Amino Acids* **49**, 747-759, doi:10.1007/s00726-016-2376-z (2017).

Nanbru, C. *et al.* Alternative translation of the proto-oncogene c-myc by an internal ribosome entry site. *J Biol Chem* **272**, 32061-32066, doi:10.1074/jbc.272.51.32061 (1997).

Nass, M. M. Differential effects of ethidium bromide on mitochondrial and nuclear DNA synthesis in vivo in cultured mammalian cells. *Exp Cell Res* **72**, 211-222, doi:10.1016/0014-4827(72)90583-6 (1972).

Niwa, S. *et al.* Structural basis for CRMP2-induced axonal microtubule formation. *Sci Rep* **7**, 10681, doi:10.1038/s41598-017-11031-4 (2017).

Oliemuller, E. *et al.* Phosphorylated tubulin adaptor protein CRMP-2 as prognostic marker and candidate therapeutic target for NSCLC. *Int J Cancer* **132**, 1986-1995, doi:10.1002/ijc.27881 (2013).

Ou, Y. *et al.* Targeting of CRMP-2 to the primary cilium is modulated by GSK-3beta. *PLoS One* **7**, e48773, doi:10.1371/journal.pone.0048773 (2012).

Pastushenko, I. & Blanpain, C. EMT Transition States during Tumor Progression and Metastasis. *Trends Cell Biol* **29**, 212-226, doi:10.1016/j.tcb.2018.12.001 (2019).

Pei, D., Shu, X., Gassama-Diagne, A. & Thiery, J. P. Mesenchymal-epithelial transition in development and reprogramming. *Nat Cell Biol* **21**, 44-53, doi:10.1038/s41556-018-0195-z (2019).

Petratos, S. *et al.* The beta-amyloid protein of Alzheimer's disease increases neuronal CRMP-2 phosphorylation by a Rho-GTP mechanism. *Brain* **131**, 90-108, doi:10.1093/brain/awm260 (2008).

Pham, X. *et al.* The DPYSL2 gene connects mTOR and schizophrenia. *Transl Psychiatry* **6**, e933, doi:10.1038/tp.2016.204 (2016).

Quinn, C. C. *et al.* TUC-4b, a novel TUC family variant, regulates neurite outgrowth and associates with vesicles in the growth cone. *J Neurosci* **23**, 2815-2823 (2003).

Saleme, B. *et al.* Tissue-specific regulation of p53 by PKM2 is redox dependent and provides a therapeutic target for anthracycline-induced cardiotoxicity. *Sci Transl Med* **11**, doi:10.1126/scitranslmed.aau8866 (2019).

Sciacovelli, M. & Frezza, C. Metabolic reprogramming and epithelial-to-mesenchymal transition in cancer. *FEBS J* **284**, 3132-3144, doi:10.1111/febs.14090 (2017).

Stemmler, M. P., Eccles, R. L., Brabletz, S. & Brabletz, T. Non-redundant functions of EMT transcription factors. *Nat Cell Biol* **21**, 102-112, doi:10.1038/s41556-018-0196-y (2019).

Stenmark, P. *et al.* The structure of human collapsin response mediator protein 2, a regulator of axonal growth. *J Neurochem* **101**, 906-917, doi:10.1111/j.1471-4159.2006.04401.x (2007).

Stone, R. C. et al. Epithelial-mesenchymal transition in tissue repair and fibrosis. Cell Tissue Res 365, 495-506, doi:10.1007/s00441-016-2464-0 (2016).

Sullivan, L. B. *et al.* Aspartate is an endogenous metabolic limitation for tumour growth. *Nat Cell Biol* **20**, 782-788, doi:10.1038/s41556-018-0125-0 (2018).

Sullivan, L. B. *et al.* Supporting Aspartate Biosynthesis Is an Essential Function of Respiration in Proliferating Cells. *Cell* **162**, 552-563, doi:10.1016/j.cell.2015.07.017 (2015).

Sun, B. O., Fang, Y., Li, Z., Chen, Z. & Xiang, J. Role of cellular cytoskeleton in epithelial-mesenchymal transition process during cancer progression. *Biomed Rep* **3**, 603-610, doi:10.3892/br.2015.494 (2015).

Sun, L. & Fang, J. Epigenetic regulation of epithelial-mesenchymal transition. *Cell Mol Life Sci* **73**, 4493-4515, doi:10.1007/s00018-016-2303-1 (2016).

Tahimic, C. G. *et al.* Evidence for a role of Collapsin response mediator protein-2 in signaling pathways that regulate the proliferation of non-neuronal cells. *Biochem Biophys Res Commun* **340**, 1244-1250, doi:10.1016/j.bbrc.2005.12.132 (2006).

Teo, Z. *et al.* Elevation of adenylate energy charge by angiopoietin-like 4 enhances epithelial-mesenchymal transition by inducing 14-3-3gamma expression. *Oncogene* **36**, 6408-6419, doi:10.1038/onc.2017.244 (2017).

Tobe, B. T. D. *et al.* Probing the lithium-response pathway in hiPSCs implicates the phosphoregulatory set-point for a cytoskeletal modulator in bipolar pathogenesis.

Proc Natl Acad Sci U S A **114**, E4462-E4471, doi:10.1073/pnas.1700111114 (2017).

Torrino, S. et al. Mechano-induced cell metabolism promotes microtubule glutamylation to force metastasis. Cell Metab 33, 1342-1357 e1310, doi:10.1016/j.cmet.2021.05.009 (2021).

Uchida, Y. *et al.* Semaphorin3A signalling is mediated via sequential Cdk5 and GSK3beta phosphorylation of CRMP2: implication of common phosphorylating mechanism underlying axon guidance and Alzheimer's disease. *Genes Cells* **10**, 165-179, doi:10.1111/j.1365-2443.2005.00827.x (2005).

Vega, S. *et al.* Snail blocks the cell cycle and confers resistance to cell death. *Genes Dev* **18**, 1131-1143, doi:10.1101/gad.294104 (2004).

Walcher, L. *et al.* Cancer Stem Cells-Origins and Biomarkers: Perspectives for Targeted Personalized Therapies. *Front Immunol* **11**, 1280, doi:10.3389/fimmu.2020.01280 (2020).

Wang, L. H. & Strittmatter, S. M. A family of rat CRMP genes is differentially expressed in the nervous system. *J Neurosci* **16**, 6197-6207 (1996).

Wang, Z. et al. Targeting Glutaminolysis: New Perspectives to Understand Cancer Development and Novel Strategies for Potential Target Therapies. Front Oncol 10, 589508, doi:10.3389/fonc.2020.589508 (2020).

Whipple, R. A. *et al.* Epithelial-to-mesenchymal transition promotes tubulin detyrosination and microtentacles that enhance endothelial engagement. *Cancer Res* **70**, 8127-8137, doi:10.1158/0008-5472.CAN-09-4613 (2010).

Wilson, M. M., Weinberg, R. A., Lees, J. A. & Guen, V. J. Emerging Mechanisms by which EMT Programs Control Stemness. *Trends Cancer* **6**, 775-780, doi:10.1016/j.trecan.2020.03.011 (2020).

Winkler, S. C., Shimobayashi, E. & Kapfhammer, J. P. PKCgamma-Mediated Phosphorylation of CRMP2 Regulates Dendritic Outgrowth in Cerebellar Purkinje Cells. *Mol Neurobiol* **57**, 5150-5166, doi:10.1007/s12035-020-02038-6 (2020).

Wu, Y. *et al.* Uridine-cytidine kinase 2 (UCK2): A potential diagnostic and prognostic biomarker for lung cancer. *Cancer Sci* **110**, 2734-2747, doi:10.1111/cas.14125 (2019).

Wu, Y., Zanotelli, M. R., Zhang, J. & Reinhart-King, C. A. Matrix-driven changes in metabolism support cytoskeletal activity to promote cell migration. Biophys J 120, 1705-1717, doi:10.1016/j.bpj.2021.02.044 (2021).

Xu, J., Lamouille, S. & Derynck, R. TGF-beta-induced epithelial to mesenchymal transition. *Cell Res* **19**, 156-172, doi:10.1038/cr.2009.5 (2009).

Xu, W. et al. Oncometabolite 2-hydroxyglutarate is a competitive inhibitor of alpha-ketoglutarate-dependent dioxygenases. Cancer Cell 19, 17-30, doi:10.1016/j.ccr.2010.12.014 (2011).

Yang, L., Venneti, S. & Nagrath, D. Glutaminolysis: A Hallmark of Cancer Metabolism. Annu Rev Biomed Eng 19, 163-194, doi:10.1146/annurev-bioeng-071516-044546 (2017).

Yang, X. *et al.* Conventional protein kinase Cbeta-mediated phosphorylation inhibits collapsin response-mediated protein 2 proteolysis and alleviates ischemic injury

in cultured cortical neurons and ischemic stroke-induced mice. *J Neurochem* **137**, 446-459, doi:10.1111/jnc.13538 (2016).

Yeh, E. *et al.* A signalling pathway controlling c-Myc degradation that impacts oncogenic transformation of human cells. *Nat Cell Biol* **6**, 308-318, doi:10.1038/ncb1110 (2004).

Yoshida, H., Watanabe, A. & Ihara, Y. Collapsin response mediator protein-2 is associated with neurofibrillary tangles in Alzheimer's disease. *J Biol Chem* **273**, 9761-9768, doi:10.1074/jbc.273.16.9761 (1998).

Yoshimura, T. *et al.* GSK-3beta regulates phosphorylation of CRMP-2 and neuronal polarity. *Cell* **120**, 137-149, doi:10.1016/j.cell.2004.11.012 (2005).

Yu, J. *et al.* Snail Enhances Glycolysis in the Epithelial-Mesenchymal Transition Process by Targeting FBP1 in Gastric Cancer. *Cell Physiol Biochem* **43**, 31-38, doi:10.1159/000480314 (2017).

Yuasa-Kawada, J. *et al.* Axonal morphogenesis controlled by antagonistic roles of two CRMP subtypes in microtubule organization. *Eur J Neurosci* **17**, 2329-2343, doi:10.1046/j.1460-9568.2003.02664.x (2003).

Zhao, W., Li, Y. & Zhang, X. Stemness-Related Markers in Cancer. *Cancer Transl Med* **3**, 87-95, doi:10.4103/ctm.ctm_69_16 (2017).

Zheng, Y. *et al.* Tuning microtubule dynamics to enhance cancer therapy by modulating FER-mediated CRMP2 phosphorylation. *Nat Commun* **9**, 476, doi:10.1038/s41467-017-02811-7 (2018).

Appendix I: Materials used in this dissertation

REAGENT or RESOURCE	SOURCE	IDENTIFIER
Antibodies		
Mouse monoclonal anti-α-Tubulin (clone DM1A)	Sigma-Aldrich	Cat#T6199; RRID: AB_477583
Mouse monoclonal anti-Acetyl-Tubulin (Clone 6-11B-1)	Sigma-Aldrich	Cat#T6793; RRID: AB_477585
Mouse monoclonal anti-Actin	Abcam	Cat#ab3280; RRID: AB_303668
Rabbit monoclonal anti-BMP2	Abcam	Cat#ab214821; RRID: AB_2814695
Rabbit monoclonal anti-CD44	Cell Signaling Technology	Cat#37259; RRID: AB_2750879
Goat polyclonal anti-CD133 (clone K-18)	Santa Cruz Biotechnology	Cat#sc-23797; RRID: AB_2172885
Rabbit polyclonal anti-CDK5	Cell Signaling Technology	Cat#2506; RRID: AB_2078855
Rabbit polyclonal anti-Cleaved Caspase-3 (Asp175)	Cell Signaling Technology	Cat#9661; RRID: AB_2341188
Rabbit monoclonal anti-c-Myc	Cell Signaling Technology	Cat#5605; RRID: AB_1903938
Rabbit polyclonal anti-c-Myc	Cell Signaling Technology	Cat#9402; RRID: AB_2151827
Rabbit monoclonal anti-CRMP2	Cell Signaling Technology	Cat#35672; RRID: AB_2799082
Rabbit monoclonal anti-CRMP2A	INSERM (Dr. Veronique Rogemond)	N/A
Mouse monoclonal anti-CRMP2A	This paper (GenScript)	N/A
Rabbit polyclonal anti-Detyrosinated-α-Tubulin	Abcam	Cat#ab48389; RRID: AB_869990
Rabbit monoclonal anti-E-cadherin	Cell Signaling Technology	Cat#3195; RRID: AB_2291471
Rabbit monoclonal anti-GDH	Cell Signaling Technology	Cat#12793; RRID: AB_2750880
Rabbit monoclonal anti-GLS1	Cell Signaling Technology	Cat#56750
Rabbit polyclonal anti-GLS2	Abcam	Cat#ab113509; RRID: AB_10866157
Rabbit monoclonal anti-HIF-1α	Cell Signaling Technology	Cat#14179; RRID: AB_2622225
Rabbit polyclonal anti-HIF-1α	Cell Signaling Technology	Cat#3716; RRID: AB_2116962
Rabbit monoclonal anti-HLA-A	Abcam	Cat# ab52922; RRID: AB_881225
Rabbit polyclonal anti-Ki67	Abcam	Cat# ab15580; RRID: AB_443209
Rabbit monoclonal anti-MEK2	Cell Signaling Technology	Cat#9147; RRID: AB_2140641

Rabbit monoclonal anti-N-cadherin	Cell Signaling Technology	Cat#13116; RRID: AB_2687616
Rabbit polyclonal anti-p53	Cell Signaling Technology	Cat#9282; RRID: AB_331476
Rabbit polyclonal anti-Phospho-CRMP-2 (Thr514)	Cell Signaling Technology	Cat#9397; RRID: AB_2094336
Rabbit monoclonal anti-SIRT3	Cell Signaling Technology	Cat#5490; RRID: AB_10828246
Rabbit monoclonal anti-Snail	Cell Signaling Technology	Cat#3879S; RRID: AB_2255011
Rabbit monoclonal anti-Slug	Cell Signaling Technology	Cat#9585; RRID: AB_2239535
Mouse monoclonal anti-Sox2	Cell Signaling Technology	Cat#4900; RRID: AB_10560516
Rabbit monoclonal anti-SP1	Cell Signaling Technology	Cat#9389; RRID: AB_11220235
Rabbit polyclonal anti-TFAM	Cell Signaling Technology	Cat#7495; RRID: AB_10841294
Rabbit polyclonal anti-UCK2	Proteintech	Cat#10511-1-AP; RRID: AB_2241182
Donkey anti-rabbit IgG (H+L) Alexa Fluor 488 conjugated	Invitrogen	Cat#A-21206; RRID: AB_2535792
Donkey anti-rabbit IgG (H+L) highly cross-adsorbed secondary antibody, Alexa Fluor 546	Thermo Fisher Scientific	Cat#A-10040; RRID: AB_2534016
Goat anti-mouse IgG2b cross-adsorbed secondary antibody, Alexa Fluor 647	Thermo Fisher Scientific	Cat#A-21242; RRID: AB_2535811
Donkey anti-goat IgG-HRP antibody	Santa Cruz Biotechnology	Cat#sc-2056; RRID: AB_631730
Anti-mouse IgG, HRP-linked antibody	Cell Signaling Technology	Cat#7076; RRID: AB_330924
Anti-rabbit IgG, HRP-linked antibody	Cell Signaling Technology	Cat#7074; RRID: AB_2099233
Biological Samples		
Patient-derived prostate cancer tissues	The Alberta Prostate Cancer Research Initiative	https://apcari.ca
Chemicals, Peptides, and Recombinant Proteins		
5-Aza-2′-deoxycytidine	Sigma-Aldrich	Cat#A3656; CAS: 2353-33-5
2x Laemmli Sample Buffer Concentrate	Sigma-Aldrich	Cat#S3401
4x Laemmli Sample Buffer	Bio-Rad	Cat#161-0747
30% Acrylamide/Bis Solution 37.1:1	Bio-Rad	Cat#161-0158
Acetonitrile, Optima LC/MS Grade	Thermo Fisher Scientific	Cat#A955-4; CAS: 75-05-08

Agilent Technologies XF24 FluxPak Mini	Agilent Technologies	Cat#102342100
Alkaline Phosphatase Type VII-S (from bovine intestinal mucosa)	Sigma-Aldrich	Cat#P5521; CAS: 9001-78-9
Amersham ECL Western Blotting Detection Reagent	Cytiva	Cat#RPN2106
Ammonium Acetate (Optima LC/MS)	Fisher Scientific	Cat#A11450; CAS: 631-61-8
Ammonium Hydroxide	Fisher Scientific	Cat# A669S-500; CAS: 1336-21-6
Antibiotic Solution	ScienCell Research Laboratories	Cat#0503
Antibiotic-Antimycotic	Gibco	Cat#15240
APS	Bio-Rad	Cat#161-0700; CAS: 7727-54-0
Aspartic acid sodium salt monohydrate >=98% (TLC)	Sigma-Aldrich	Cat#A6683; CAS: 323194-76-9
CHAPS Hydrate >=98% (TLC)	Sigma-Aldrich	Cat#C3023; CAS: 331717-45-4
Ciprofloxacin HCl	Santa Cruz	Cat#sc-29064; CAS: 93107-08-5
Cisplatin	Abcam	Cat#ab141398; CAS: 15663-27-1
Coomassie Brilliant Blue R-250	Bio-Rad	Cat#1610400; CAS: 6104-59-2
Countess Cell Counting Chamber Slides	Thermo Fisher Scientific	Cat#C10228
D-(+)-Glucose	Sigma-Aldrich	Cat#G7021; CAS: 50-99-7
DAPI	Molecular Probes	Cat#D1306; CAS: 28718-90-3
DeStreak Reagent	GE Healthcare	Cat#17600318
DMEM, no glucose	Gibco	Cat#11966
DMEM, no glucose, no glutamine, no phenol red	Gibco	Cat#A1443001
DMEM, high glucose, pyruvate	Gibco	Cat#11995
DMSO Hybri-Max	Sigma-Aldrich	Cat#D2650
Donkey Serum	Sigma-Aldrich	Cat#D9663
DSS (disuccinimidyl suberate)	Thermo Fisher Scientific	Cat#21655
Epithelial Cell Growth Supplement	ScienCell Research Laboratories	Cat#4152
Epithelial Cell Medium (EpiCM)	ScienCell Research Laboratories	Cat#4101
Ethidium Bromide	Bio-Rad	Cat#161-0433
Fetal Bovine Serum	Sigma-Aldrich	Cat#F1051
Gelatin from bovine skin, Type B, powder, BioReagent, cell culture	Sigma-Aldrich	Cat#G9391; CAS 9000-70-8
Gemcitabine	Abcam	ab145657; CAS: 95058-81-4

Glutamic acid monosodium salt hydrate	Sigma-Aldrich	Cat#G5889; CAS: 142-47-2(anhydrous)
Image-IT FX signal enhancer	Invitrogen	Cat#I36933
Immobiline DryStrip, 24cm, pH 3-11, Nonlinear	GE Healthcare	Cat#17-6003-77
Iodoacetamide Bioultra	Sigma-Aldrich	Cat#I1149; CAS: 144-48-9
L-Glutamine-13C5,15N2,98 atom % 13C, 98 atom % 15N	Sigma-Aldrich	Cat#607983
Lipofectamine RNAiMax	Thermo Fisher Scientific	Cat#13778
MAT2A Inhibitor II, FIDAS-5	Calbiochem	Cat# 504173
N, N, N', N'-Tetramethylethylenediamine	Sigma-Aldrich	Cat#T9281; CAS: 110-18-9
Normal Goat Serum	Cell Signaling Technology	Cat#5425S
Nuclease P1 (from Penicillium Citrinum)	Sigma-Aldrich	Cat#N8630; CAS: 54576-84-0
Oligomycin	Sigma-Aldrich	Cat#O4876; CAS: 1404-19-9
OptiMEM Reduced Serum Medium	Thermo Fisher Scientific	Cat#31985
Orotic acid, ≥98% (titration), anhydrous	Sigma-Aldrich	Cat#O2750
Paraformaldehyde	Sigma-Aldrich	Cat#158127; CAS: 30525-89-4
Phalloidin-iFluor 488 Reagent	Abcam	Cat#ab176753
Phosphodiesterase I (from Crotalus adamanteus venom)	Sigma-Aldrich	Cat#P3243; CAS: 9025-82-5
Pierce IP lysis buffer	Thermo Fisher Scientific	Cat#87787
Pierce BCA Protein Assay Kit	Thermo Fisher Scientific	Cat#23227
Precision Plus Kaleidoscope Protein Standard	Bio-Rad	Cat#161-0395
ProLong Glass Antifade Mountant	Invitrogen	Cat#P36984
Phenylmethanesulfonyl fluoride solution	Sigma-Aldrich	Cat#93482; CAS: 329-98-6
Protease Inhibitor Cocktail Powder	Sigma-Aldrich	Cat#P2714
rhTGF-β1	R&D Systems	Cat#240-B-002
Resolving Gel Buffer	Bio-Rad	Cat#1610798
RIPA Buffer	Sigma-Aldrich	Cat#R0278
Seahorse XF base medium, without phenol red	Agilent Technologies	Cat#103335-100
Sodium Orthovanadate	Sigma-Aldrich	Cat#S6508; CAS: 13721-39-6
Small Airway Epithelial Cell Medium	ScienCell Research Laboratories	Cat#3231
Stacking Gel Buffer	Bio-Rad	Cat#1610799
Superfrost Plus microscope slides	Fisher Scientific	Cat# 22-037-246
SYBR Green PCR Master Mix	Applied Biosystems	Cat#4309155
TCA cycle metabolite library	Sigma-Aldrich	Cat#ML0010
Thiourea	Sigma-Aldrich	Cat#T7875; CAS: 62-56-6

Thymidine ≥99.0% (HPLC)	Sigma-Aldrich	Cat#89270; CAS: 50-89-5
Trans-Blot Turbo 5x Transfer Buffer	Bio-Rad	Cat#10026938
Triton X-100	Sigma-Aldrich	Cat#T8787; CAS: 9002-93-1
Trypan Blue solution	Sigma-Aldrich	Cat#T8154; CAS: 72-57-1
Trypsin-EDTA, 0.25% 1X, Phenol Red	Gibco	Cat#25200
Ultrapure Distilled Water DNAse, RNAse free	Invitrogen	Cat#10977
Ureidosuccinate (>99%)	Selleck Chemicals	Cat#S6259
Uridine 5'-monophosphate disodium salt (>99%)	Sigma-Aldrich	Cat#6375
Critical Commercial Assays		
AllPrep DNA/RNA Mini Kit	Qiagen	80204
CultreCoat 96® Well Medium BME Cell Invasion Assay	Trevigen	3482-096-K
Dual-Luciferase Reporter Assay System	Promega	E1910
One-Step RT-ddPCR Advanced Kit for Probes	Bio-Rad	1864021
ReadyPrep 2-D Cleanup Kit	Bio-Rad	1632130
RNeasy FFPE Kit	Qiagen	73504
SimpleChIP Enzymatic Chromatin IP Kit	Thermo Fisher Scientific	9003
Subcellular Protein Fractionation Kit for Cultured Cells	Thermo Fisher Scientific	78840
TaqMan RNA-to-Ct 1-Step Kit	Applied Biosystems	4392938
Experimental Models: Cell lines		
Human: A549 cells	ATCC	CCL-185
Human: Glioblastoma (GBM) cells	Our lab[32]	-
Human: H1299 cells	ATCC	CRL-5803
Human: HCC1143 cells	ATCC	CRL-2321
Human: HeLa cells	ATCC	CCL-2
Human: HFF-1 cells	ATCC	SCRC-1041
Human: HEK-293 cells	ATCC	CRL-1573.3
Human: Passage 8 HGPS Fibroblasts from Skin, Arm	NIA Aging Cell Culture Repository	AG03513
Human: Hs578T cells	ATCC	HTB-126
Human: Renal Proximal Tubular Epithelial Cells	ScienCell Research Laboratories	4100
Human: Small Airway Epithelial Cells	ScienCell Research Laboratories	3230
Human: MCF-7 cells	ATCC	HTB-22
Human: MDA-MB-231 cells	ATCC	HTB-26
Human: SW480 cells	ATCC	CCL-228
Human: SW620 cells	ATCC	CCL-227

Human: U2-OS cells	ATCC	HTB-96
Mouse: Mouse Embryonic Fibroblasts	ATCC	SCRC-1008
Experimental Models: Organisms/Strains		
Mouse: Crl:NU-*Foxn1*^{nu}	Charles River Canada	088 (homozygous)
Oligonucleotides		
c-Myc siRNA (Exon 1-targeting) 1.1 (ID: ABRSAC8)	Ambion	Cat# (custom)
c-Myc siRNA (Exon 1-targeting) 1.2 (ID: ABVI4VW)	Ambion	Cat# (custom)
c-Myc siRNA (Exon 2-targeting) (ID: VHS407089)	Ambion	Cat#1299001
c-Myc siRNA (Exon 3-targeting) 3.1 (ID: s9130)	Ambion	Cat#4392420
c-Myc siRNA (Exon 3-targeting) 3.2 (ID: s9131)	Ambion	Cat#4392420
CRMP2A siRNA (ID: CD.Ri.63593.13.14)	iDT	Cat# (custom)
HIF-1α siRNA (ID: 42840)	Ambion	Cat#AM51331
SIRT3 siRNA (ID: s23768)	Ambion	Cat#4392420
TFAM siRNA (ID: s14000)	Ambion	Cat#4427037
18S rRNA TaqMan assay (ID: Hs03003631_g1)	Life Technologies	Cat#4331182
CRMP2A TaqMan assay	Life Technologies	Cat# (custom)
Snail TaqMan assay (ID: Hs00195591_m1)	Life Technologies	Cat#4427037
Software and Algorithms		
GeneAnalytics	LifeMap Sciences	https://geneanalytics.genecards.org
GraphPad Prism (v8.0)	GraphPad Software	https://www.graphpad.com
Image J (v.1.53h)	NIH	https://imagej.nih.gov